APPENDIX B

HOLOCENE PALEOSEISMOLOGY OF THE CENTRAL SEGMENTS OF THE WASATCH FAULT ZONE, UTAH

By

Christopher B. DuRoss[1,7], Stephen F. Personius[2], Anthony J. Crone[3], Susan S. Olig[4,8], Michael D. Hylland[1], William R. Lund[5], and David P. Schwartz[6]

[1]Utah Geological Survey, Salt Lake City, Utah
[2]U.S. Geological Survey, Golden, Colorado
[3]U.S. Geological Survey, Emeritus
[4]URS Corporation, Oakland, California
[5]Utah Geological Survey, Emeritus
[6]U.S. Geological Survey, Menlo Park, California
[7]Currently U.S Geological Survey, Golden, Colorado
[8]Currently Olig Seismic Geology, Martinez, California

2016

Research supported by the U.S. Geological Survey (USGS), Department of the Interior, under USGS award numbers G11AP20004 and G13AP00002 to the Utah Geological Survey.

Suggested citation:

DuRoss, C.B., Personius, S.F., Crone, A.J., Olig, S.S., Hylland, M.D., Lund, W.R., and Schwartz, D.P., 2016, Holocene paleoseismology of the central segments of the Wasatch fault zone, Utah—Appendix B, *in* Working Group on Utah Earthquake Probabilities (WGUEP), Earthquake probabilities for the Wasatch Front region in Utah, Idaho, and Wyoming: Utah Geological Survey Miscellaneous Publication 16-3, p. B1–B70.

CONTENTS

TABLES

FIGURES

INTRODUCTION

The Wasatch fault zone (WFZ) is Utah's longest and most active normal-slip fault, extending about 350 km from southern Idaho to central Utah, and forming the general structural boundary between the Basin and Range Province to the west and the relatively more stable Middle Rocky Mountain and Colorado Plateau provinces to the east. The WFZ has a complex trace that comprises ten structural segments defined on the basis of fault geometry and structure (Schwartz and Coppersmith, 1984; Machette *et al*., 1992; Wheeler and Krystinik, 1992) (Figure B-1). Five central segments (Brigham City to Nephi; figure B-2) have geomorphic (scarp-profile) and paleoseismic (mostly fault-trench) evidence of repeated Holocene surface-faulting earthquakes (Machette *et al*., 1992; Lund, 2005), and are the focus of this appendix. These segments are thought to generally rupture as seismogenically independent parts of the WFZ on the basis of clear differences in earthquake timing—especially for the best constrained most recent earthquakes—that occur across the prominent structural boundaries (DuRoss *et al.*, 2016). Thus, in the absence of well-defined rupture boundaries for prehistoric ruptures of the WFZ, we use the structural boundaries, together with paleoseismic earthquake timing and displacement data, as the basis for defining the fault's surface rupture characteristics and uncertainties. Additional discussion of paleoseismic data in the context of structural complexities along the WFZ is included in DuRoss *et al.* (2016). The end segments—including the Malad City, Clarkston Mountain, and Collinston segments to the north and the Levan and Fayette segments to the south (Figure B-1)—are discussed in Section 4.2 of the main report.

Segmentation models for the WFZ have evolved as additional paleoseismic data have been obtained along the fault. Schwartz and Coppersmith (1984) used the results of five early paleoseismic studies (described by Swan *et al*., 1980, 1981) to formulate a six-segment model between Collinston and Levan. Schwartz and Coppersmith (1984) also used these data to support a characteristic earthquake model, which implies that some faults or segments tend to produce similar-sized earthquakes at the upper end of their possible magnitude ranges, and thus have relatively large and constant displacement at a point in individual earthquakes (see also Hecker *et al*., 2013). Machette *et al*. (1992) developed a ten-segment model following the acquisition of additional paleoseismic data (see also Lund, 2005). This now well-established model is supported by (1) well-defined fault salients that are marked by complex and diffuse faulting and shallow bedrock (indicating decreased fault displacement), which separates adjacent hanging-wall basins; (2) along-strike changes in fault geometry and range-front morphology, and timing of most recent surface faulting; and (3) for each of the five central segments (Figure B-2), unique Holocene surface-faulting earthquake chronologies (Swan *et al*., 1980; Schwartz and Coppersmith, 1984; Machette *et al*., 1992; Wheeler and Krystinik, 1992). Although fault and paleoearthquake data generally support the Machette *et al*. (1992) model for the central segments, remaining uncertainties in paleoearthquake timing and displacement data permit alternative models (Chang and Smith, 2002; DuRoss, 2008; DuRoss *et al*., 2011).

On the central WFZ, prominent fault scarps displace late Holocene to latest Pleistocene geomorphic surfaces as much as several tens of meters and have been the focus of numerous paleoseismic fault-trench investigations. To date, 23 research trench sites (excluding trench projects for pre-development fault-setback and educational purposes) have yielded earthquake timing and/or displacement data. The majority of these sites are on faulted Holocene alluvial-fan surfaces, although scarps on latest Pleistocene surfaces related to phases of pluvial Lake

Bonneville (e.g., Oviatt *et al.*, 1992; Godsey *et al.*, 2005, 2011) have also provided important paleoseismic information (Lund, 2005). Fourteen of these research trench projects span the late 1970s (e.g., Swan *et al.*, 1980) to the late 1990s (e.g., Lund and Black, 1998), which we refer to as legacy data. Studies of the remaining nine sites occurred in the 11 years from the 1999 Little Cottonwood Canyon megatrench work (McCalpin, 2002) to the 2010 trenches on the Salt Lake City segment at Penrose Drive (DuRoss *et al.*, 2014). These more recent investigations capitalized on advances in numerical dating, such as improved soil sampling and sorting methods (e.g., the separation and identification of charcoal fragments; Puseman and Cummings, 2005), accelerator mass spectrometry (AMS) radiocarbon dating of minute charcoal fragments (e.g., Tucker *et al.*, 1983), optically stimulated luminescence (OSL) dating of clastic grains (e.g., Huntley *et al.*, 1985; Aitken, 1994; Duller, 2008), and the quantitative assessment of numerical ages using chronostratigraphic models (OxCal; Bronk Ramsey, 1995, 2001, 2008). For more thorough discussions of the evolution of WFZ paleoseismic data and dating methods see Lund (2005), Nelson *et al.* (2006), DuRoss *et al.* (2011), and Personius *et al.* (2012).

Paleoseismic data indicate that the central WFZ has been very active in Holocene time. Lund (2005) reported mean recurrence times of 1.3 to 2.5 kyr (kilo-year) for late Holocene (post ~6 ka [thousand years ago]) surface-faulting earthquakes on the central WFZ. Results of the more recent (1999–2010) trenching investigations (e.g., Machette *et al.*, 2007; DuRoss *et al.*, 2009; Olig *et al.*, 2011) show that the mean recurrence time for surface-rupturing earthquakes is similar for the five central segments, closer to ~1.3 kyr than ~2.5 kyr. DuRoss (2008) showed that the mean net vertical displacement per surface-rupturing earthquake for the central segments is 2.2 ± 1.0 m (±1σ), and average vertical slip rates range from about 0.5 to 2.2 mm/yr using paleoseismic and geomorphic data (Machette *et al.*, 1992; Friedrich *et al.*, 2003; Lund, 2005). However, despite all of these paleoseismic data, important questions remained regarding earthquakes on the central five segments of the WFZ at the time of this analysis. For example, should legacy paleoseismic data be superseded by or integrated with the results of more recent paleoseismic studies, which have generally yielded smaller earthquake-timing uncertainties due to improved sampling and dating methods? How complete are the paleoseismic data for each segment, and what methods should be used to calculate earthquake recurrence values and fault slip rates? How robust is the segmentation model for the fault—that is, should alternative (e.g., multi-segment-rupture) models be included to assess the hazard? Finally, which magnitude regression parameters, such as surface rupture length and average displacement (e.g., Wells and Coppersmith, 1994), are most suitable to characterize prehistoric earthquake magnitudes for the central WFZ?

To address these questions, we systematically examined paleoseismic data for the central WFZ segments to rigorously characterize their surface-faulting earthquake histories and rates of activity. For each segment, we (1) reviewed and compiled published paleoseismic data from each trench site (we considered, but generally excluded incomplete and unpublished data); (2) constructed time-stratigraphic OxCal models for each site (using version 4 of Bronk Ramsey [1995, 2001] and the terrestrial calibration curve of Reimer *et al.* [2009]), which yielded earthquake-timing probability density functions (PDFs) for each site; (3) constructed earthquake histories for each segment by correlating and combining the per-site earthquake-timing PDFs along the segment; (4) using the revised earthquake histories per segment, calculated inter-event and mean earthquake recurrence intervals; and (5) calculated vertical slip rates using displacement per rupture and source estimates and the recurrence-interval data. Finally, we evaluated the segmentation of the central WFZ and constructed several rupture models that address epistemic uncertainties in fault segmentation and earthquake rupture extent.

In this analysis, we compared and combined site-earthquake data (i.e., paleoseismic trench data) for each segment separately. That is, we did not systematically compare site earthquakes along the fault (i.e., on adjacent segments) to exhaustively allow for all possible rupture combinations (e.g., Biasi and Weldon, 2009). The assumption of single-segment ruptures on the central WFZ is consistent with Machette *et al*. (1992), Lund (2005), and DuRoss (2008), but affects the determination of the segment chronologies and recurrence intervals. Ultimately, we considered the potential for rupture beyond the segment boundaries and defined rupture uncertainties to account for more flexibility in the segmentation of the fault, but considered the treatment of the fault in a fully unsegmented manner outside the scope of this work.

SURFACE-FAULTING EARTHQUAKE HISTORIES

We reviewed, compiled, and evaluated paleoseismic data for the central WFZ segments to determine their surface-faulting earthquake histories, including the elapsed time since the most recent surface-faulting earthquakes (MRE) on each segment. For each segment, we used trench stratigraphy and numerical ages to construct time-stratigraphic OxCal models for each site, which allowed us to objectively model earthquake timing (e.g., Bronk Ramsey, 2008; Lienkaemper and Bronk Ramsey, 2009) and to generate earthquake-timing PDFs for each site (site PDFs; Figure B-3; Tables B-1 to B-5). We correlated the site PDFs along the segment using a quantitative measure of the amount of overlap in the site PDFs (after Biasi and Weldon, 2009), as well as inferences and conclusions in the original paleoseismic reports. For each segment, we then combined the site PDFs to construct earthquake histories for each entire segment (segment PDFs; Figures B-3 and B-4) using either the mean or the product methods of DuRoss *et al.* (2011) (Table B-6). Because of the detailed nature of this work, we only include a summary of the paleoseismic data for each segment here. More thorough discussions of original paleoseismic data and segment-wide earthquake chronologies can be found in DuRoss *et al.* (2011) (Weber segment), Personius *et al.* (2012) (Brigham City segment), and Crone *et al.* (2014) (Nephi segment). Paleoseismic site data for the Nephi, Salt Lake City, and Provo segments are also discussed by DuRoss *et al.* (2008), DuRoss *et al.* (2014), and Olig *et al.* (2011), respectively. Legacy paleoseismic data for the central WFZ are summarized by Machette *et al.* (1992) and Lund (2005).

To combine two or more site PDFs into a single-segment PDF, we used both the product and mean methods of DuRoss *et al.* (2011). The product method takes the product of the probabilities for each common time bin in the site PDFs; the mean method takes the average of the individual site PDF probabilities. We relied primarily on the product method, which focuses on the overlap in the site PDFs, giving more weight to the best constrained PDFs from the sites that establish the tightest limits on earthquake timing. In this method, we used all of the site PDF data, rather than excluding or subjectively weighting the less well-constrained data. However, DuRoss *et al.* (2011) caution that the product method is best suited to paleoseismic datasets in which: (1) the OxCal models (and resulting site PDFs) are supported by geologic observations and judgment; and (2) the correlation of site PDFs to form a segment (or fault-rupture) chronology is consistent with earthquake-timing data (i.e., segment earthquakes constrained by overlapping site PDFs) and fault geometry and displacement information (e.g., site PDF correlation supported by mapped segment boundaries and per-event displacements). Thus, where the site PDFs contributing to a segment-wide earthquake have poor overlap, or the correlation of site PDFs from site to site is uncertain, we used the mean method to combine the site PDFs (Table B-6) because it more accurately represents the uncertainty in the earthquake time. See DuRoss *et al.* (2011) for a detailed description of these methods and their application to the Weber segment, and Personius *et al.* (2012) for their application to the Brigham City segment.

Brigham City Segment

Paleoseismic Data

The Brigham City segment (BCS) is the northernmost segment of the central WFZ that has evidence of Holocene surface rupture. The surface trace extends 35 km (all length measurements in this appendix are straight line, end-to-end) from a range-front reentrant near Coldwater Canyon near Honeyville to the southern terminus of the segment's Holocene faulting at the Pleasant View salient near North Ogden. At the Coldwater Canyon reentrant, scarps on Holocene to late Pleistocene surficial deposits form a zone of complex faulting that overlaps with the southern end of the Collinston segment (Personius 1990; Hylland, 2007). At the Pleasant View salient, complexly faulted late Pleistocene alluvial-fan deposits bury shallow bedrock on the hanging wall of the WFZ (Personius, 1990).

Paleoseismic data for the BCS span several decades and are dominantly from the northern half of the segment. Near Brigham City in the north-central part of the BCS, Personius (1991a) excavated a trench at the Bowden Canyon site. On the southern BCS, Personius (1991b) studied a modified gravel-pit exposure of a subsidiary fault trace on the Pleasant View salient at the Pole Patch site. Later, about 2 km south of Bowden Canyon, McCalpin and Forman (2002) excavated several trenches across a Lake Bonneville delta at the mouth of Box Elder Canyon. And most recently, DuRoss *et al.* (2012) excavated trenches at two sites on the northern BCS—the Hansen Canyon and Kotter Canyon sites—and one site on the southern BCS—the Pearsons Canyon site, which is about 6 km north of the southern end of the Holocene scarps on the segment. We constructed OxCal models for the Box Elder Canyon, Bowden Canyon, Kotter Canyon, and Pearsons Canyon paleoseismic sites. Earthquake times reported for these sites are the mean values and two-sigma (2σ) uncertainties from the OxCal models (Table B-1); see Personius *et al.* (2012) for an expanded discussion of the original paleoseismic data and the OxCal modeling results. We did not develop OxCal models for the Hansen Canyon and Pole Patch sites because the earthquake times are too broadly constrained.

At the Bowden Canyon (BC) site, Personius (1991a) exposed evidence for three Holocene surface-faulting earthquakes in a trench across an 8-m-high scarp. Based on minimum- and maximum-limiting radiocarbon (^{14}C) ages from bulk soil organics, the youngest earthquake (BC2) occurred at about 3.7 ± 0.5 ka and the preceding earthquake (BC3) at about 4.6 ± 0.6 ka. The oldest earthquake (BC4) is only constrained by minimum ages, and thus has a broadly constrained time of 5.8 ± 1.6 ka. Personius (1991a) did not find evidence for an earthquake younger than about 3.6 ka; however, the structure and stratigraphy in the trench was complicated and included multiple fault zones and extensive erosional unconformities. Personius (1991a, p. 6) noted the possible presence of an additional buried soil in the colluvial sequence, which permitted an alternative interpretation of an earthquake younger than about 3.6 ka. Considering this, as well as evidence from the adjacent Kotter Canyon and Box Elder Canyon trench sites (2 km to the north and south, respectively) where there is evidence of a post-3.6-ka earthquake, our OxCal model for the Bowden Canyon site includes an additional earthquake (BC1) at 2.6 ± 1.0 ka (see Personius *et al.* [2012] for discussion). Earthquakes BC3 and BC4 each produced about 2.5 m of vertical displacement, compared to about 1.0 m in BC2.

The Pole Patch (PP) trench revealed evidence for three surface-faulting earthquakes: two postdating the Bonneville highstand, and an MRE (PP1) that occurred prior to 4.5 ± 0.7 ka based on a ^{14}C age for bulk soil organics. Personius (1991b) estimated a time of 4.6 ± 0.5 ka for PP1. The two older earthquakes were broadly constrained between the age of the MRE and the time of the Bonneville flood at ~18 ka (based on Oviatt [1997]). Each of the older earthquakes produced about 1.5 to 2.5 m of vertical displacement, compared to about 0.7 to 1.3 m in PP1 (Personius, 1991b).

At the Box Elder Canyon (BEC) site, McCalpin and Forman (2002) excavated 14 trenches across a complex fault zone formed on a Lake Bonneville (Provo-phase) delta and used ^{14}C and thermoluminescence (TL) ages to constrain the timing of six surface-faulting earthquakes younger than ~8.5 ka. The youngest and best-constrained earthquakes occurred at 2.2 ± 0.6 ka (BEC1), 3.2 ± 0.5 ka (BEC2), 4.4 ± 1.1 ka (BEC3), and 5.6 ± 0.8 ka (BEC4). Two older, less well-constrained earthquakes occurred at 7.7 ± 1.5 ka (BEC5) and 9.5 ± 2.1 ka (BEC6). BEC1 and BEC2 had minimum vertical displacements of 1.1 m and 0.5 to 1.2 m, respectively (McCalpin and Forman, 2002). They reported only poorly constrained minimum displacements due to the complex fault zone, which complicated the measurement of total throw per event across the entire zone.

At the Hansen Canyon (HC) site, DuRoss *et al.* (2012) excavated two trenches across a 4-m-high scarp and exposed evidence of a single late Holocene surface-faulting earthquake. Four maximum and three minimum ^{14}C ages broadly constrained the time of the youngest earthquake (HC1) to 2.1 to 4.2 ka. DuRoss *et al.* (2012) attributed the broadly constrained time of HC1 to ^{14}C ages affected by both detrital charcoal (inherited ages) and burrowing. Because of the broad time range, which overlaps with BEC1–BEC3, we chose not to include HC1 in our analysis of BCS earthquake-timing data.

DuRoss *et al.* (2012) excavated one trench across an 8-m-high scarp at the Kotter Canyon (KC) site and found evidence of two late Holocene earthquakes. Based on OSL and charcoal ^{14}C ages, the youngest earthquake (KC1) occurred at 2.5 ± 0.3 ka and the penultimate earthquake (KC2) at 3.5 ± 0.3 ka. The timing of KC1 and KC2 corresponds well with Box Elder Canyon earthquakes BEC1 (~2.5 ka) and BEC2 (~3.2 ka) and Bowden Canyon earthquake BC2 (~3.7 ka). DuRoss *et al.* (2012) measured an average displacement of 2.1 ± 0.2 m for KC1 and KC2.

At the Pearsons Canyon (PC) site, DuRoss *et al.* (2012) excavated two trenches across a 2-m-high main scarp and a 0.2-m-high antithetic scarp north of Pearsons Canyon on the southern BCS. The trenches exposed evidence for a single earthquake, the timing of which is tightly constrained to 1.2 ± 0.05 ka (PC1) by multiple ^{14}C ages on charcoal from alluvial-fan deposits, scarp colluvium, and a post-earthquake debris flow. PC1 is much younger than the youngest earthquake on the northern part of the BCS at ~2.2 to 2.6 ka and likely represents a partial rupture of the southernmost BCS during an earthquake that ruptured the adjacent Weber segment (WS) to the south (discussed below and in DuRoss *et al.* [2012] and Personius *et al.* [2012]). About 0.5 m of vertical displacement (0.1–0.9 m range, which accounts for antithetic faulting) occurred in PC1 (DuRoss *et al.*, 2012).

Earthquake Chronology

The Kaysville, East Ogden, Garner Canyon, and Rice Creek trench investigations each yielded evidence for at least three large-displacement, surface-faulting earthquakes during the Holocene. DuRoss *et al.* (2011) correlated and combined these data into a record of five earthquakes at about 0.6 ka (W1), 1.1 ka (W2), 3.1 ka (W3), 4.5 ka (W4), and 5.9 ka (W5) (Table B-2). Based on their analysis, DuRoss *et al.* (2011) concluded that (1) W3, W2, and W1 likely ruptured the entire segment, although questions remain whether W2 ruptured the Kaysville site; (2) W4 was not exposed (or possibly not identified) at Kaysville; and (3) W5 was likely exposed at both Rice Creek and Kaysville, but predated the stratigraphic record exposed at East Ogden, supporting the inference of McCalpin *et al.* (1994) that Kaysville earthquake K4 (~5.7 ka) is a separate, older earthquake than East Ogden earthquake EO4 (~4.0 ka) (Table B-2). Although Nelson *et al.* (2006) had previously considered W1 a possible partial rupture confined to the northern WS, DuRoss *et al.* (2011) concluded that this earthquake ruptured at least from Rice Creek in the north to Kaysville on the south. Thus, consistent with DuRoss *et al.* (2011), we include W1 as a full rupture of the WS.

Weber Segment

Paleoseismic Data

The 56-km-long Weber segment (WS) is the second longest WFZ segment and extends from the Pleasant View salient to the Salt Lake salient near North Salt Lake. At the Pleasant View salient, a 1.5-km-wide left step separates the WS from the Holocene trace of the BCS (Personius, 1990; Nelson and Personius, 1993). At the Salt Lake salient, the WS terminates in Tertiary bedrock, close to an about 2-km-wide zone of en-echelon, right-stepping faults between the WS and the Warm Springs fault of the Salt Lake City segment (Nelson and Personius, 1993).

Paleoseismic data for the WS are from trench investigations at the Kaysville site on the southern WS (Swan *et al.*, 1980, 1981; later reoccupied by McCalpin *et al.*, 1994), the East Ogden site on the north-central part of the segment (Nelson, 1988; Nelson *et al.*, 2006), and the Rice Creek site on the northern WS (DuRoss *et al.*, 2009). Study of a cut-slope excavation 5 km north of East Ogden at the Garner Canyon site provided additional data on earthquake-times and displacements for the northern WS (Nelson, 1988; Forman *et al.*, 1991; Nelson *et al.*, 2006). We constructed OxCal models for all four WS sites, which yielded the mean and 2σ earthquake times discussed in Table B-2. See DuRoss *et al.* (2011) for an expanded discussion of the original paleoseismic data and OxCal modeling results.

At the Kaysville (K) site about 20 km north of the southern end of the WS, a 22-m-high fault scarp has been the subject of two trench investigations. In one of the first paleoseismic studies on the WFZ, Swan *et al.* (1980, 1981) excavated several trenches across the scarp and exposed evidence of at least three surface-faulting earthquakes. However, the two youngest earthquakes were only constrained by a maximum ^{14}C age of ~1.6 ka. In 1988, McCalpin *et al.* (1994) reexcavated the Kaysville site and used ^{14}C and TL ages to constrain the timing of three mid-Holocene earthquakes. However, based on the analysis of paleoseismic data discussed in DuRoss *et al.* (2011), we modeled four earthquakes at the site: 0.6 ± 0.2 ka (K1), 0.9 ± 0.5 ka (K2), 2.8 ± 1.7 ka (K3), and 5.7 ± 1.3 ka (K4). The addition of earthquake K2 stems from DuRoss *et al.*' (2011) review and synthesis of stratigraphic and structural data from both Kaysville investigations and the chronological constraints from McCalpin *et al*. (1994). Stratigraphic and structural evidence of K2 includes prominent fissures and likely scarp colluvium that predates K1 and postdates K3; furthermore, the incremental rotation of colluvial-wedge sediments into the fault zone, fault terminations, differential offset of stratigraphic horizons, and a possible buried fault scarp support the interpretation of an additional earthquake. Vertical displacement per event ranges from about 1.4 to 1.8 m (K1 and K4) to 3.9 m (K3) (McCalpin *et al.*, 1994).

At the East Ogden site (EO), Nelson (1988) excavated a total of five trenches across two main (west-facing) scarps having 5 and 8 m of vertical offset, and an antithetic scarp that has 2 m of vertical offset. He used ^{14}C ages on bulk-soil sediment and charcoal and TL ages on quartz-bearing sediment to limit the timing of four late-Holocene earthquakes. Based on limiting ages in Nelson *et al.* (2006), the earthquakes occurred at 0.5 ± 0.2 ka (EO1), 0.9 ± 0.4 ka (EO2), 3.0 ± 0.4 ka (EO3), and 4.0 ± 0.5 ka (EO4). Per-event vertical displacements are generally large, including 2.6 m in EO2 and 4.2 m in both EO3 and EO4 (Nelson *et al.*, 2006). Nelson *et al.* (2006) suggested that EO1—which only had about 0.5 m of displacement—may be a separate, younger earthquake than the youngest Kaysville (K1) and Garner Canyon (GC1) events, and thus, possible evidence of a partial segment rupture on the northern WS.

At the Garner Canyon (GC) site, Nelson *et al.* (2006) mapped the exposure excavated into a 4-m-high fault scarp and reported stratigraphic and structural evidence of four earthquakes. Based on the OxCal model of DuRoss *et al.* (2011), these earthquakes occurred at 0.6 ± 0.4 ka (GC1), 1.5 ± 0.5 ka (GC2), 3.2 ± 0.6 ka (GC3), and 4.4 ± 0.6 ka (GC4). Earthquakes GC4 and GC3 have no maximum age constraints; and thus, the timing of GC4 and GC3 is based on a plausible correlation of these events with earthquakes EO4 and EO3 at East Ogden (Nelson *et al.*, 2006). This correlation is supported by geologic mapping that shows similar amounts of vertical displacement on late Holocene alluvial fans at both Garner Canyon and East Ogden (Nelson and Personius, 1993). Per-event vertical displacements for GC1–GC3 range from about 1.0 m to 1.5 m (Nelson *et al.*, 2006).

DuRoss *et al.* (2009) excavated two trenches across 4-m- and 8-m-high main (west-facing) scarps and a 1-m-high antithetic scarp at the Rice Creek (RC) site, near the northern end of the WS. Based on ^{14}C ages on charcoal, OSL ages, and the OxCal model in DuRoss *et al.* (2011), the trenches exposed evidence for five earthquakes that occurred at 0.6 ± 0.08 ka (RC1), 1.2 ± 0.3 ka (RC2), 3.4 ± 0.7 ka (RC3), 4.6 ± 0.5 ka (RC4), and 6.0 ± 1.0 ka (RC5). DuRoss *et al.* (2011) concluded that earthquake RC1 at ~0.6 ka likely corresponds with events at ~0.6 ka at Kaysville (KC1), ~0.5 ka at East Ogden (EO1), and ~0.6 ka at Garner Canyon (GC1). DuRoss *et al.* (2009) included an additional earthquake (RC6, which occurred before 7.8–9.9 ka); however, the time of this event is poorly constrained by a single minimum-limiting age. Vertical displacements for individual earthquakes at Rice Creek ranged from about 1.1 m in RC3 to 3.2 m in RC2; RC1, RC4, and RC5 each had about 2.0 m of displacement.

Earthquake Chronology

The Kaysville, East Ogden, Garner Canyon, and Rice Creek trench investigations each yielded evidence for at least three large-displacement, surface-faulting earthquakes during the Holocene. DuRoss *et al.* (2011) correlated and combined these data into a record of five earthquakes at about 0.6 ka (W1), 1.1 ka (W2), 3.1 ka (W3), 4.5 ka (W4), and 5.9 ka (W5) (Table B-2). Based on their analysis, DuRoss *et al.* (2011) concluded that (1) W3, W2, and W1 likely ruptured the entire segment, although questions remain whether W2 ruptured the Kaysville site; (2) W4 was not exposed (or possibly not identified) at Kaysville; and (3) W5 was likely exposed at both Rice Creek and Kaysville, but predated the stratigraphic record exposed at East Ogden, supporting the inference of McCalpin *et al.* (1994) that Kaysville earthquake K4 (~5.7 ka) is a separate, older earthquake than East Ogden earthquake EO4 (~4.0 ka) (Table B-2). Prior to the Rice Creek study, Nelson *et al.* (2006) had interpreted W1 as a possible partial rupture that was confined to the northern WS, but we favor the interpretation that this earthquake ruptured at least from Rice Creek in the north to Kaysville on the south. See DuRoss *et al.* (2011) for further discussion.

Salt Lake City Segment

Paleoseismic Data

The Salt Lake City segment (SLCS) comprises three subsections (separate fault strands) that are separated by prominent left steps: the Warm Springs, East Bench, and Cottonwood faults (Scott and Shroba, 1985; Personius and Scott, 1992, 2009). The SLCS extends 40 km from the northern end of the Warm Springs fault, which bounds the western edge of the Salt Lake salient, to the southern end of the Cottonwood fault, where the Traverse Mountains and east-west oriented Fort Canyon fault separate the SLCS from the Provo segment (Bruhn *et al.*, 1992). The individual faults have end-to-end trace lengths of 7.5 to 10.5 km (Warm Springs fault), 12 km (East Bench fault), and 20 km (Cottonwood fault), and the step-over zones between them are 2–3 km (Cottonwood–East Bench faults) to 3–4 km (East Bench–Warm Springs faults) wide.

Paleoseismic data for the SLCS are from fault-trench investigations at the Little Cottonwood Canyon (LCC; Swan *et al.*, 1981; later reoccupied by McCalpin, 2002) and South Fork Dry Creek (SFDC) sites (Schwartz and Lund, 1988; Black *et al.*, 1996), both on the Cottonwood fault, and the Penrose Drive (PD) site on the East Bench fault (DuRoss *et al*., 2014; DuRoss and Hylland, 2015). Earthquake-timing data are not available for the Warm Springs fault because extensive surface disturbance and development along the fault trace has apparently eliminated all suitable study sites (DuRoss and Hylland, 2015). We constructed OxCal models for the LCC and SFDC sites; mean and 2σ earthquake times from these models are reported in Table B-3. OxCal models for the PD site are included in DuRoss and Hylland (2015); because the PD data were not available at the time of our SLCS analysis, our segment-wide earthquake times only reflect data from LCC and SFDC. However, the youngest PD earthquake times overlap well with older events at the LCC and SFDC sites, and if we had included them, this addition would have had only a minor (30–50-yr) effect on segment-wide earthquake times (Table B-3). See DuRoss *et al.* (2014) and DuRoss and Hylland (2015) for expanded discussions of the OxCal models for the SLCS. Paleoseismic data for the SLCS are also available from exploratory trenches across the East Bench fault (Dresden Place site; Machette *et al.*, 1992) and geotechnical studies of the Warm Springs fault (Robison and Burr, 1991; Simon-Bymaster, 1999); however, these studies did not yield information on the times of earthquakes, and are not included in our analysis.

Both Swan *et al.* (1981) and McCalpin (2002) trenched the LCC site. Swan *et al.* (1981) reported evidence for two or three Holocene earthquakes, but could only constrain the minimum time of the penultimate earthquake to the early Holocene. McCalpin (2002) reoccupied the LCC site and interpreted seven post-Bonneville age (<18 ka) earthquakes. Using paleoseismic data from McCalpin (2002) in an OxCal model, the four youngest earthquakes occurred at 1.3 ± 0.04 ka (LCC1), 2.1 ± 0.3 ka (LCC2), 4.4 ± 0.5 ka (LCC3), 5.5 ± 0.8 ka (LCC4). Two older earthquakes occurred at 7.8 ± 0.7 ka (LCC5) and 9.5 ± 0.2 ka (LCC6); however, McCalpin (2002) interpreted a period of seismic quiescence on the SLCS between about 9 and 17 ka. Using the total displacement (~7.5 m) across the lower of two fault zones, McCalpin (2002) estimated an average displacement of 1.8 m per event for the youngest four earthquakes. However, this average displacement estimate does not account for possible displacement on the upper (eastern) fault and thus could be a minimum value.

At the SFDC site, about 5 km south of LCC, Schwartz and Lund (1988) and Black *et al.* (1996) excavated trenches across six scarps and constrained the timing of four events. Based on the SFDC data, as well as the results of a geotechnical trench excavation at Dry Gulch (Black *et al.*, 1996), the four earthquakes occurred at 1.3 ± 0.2 ka (SFDC1), 2.2 ± 0.4 ka (SFDC2), 3.8 ± 0.6 ka (SFDC3), and 5.0 ± 0.5 ka (SFDC4). Average per-event displacement for SFDC is 1.5 to 2.5 m based on a debris-flow levee that was vertically offset by two and possibly three earthquakes (Black *et al.*, 1996; DuRoss, 2008).

Earthquake Chronology

LCC and SFDC paleoseismic data indicate that the four youngest surface-rupturing earthquakes on the segment occurred at about 1.3 ka (S1), 2.2 ka (S2), 4.1 ka (S3), and 5.3 ka (S4) (Table B-3). Our correlation of earthquakes between LCC and SFDC corresponds with that of McCalpin (2002) and DuRoss and Hylland (2015), and is also consistent with results from the PD site. The youngest PD earthquakes occurred at 4.0 ± 0.5 ka (2σ) (PD1) and 5.9 ± 0.7 ka (PD2), consistent with earthquakes at ~3.8 to 4.4 ka and ~5.0 to 5.5 ka at LCC and SFDC. McCalpin (2002) reported three earthquakes between about 6 ka and ~18 ka (timing of the highstand of Lake Bonneville), and discussed the possibility of a period of seismic quiescence on the SLCS between about 9 and 17 ka. Although our analysis of the SLCS is limited to the youngest four, late Holocene earthquakes, which corresponds with the time period over which the paleoseismic record for the central WFZ is likely complete, questions regarding the completeness of the early Holocene–latest Pleistocene earthquake record, and McCalpin's inference of an 8-kyr quiescent period are important. However, we note that data from the PD site show that two earthquakes occurred during this time period (PD4 at 10.9 ± 0.2 ka and PD5 at 12.1 ± 1.6 ka), which suggests that the apparent lack of earthquakes at LCC between 9 and 17 ka is likely related to an incomplete paleoseismic record rather than a quiescent interval. DuRoss and Hylland (2015) suggested that PD4 and PD5 could have ruptured the Cottonwood fault, but may have been difficult to recognize at LCC because of the fault zone's complexity and/or because of abundant soil carbonate in the deposits, which complicated the interpretation of depositional environments at LCC (McCalpin, 2002).

Provo Segment

Paleoseismic Data

The Provo segment (PS) bounds the eastern margin of Utah Valley and is the longest segment on the WFZ, consisting of three distinct subsections that have a total end-to-end length of 59 km. The segment extends from the Traverse Mountains salient and the Fort Canyon fault east of the Traverse Mountains on the north to an en-echelon, 5- to 9-km-wide, right-step with the Nephi segment near Santaquin on the south. Machette *et al.* (1992) informally subdivided the segment into three 17- to 24-km-long subsections: the American Fork at the northern end, the Central or Provo-restricted, and the Spanish Fork at the southern end. However, paleoseismic data strongly suggest that the entire segment typically ruptures during surface-faulting earthquakes (Lund *et al.*, 1991; Machette *et al.*, 1992) as originally proposed by Schwartz and Coppersmith (1984) and is consistent with our findings. However, given the length and complexity of fault trace geometry, the three subsections remain a convenient way to discuss the PS segment paleoseismic data and is used here.

A total of seven paleoseismic trench sites have been investigated along the Provo segment (Figure B-1), but only four of these sites had sufficient timing data available to explicitly be included in this analysis. Importantly, we do have paleoseismic data analyzed for each of the three PS subsections and these are discussed in more detail below. On the northern part of the PS, Forman *et al.* (1989) and Machette *et al.* (1992) excavated several trenches at the American Fork (AF) site about 10 km from the segment's northern end and immediately south of the mouth of American Fork Canyon. Near the center of the segment, Lund and Black (1998) excavated a trench at the Rock Canyon (ROC) site and studied a natural exposure of the fault along Rock Creek. Lund *et al.* (1991) excavated trenches across faulted late Holocene fans on the southern PS at two sites approximately one kilometer apart: two trenches at the Mapleton South (MS) site and two trenches at the Mapleton North (MN) site just east of the city of Mapleton. Olig *et al.* (2011) later reoccupied the MN site in a single, large (megatrench) excavation, which was excavated just north of the original MN trenches. We constructed OxCal models for the AF, ROC, MN (the original and megatrench combined) and MS sites using paleoseismic data from Machette *et al.* (1992), Lund and Black (1998), and Olig *et al.* (2011), and mean and 2σ earthquake times from those models are discussed here (Table B-4).

The three paleoseismic trench sites on the PS that are not included in this OxCal/Matlab analysis are Hobble Creek, Woodland Hills, and Water Canyon (Figure B-1), and the reasons are briefly explained here. At the Hobble Creek site, a few kilometers north of the MN site, Swan *et al.* (1980) and Schwartz *et al.* (1983) found evidence for six to seven surface-faulting earthquakes that produced 11.5 to 13.5 m of cumulative net vertical displacement since a Provo delta formed between 14,500 and 12,000 ^{14}C yr B.P. (revised Provo phase ages from Godsey *et al*., 2005). These data were calendar calibrated and used in this study to estimate slip rates, but unfortunately absolute age constraints for individual events were lacking, precluding construction of OxCal models for the Hobble Creek site.

At the Woodland Hills site, two trenches were excavated across a west-northwest-dipping splay fault above the highest Bonneville shoreline, termed the Woodland Hills fault by Machette (1992), which is about 6 km from the southern end of the PS. Machette (1992) reported evidence for three or four late Quaternary events on the Woodland Hills fault that produced about 3 m of vertical displacement, including a late Holocene event that he correlated to the MRE at MN, but given the large uncertainties in the legacy dates, it may actually correlate to the penultimate event observed at the MN site (discussed further below). Machette (1992) reported AMRT dates of 1190 ± 50 and 1380 ± 60 ^{14}C yr B.P. from a block of soil that had fallen off the free face and he interpreted these dates to provide a minimum estimate of 1.0 ± 0.3 ka since faulting (including calendar calibration and subtracting 200 years for soil formation). However, because trench logs and other age data were not available, and because of the issues with interpreting legacy bulk soil dates, we did not construct an OxCal model for this site.

The Water Canyon site is on the southern PS near the junction with the Woodland Hills fault. Here, the U.S. Bureau of Reclamation (USBR) excavated three trenches near a pipeline crossing for the Central Utah Project. They exposed evidence for at least four or possibly five surface-faulting events since 4,600 ± 75 ^{14}C yr B.P., including two events in one trench that were younger than 890 ± 75 ^{14}C yr B.P. based on a bulk sample ^{14}C date from an A horizon underlying the penultimate event colluvial wedge (D. Ostenaa, USBR, personal communication, cited in Olig *et al.*, 2011). Unfortunately, the investigation remains unpublished except for an abstract (Ostenaa, 1990). We reviewed copies of field logs made by Michael Machette that were available from UGS files, but the limited documentation made constructing detailed OxCal models for the Water Canyon site beyond the scope of this study, although additional time and resources might make this a worthwhile future endeavor.

At the AF site, Forman *et al.* (1989) and Machette *et al.* (1992) excavated three trenches (AF-1 through AF-3) across most, but not all, of the complex distribution of overlapping post-Bonneville fault scarps at this site. They found evidence for at least four surface-faulting earthquakes that occurred since 8 ka, but we emphasize that this paleoseismic record is a minimum for this site because the ages of the youngest colluvial wedges exposed on two different west-dipping late Holocene fault scarps (the eastern fault splay in Trench AF1 and the main fault in Trench AF-3) were not constrained. In addition, the easternmost, west-dipping fault scarp at the site was not trenched due to landowner restrictions (see Figure 3 of Machette *et al.*, 1992). Our OxCal model for the AF site is based on the published paleoseismic data (Machette *et al.*, 1992) and review of original field logs from USGS file archives (including previously unpublished logs for Trenches AF-2, AF-3, and the eastern part of Trench AF-1), as well as discussions of these data with M.N. Machette (U.S. Geological Survey [retired], written communication, 2011). Based on our OxCal analysis, the four earthquakes occurred at 0.4 ± 0.2 ka (AF1), 2.0 ± 0.8 ka (AF2), 4.3 ± 1.5 ka (AF3), and 6.2 ± 1.0 ka (AF4). During review of field logs, we considered but ultimately discounted suggestive stratigraphic evidence for a possible younger event in trench AF-2 that would have occurred at 0.3 ± 0.1 ka, but only apparently on an antithetic fault. The average per-event vertical displacement for AF1–AF3 is 2.5 ± 0.3 m, based on the total displacement at the site divided by the number of events (Machette *et al.*, 1992).

At the ROC site, Lund and Black (1998) excavated a trench and studied a natural exposure of the fault and found evidence of a single surface-faulting earthquake since about 2 ka. Several ^{14}C ages on bulk soil and charcoal constrain the earthquake time (ROC1) to 0.6 ± 0.06 ka from our OxCal analysis of the data. Based on the stratigraphic separation measured across the entire deformation zone, Lund and Black (1998) measured about 3.3 m of net vertical displacement for ROC1. Finally, we emphasize that not all fault scarps on unconsolidated deposits were trenched at this site, including scarps on various Lake Bonneville deposits (see Figure 3 of Lund and Black, 1998).

Near Mapleton, both Lund *et al.* (1991) and Olig *et al.* (2011) excavated trenches across a 19- to 23-m-high scarp. At the MN site, Lund *et al.* (1991) excavated two trenches across the lower one-third of the scarp and found evidence of two surface-faulting earthquakes, but were only able to date the youngest event at 0.6 ± 0.2 ka. Olig *et al.* (2011) reoccupied the site and excavated a single, large trench across the entire 50-m-wide deformation zone, which revealed evidence of at least seven, probably ten, surface-faulting earthquakes that occurred since 13 ka. We combined the paleoseismic data from these two studies to construct a single OxCal model for the MN site. Based on our analyses, earthquakes occurred at 0.6 ± 0.08 ka (MN1), 1.5 ± 0.4 ka (MN2), 3.2 ±

1.3 ka (MN3) 4.7 ± 0.3 ka (MN4), and 5.6 ± 0.5 ka (MN5). Estimates of per event vertical displacement from the MN site used in this analysis are: 4.7 ± 0.5 m for MN1, and a minimum of 0.5 to 2.2 m for MN2 (Olig *et al.*, 2011).

About 0.8 km south of the MN site, Lund *et al.* (1991) excavated three trenches across two west-facing scarps at the MS site, but they only logged one trench in detail because suitable material for dating was not found in the other two trenches. They found evidence for two events since about 3 ka, but the time of the youngest event was poorly constrained. Based on our OxCal analysis of their data, surface-faulting earthquakes occurred at 0.7 ± 0.7 ka (MS1) and 2.2 ± 0.8 ka (MS2). Reliable estimates of per event displacement could not be made at MS because of incomplete exposure of the deformation zone (Lund *et al.*, 1991).

Based on these earthquake times, MS1 likely correlates with MN1 (and AF1), whereas MS2 likely correlates with MN3 and AF2, with MN2 only identified at the MN site, because it was not exposed or dated at other sites, or because it did not rupture elsewhere, which seems less likely given the relatively large displacements for this event (Olig *et al.*, 2011). However, given the timing uncertainties of events, we also considered correlations among AF2, MN2, and MS2, with paleoearthquake MN3 as the additional event not identified at the other sites. However, we ultimately preferred the former correlation (AF2, MN3, and MS2) because it has a better overlap between PDFs of event times, although we acknowledge that additional paleoseismic investigations of the PS are needed to better determine the extent of the MN2 rupture and verify the AF2, MN3, and MS2 correlation of events.

Earthquake Chronology

At least five post-mid-Holocene earthquakes have caused surface-rupture on the PS: 0.6 ka (P1), 1.5 ka (P2), 2.2 ka (P3), 4.7 ka (P4), and 5.9 ka (P5) (Table B-4). These earthquake times are based on our review of PS paleoseismic data from all of the study sites and our preferred correlation of earthquakes along the segment. Based on our analysis, we consider the post-mid-Holocene earthquake record complete for the MN site because it includes earthquake P2 (MN2) that occurred at ~1.5 ka. In our analysis, we have assumed events A2, MN3, and MS2 correlated in the P3 rupture, and P2 either did not rupture the full extent of the PS or evidence of it was not exposed at the AF, ROC, and MS sites. The relatively large displacement of 0.5 to 2.2 m for MN2 supports the latter. Additionally, for AF and MS, the latter explanation is more plausible because ages of at least two colluvial wedges exposed in the AF trenches were poorly constrained and could correlate to MN2, as well as the AF trenches did not span all of the fault traces (the easternmost down-to-the west fault trace in a complex zone was not trenched), and at the MS site, only the lower part of a large, complexly faulted scarp was exposed in the trench that was logged. At ROC, P2 postdates the oldest buried soil at the site (dated to about 2.4 ka; Lund and Black, 1998), but considering the limited exposure of the soil (not exposed in the fault zone) and additional fault traces (on older unconsolidated sediments, but showing evidence of complex surface faulting) both east and west of the ROC site that were not trenched, we consider it possible that P2 ruptured the ROC site, but was not exposed.

Nephi Segment

Paleoseismic Data

The Nephi segment (NS) is the southernmost segment of the central WFZ that has evidence of multiple Holocene surface-faulting earthquakes. The NS extends 43 km and comprises two subsections—a 17-km-long northern strand and a 25-km-long southern strand—which are separated by a 4- to 5-km-wide right step in bedrock. The northern strand extends along a steep range front from near Santaquin Canyon northward into southern Utah Valley where it overlaps the southern PS by 12 km (Machette, 1992). The southern strand bounds a steep range front in eastern Juab Valley and terminates to the south at a 7-km-wide gap in faulting between the Nephi and Levan segments (Harty *et al.*, 1997).

Paleoseismic data for the NS are from three trench sites on the southern strand and one site on the northern strand. At North Creek (NC) on the northern part of the southern strand, Hanson *et al.* (1981, 1982a) excavated several trenches, and at Red Canyon (REC) on the southern part, Jackson (1991) excavated one trench near the southern terminus of the NS (12 km south of North Creek). Both investigations found evidence for three surface-faulting earthquakes. Machette *et al.* (2007) excavated trenches at the Willow Creek (WC) site midway between the NC and REC sites). At the Santaquin (SQ) site on the northern strand, DuRoss *et al.* (2008) excavated trenches across a single-event scarp near the center of the strand. We constructed OxCal models for all NS sites (included in DuRoss, 2014), which yielded the mean and 2σ earthquake times discussed here (Table B-5). Horns *et al.* (2009) excavated trenches on the northern strand for geology field courses; however, these limited data are only published in an abstract, and thus, we do not include them in our analysis. In 2012, the UGS and USGS reoccupied the NC site and excavated a trench on the northern strand near Spring Lake to help resolve the timing of large earthquakes on the NS; however, results were not available at the time of this analysis.

At the NC site, Hanson *et al.* (1981) excavated three trenches, and exposed stratigraphic evidence for two surface-faulting earthquakes. They used six maximum and two minimum ^{14}C ages on bulk soil and charcoal fragments to constrain the timing of NC1 to 0.4 ± 0.5 ka. The young age of this earthquake is consistent with the steep scarp angles and the presence of a stream-channel nickpoint in North Creek just above the scarp (Hanson *et al.*, 1982b). The timing of older earthquakes is complicated by ^{14}C ages that cluster in two groups (~1.3–1.4 ka and 3.7–4.1 ka). Based on the discussion of these data in DuRoss *et al.* (2008), and considering radiocarbon-dating limitations and uncertainties discussed by Nelson *et al.* (2006) and DuRoss *et al.* (2011), we used the younger limiting ages to model earthquake times at 1.4 ± 0.3 ka (NC2) and 1.9 ± 0.5 ka (NC3). This differs from the interpretation of Hanson *et al.* (1982a, 1982b), who preferred the older ages, concluding that the younger ages "may represent younger material incorporated into the soil prior to burial." NC1 and NC2 both had about 2.1 to 2.3 m of per-event vertical displacement (Hanson *et al.*, 1981).

At the REC site on the southern strand, Jackson (1991) excavated one trench and found evidence for three Holocene surface-faulting earthquakes. The OxCal model for the REC site is based largely on the discussion and analysis of REC data included in DuRoss *et al.* (2008), and includes ^{14}C ages on bulk soil and TL ages that constrain the timing of these earthquakes to 0.5 ± 0.5 ka (REC1), 1.2 ± 0.3 ka (REC2), and 4.7 ± 2.5 ka (REC3). The large (2.5-kyr) uncertainty for REC3 stems from the lack of a numerical maximum constraining age for that event. Jackson (1991) inferred that REC3 occurred after deposition of the REC alluvial fan at approximately 7 to 15 ka. Per-event vertical displacements range from about 1.4 m (REC1) to 1.7 m (REC3) (Jackson, 1991).

A trench investigation on the southern strand at the WC site by Machette *et al.* (2007) improved the late-Holocene (younger than about 2.5 ka) earthquake chronology for the southern strand. They used ^{14}C and OSL ages to constrain the timing of three surface-faulting earthquakes to 0.2 ± 0.09 ka (WC1), 1.2 ± 0.1 ka (WC2), and 2.0 ± 0.5 ka (WC3). Machette *et al.* (2007) also found indirect evidence for at least one earlier earthquake (WC4) based on the 6.2 ka age and minimum offset of footwall alluvial-fan sediments exposed in the trenches. However, they did not expose stratigraphic (*e.g.*, colluvial-wedge) evidence of the additional earthquake(s) in their trenches. Based on the time range for earthquake WC3 and 6.2 ka OSL ages for sediments exposed in the footwall of the fault, WC4 is poorly constrained to 4.7 ± 1.8 ka. Machette *et al.* (2007) did not calculate per-event vertical displacements for WC1–WC3.

On the northern strand, DuRoss *et al.* (2008) excavated trenches across a scarp having 3 m of vertical surface offset at the SQ site and found evidence of one surface-faulting earthquake. DuRoss *et al.* (2008) modeled a time for the Santaquin earthquake (SQ1) of 0.5 ± 0.2 ka based on two ~0.5-ka charcoal ages for a pre-faulting soil that provide a maximum constraint and a charcoal age of ~0.4 ka for scarp colluvium that provides a minimum constraint. However, considering the similarity in the maximum and minimum ages, it is possible that the 0.4-ka charcoal was recycled from the pre-faulting soil exposed in the footwall. Thus, we modeled an SQ1 time of 0.3 ± 0.2 ka (this study) by excluding the 0.4-ka minimum age. Considering both possibilities, the broadest possible time range for SQ1 is ~0.1–0.7 ka, which overlaps with both the youngest earthquake on the southern strand of the NS (~0.2 ka at WC) and the youngest earthquake on the PS (~0.6 ka). DuRoss *et al.* (2008) did not find evidence of a penultimate earthquake at the SQ site; however, this earthquake likely occurred prior to 1.5 ka based on soil charcoal, or possibly prior to 6.9 ka based on detrital charcoal from alluvial-fan sediments. About 3.0 m of vertical displacement occurred in SQ1 (DuRoss *et al.*, 2008).

Earthquake Chronology

Based on our analyses of these paleoseismic data (see expanded discussion in Crone *et al.*, 2014) and the discussion of these data in DuRoss *et al.* (2008), we model four late to middle Holocene earthquakes on the NS that occurred at 0.2 ka (N1), 1.2 ka (N2), 2.0 ka (N3), and 4.7 ka (N4) (Table B-5). These earthquake times rely heavily on the WC study, which found good evidence of three earthquakes younger than ~2.5 ka, and indirect evidence for an additional earthquake N4 (WC4) (Table B-5). We used the WC4 time (4.7 ± 1.8 ka) to define the N4 time, excluding REC earthquake REC3 (4.7 ± 2.5 ka) due to its larger 2σ uncertainty. Given their very broadly constrained (uniformly distributed) earthquake-timing PDFs, and the 6-km distance between the WC and REC trench sites, we did not correlate WC4 and REC3. In addition, we considered, but did not use the youngest earthquake on the northern strand from the SQ site (SQ1, 0.3 ± 0.2 ka, this study) to define the N1 time due to the uncertainty in the timing and rupture extent of the SQ1 earthquake. Given this uncertainty in earthquake timing, SQ1 could correlate with either the youngest earthquake on the southern strand (best constrained by WC1 at ~0.2 ka) or the youngest earthquake on the PS (P1 ~0.6 ka) (Crone *et al.*, 2014). While we consider it more likely that SQ1 corresponds with WC1, including SQ1 does not affect the N1 time because of the broad SQ1 uncertainty or N1 rupture extent because the Santaquin site is within the rupture-extent uncertainty we defined for northern NS (see Section 4.1.6). Finally, excluding SQ1 is consistent with DuRoss *et al.* (2008), who considered multiple SQ1 correlation possibilities, but ultimately had insufficient data to draw conclusions regarding the behavior of the northern strand.

EARTHQUAKE RECURRENCE AND FAULT SLIP RATES

Earthquake Recurrence Intervals

Earthquake recurrence intervals, which describe the time between large earthquakes on a fault or segment, and the elapsed time since the MRE (a minimum recurrence interval) are critical for modeling time-dependent earthquake probabilities. For each central WFZ segment, we calculated individual (inter-event) and mean recurrence intervals using our revised earthquake times (Table B-6). Because the segments have limited earthquake records (yielding only three to four inter-event intervals), we also grouped the individual recurrence intervals for the central segments and calculated a composite mean recurrence interval for the central WFZ. Although grouping the intervals does not serve to increase the length of the record, it does increase the number of inter-event observations and allow for calculation of a more robust late Holocene mean recurrence interval. Recurrence intervals discussed here do not account for sample-size uncertainties.

Mean Recurrence per Segment

We calculated earthquake recurrence intervals for each central WFZ segment using a Monte Carlo model (with 10,000 simulations) to randomly sample the segment PDFs. In each segment-specific simulation, we used earthquake times sampled from the original segment PDFs (e.g., for B1 to B4; Figure B-3) to define time intervals over which the earthquakes and closed seismic intervals occurred. We calculated inter-event recurrence (e.g., the B4–B3 time; Table B-6) and closed mean recurrence, which is the total elapsed time between the oldest and youngest earthquakes divided by the number of closed intervals between them (e.g., the total time between earthquakes B4 and B1 divided by 3; Table B-7). We also calculated open mean recurrence intervals using the total elapsed time from the maximum age constraint on the oldest event (e.g., 5.9 ± 0.4 ka for B4; Table B-7) to the present (time of analysis, 2011) divided by the number of earthquakes that occurred in that period (open mean recurrence; B4 maximum age to the present divided by 4). This calculation yields an approximate maximum likelihood value for open recurrence, or the number of events per unit time (*N*-in-*T*).

The resulting recurrence estimates were filtered to eliminate values less than 195 ± 165 yr (2σ), which DuRoss *et al.* (2011) used as an estimated minimum time required to degrade a fault-scarp free face and begin to deposit scarp-derived colluvium along the rupture in a semiarid environment. The minimum time likely ranges from approximately a few tens to a few hundred years based on the elapsed times since the Borah Peak, Idaho, earthquake rupture (~30 yr) (which is now forming colluvial wedges; Crone and Haller, 2004) and the most recent earthquake on the NS (less than ~360 yr). The filtered inter-event recurrence intervals are similar (less than 10-yr difference) to those determined without a minimum time, with the exception of estimates for B4-B3, W2-W1, P3-P2, and N4-N3, where the filtered recurrence estimates are about 20 to 70 yr longer than the unfiltered results because of overlapping segment PDFs (Figure B-3). The filtered recurrence intervals do not significantly affect mean recurrence estimates for the segments (less than 10-yr difference compared to unfiltered mean recurrence). We converted the recurrence values from all simulations into probability plots (PDFs) and calculated the mean and 2σ values reported in Table B-7.

Inter-event intervals for the central WFZ segments show moderate variability (Table B-6). For example, the youngest four earthquakes (B4 to B1) on the BCS yield consistent inter-event intervals of 1.0 to 1.1 kyr; however, about 2.5 kyr have elapsed since the most recent BCS earthquake, B1. Inter-event intervals for the WS, SLCS, PS, and NS are also irregular, ranging from about 0.7 kyr to 2.7 kyr, and varying by a factor of 2.4–3.5 per segment. For example, although two inter-event intervals for the WS are ~1.4 kyr (W5–W4 and W4–W3), the longest interval of 1.9 kyr for W3–W2 is 2.9 times greater than the 0.7-kyr interval for W2–W1. These inter-event intervals are useful for understanding and comparing the variability in earthquake recurrence on the central WFZ, but they do not necessarily represent the longer-term mean recurrence for the segments.

Closed mean recurrence intervals per segment (Table B-7) are based on the number of closed seismic intervals in the time between the oldest (generally mid-Holocene and youngest earthquakes (Table B-6). With the exception of the NS, the mean recurrence intervals are similar, ranging from 1.1 kyr on the BCS to 1.3 kyr on the WS, SLCS, and PS. These similar mean recurrence intervals reflect the most current earthquake data per segment and form the basis for our composite (grouped) central WFZ recurrence estimate (discussed below). The NS has a shorter mean recurrence interval of 0.9 kyr; this value is based on only two intervals between N3 and N1. The closed mean recurrence for the NS is 1.5 kyr if calculated using the N4–N1 time. However, we are not confident in this recurrence value because of the large uncertainty in the timing of N4 and concerns about the completeness of the earthquake record between N3 and N4 (*i.e.*, we do not correlate WC4 [4.7 ± 1.8 ka] with REC3 [4.7 ± 2.5 ka], which could be evidence of two separate NS earthquakes).

Open mean (*N*-in-*T*) recurrence intervals (Table B-7) are very similar to the closed mean recurrence intervals, with differences related to the elapsed time since the MRE or the time between the oldest earthquake and its maximum age constraint. The open mean recurrence values for the WS, SLCS, and PS are within about 0.1 kyr of the closed mean values. The BCS has the largest difference between the two values (~1.1 kyr–mean, ~1.5 kyr–open) because of the long elapsed time since its MRE (2.5 kyr). The NS has an intermediate (~0.2-kyr) difference in the recurrence values (~0.9 kyr–mean, ~1.1 kyr–open), which stems from the 1.2-kyr elapsed time between N3 (~2.0 kyr) and its maximum limiting age (~3.2 kyr).

Composite Recurrence for the Central WFZ

We calculated a composite mean recurrence interval for the central WFZ (Figure B-5) based on the observation that the central five segments essentially behave in a similar manner—that is, they have similar long-term (post-Provo) slip rates and recurrence of surface rupture. The advantage of a composite recurrence interval is that the sample size for closed intervals increases from 2–4 per segment to 16 for the central WFZ, which yields a more statistically robust mean recurrence estimate for the region.

We calculated the composite closed (inter-event) recurrence interval by grouping and then sampling each of the 16 inter-event recurrence distributions (PDFs) in 10,000 simulations. In each simulation we (1) sampled each of the inter-event PDFs, yielding a subset of 16 recurrence values (one for each of the inter-event pairs, such as W5–W4), (2) calculated the mean recurrence of this composite subset, and (3) compiled these composite mean recurrence values (n = 10,000). The mean and 2σ range of the composite mean dataset, or distribution of means calculated in the simulations, is 1.2 ± 0.1 kyr (5^{th}–50^{th}–95^{th} values of 1.1–1.2–1.3 kyr) (Figure B-5). For comparison, we also calculated a composite mean by grouping all of the inter-event values (n = 160,000), rather than taking the mean in each simulation. This method conveys the full distribution of possible recurrence estimates given the initial recurrence distributions (e.g., W5–W4). As expected, the calculation results in a greatly increased width of the recurrence distribution because all of the individual recurrence values are included and treated equally, rather than grouped in individual simulations to generate mean values. This alternate composite recurrence interval (for all recurrence records) is 1.2 ± 1.1 kyr (2σ). Ultimately, the composite mean calculated using the mean per simulation better reflects the average recurrence behavior of the central WFZ as it limits the effect of the end-member recurrence values at the tails of the recurrence distributions (e.g., 82 yr between W2 and W1 or 2966 yr between P4 and P3 at 2σ). However, we caution that the uncertainty represents the distribution of the mean values, rather than the complete dataset, and does not include sample-size uncertainties.

Coefficient of Variation on Recurrence

The coefficient of variation (COV) on recurrence, the standard deviation of inter-event recurrence intervals divided by their mean, is a measure of the periodicity of earthquakes on a fault. The smaller the COV, the more periodic is the recurrence. A large COV value indicates a more variable time interval between earthquakes. For example, a COV of 0.1 reflects very periodic recurrence behavior, whereas a COV of 1.0 indicates that recurrence is essentially random. The WGCEP (2003, 2008) used a COV of 0.5 ± 0.2 based on a global dataset of repeating earthquake sequences (Ellsworth *et al.*, 1999).

To test the suitability of the global COV to the central WFZ, we calculated a composite COV for the central WFZ using inter-event recurrence times between earthquakes on each of the five segments (e.g., those for BCS earthquakes B4–B3 and WS earthquakes W5–W4) (Figure B-6). We did not use recurrence times between earthquakes on different segments (e.g., the time between W4 and B4), which would yield significantly shorter recurrence times (mean of ~300 yr). We only calculated a single (composite) COV for the central WFZ because inter-event recurrence data per segment are limited (2–4 intervals per segment). The basis for the composite COV is similar mean recurrence parameters for the individual segments. Grouping the inter-event recurrence data allowed us to calculate a more statistically robust COV; however, the estimate does account for sample-size uncertainties

To compute the composite COV for the central WFZ, we compiled 16 inter-event-recurrence PDFs and sampled them in a Monte Carlo model. We used the recurrence PDFs filtered for the minimum recurrence value of ~195 ± 165 yr (described above) in our calculations; however, we achieved similar results (COV within 0.01) using the inter-event recurrence estimates not filtered for a minimum time. We did not include open intervals (e.g., the elapsed time since the most recent earthquake per segment) in our COV calculation. We sampled the group of inter-event recurrence PDFs through 10,000 simulations; each simulation randomly selected a single recurrence value from each inter-event recurrence PDF and added it to a group of recurrence values. That is, in each simulation, one recurrence value was selected for B4–B3, one for W4–W3, etc., thus forming a set of 16 recurrence intervals from which we calculated the COV (standard deviation divided by the mean of the 16 recurrence intervals). This process was repeated in each simulation, yielding a dataset of COV values, from which we determined the mean and 2σ standard deviation. Although sampling the inter-event distributions yield combinations of inter-event times that violate the paleoseismic records per segment (e.g., summed inter-event times exceeding the total record length), these combinations occur infrequently, for example, when the large-recurrence tails of several inter-event distributions are sampled concurrently. Thus, their contribution to the model results, while adding slight variance, is considered insignificant.

For comparison, we again followed this method but segregated the sampled recurrence PDFs by segment and computed segment-specific COVs, which we then summed to form a composite COV (Figure B-6). In this method, poorly constrained data (e.g., the NS COV based on only two recurrence intervals) receive equal weight as better constrained data (e.g., the WS COV based on four recurrence intervals). Both contributed about 20% (1/5) to the composite COV value. However, we have greater confidence in the composite method rather than the segment-specific method because individual recurrence records are combined and thus have less impact on the final COV value. For example, the four WS recurrence intervals contribute 25% (4/16) to the composite COV whereas the two NS intervals only contribute 12.5% (2/16).

The composite COV for the central WFZ is 0.5 ± 0.1 (2σ), with a minimum–maximum range of about 0.3 to 0.7 (Figure B-6). Although the composite approach yields the most robust mean COV for the region, COV estimates for the individual segments show more variability. The per-segment COVs range from 0.3 ± 0.4 (NS) to 0.6 ± 0.3 (PS); however, each is based on a small dataset (two to three inter-event periods). Summing the per-segment COV PDFs yields a per-segment composite COV with a mean and 2σ uncertainty of 0.4 ± 0.4. As discussed above, the composite COV is a more robust estimate for the central WFZ as a whole as it is based on a larger (grouped) sample set. The composite COV for the WFZ is similar to the value of 0.5 ± 0.2 used by the WGCEP (2003, 2008). The consensus of the WGUEP is to use a central WFZ COV of 0.5 ± 0.2 based on the global COV (Ellsworth *et al.*, 1999) and calculated composite COV mean (0.5) and possible range of uncertainty (± ~0.2).

Vertical Displacement

Vertical Displacement per Earthquake and Rupture Source

We compiled data to estimate the vertical displacement per site and for each surface rupture (Table B-8) for the central WFZ. These data are derived from the original paleoseismic-data sources discussed above (summarized and discussed in DuRoss [2008]), and also include recently obtained data from the HC, KC, and PC sites (DuRoss *et al.*, 2012), RC site (DuRoss *et al.*, 2009), and PD site (DuRoss *et al.*, 2014; DuRoss and Hylland, 2015). Using our correlation of site events along the segments (Tables B-1 to B-5), we combined individual vertical displacements per site into mean and minimum–maximum range displacements per rupture (e.g., for events B1 through B4; Tables B-8 and B-9), and ultimately, mean displacement per rupture source (e.g., for the BCS; Table B-10). We discuss these methods and results for single-segment ruptures; mean displacements for combinations of rupture sources (multi-segment ruptures) are discussed in the Rupture Models for the Central WFZ section.

To estimate the displacement per single-segment earthquake, we plotted the location of the site displacements along a rupture and modeled the average displacement for that rupture based on the well-documented observation that displacement tapers toward the ends of a surface rupture (Hemphill-Haley and Weldon, 1999; Biasi and Weldon, 2006; Wesnousky, 2008; Biasi and Weldon, 2009) (Figure B-7). Our approach is similar to that of Chang and Smith (2002), who fit analytical (ellipse-shaped) displacement profiles to central WFZ site displacements by varying the maximum height (displacement) of the ellipse. However, rather than fixing the shape of the displacement curve, we also allowed its shape to change by using the function $([\sin(\pi x/L)]^n)h$ (after Biasi and Weldon, 2009), where x/L is the normalized distance along the rupture (in 0.1-km increments), h controls the maximum height of the displacement curve, and n controls its shape. To achieve this, we (1) compiled displacement observations (and uncertainties) along each earthquake rupture that we modeled (Table B-8); (2) computed a suite of analytical displacement curves for each rupture having a large (several meter) range of maximum heights (h) and shapes (exponent n) varying from mostly flat or uniform (n=0.1) to peaked (n=0.9); and (3) used a least-squares regression to determine a best-fit analytical displacement curve that minimized the error between the modeled and observed displacements (sum of squared deviation from the displacement observations). For ruptures having two or more displacement observations, we took the least-squares, best-fit displacement curve, which most closely matched the observations, sampled it every 0.1 km, and calculated a modeled mean displacement (Figure B-7). For ruptures having only one displacement observation or two closely spaced observations, we arbitrarily fit three displacement curves to the data with flat, half-ellipse, and peaked shapes (exponent n values of 0.2, 0.5, and 0.8, respectively, while allowing h to vary), then sampled and computed the means for these profiles, and computed the mean displacement for the rupture by averaging these three means. To account for uncertainty in rupture displacement, we followed these methods using the mean, minimum, and maximum site displacements in separate models (Table B-9). Thus, the minimum and maximum displacements for a rupture are based on a best-fit displacement curve that fits the minimum and maximum site displacements, respectively. The modeled mean displacements per rupture are summarized as displacement per rupture source in Table B-10.

An important question is whether our best-fit displacement curve method reasonably models average displacement for historical normal-faulting earthquakes. We tested our method using along-strike displacement observations from historical normal-faulting earthquakes compiled by Wesnousky (2008). We were able to closely approximate the mean rupture displacement, even if the rupture had an asymmetric shape. Our least-squares mean displacements varied by 0 to 13% from mean displacements based on field observations and mean displacements from rupture profiles with points interpolated between observations (Wesnousky, 2008). For example, our best-fit displacement curve for displacement observations from the 1983 Borah Peak earthquake rupture indicates an average displacement of 0.8 m (Figure B-7), which is the same value for the average displacement based on interpolation of Wesnousky's (2008) displacement profiles.

Vertical Displacement per Source

We determined mean displacement per rupture source (i.e., per segment; Table B-10) by taking the mean of the modeled per-rupture displacements (based on displacement curves calculated using the mean observed displacements). Minimum and maximum displacements per source are based on the smallest and largest modeled displacements per rupture (based on displacement curves calculated using the minimum and maximum observed displacements, respectively). The modeled mean displacements per source range from 1.7 m for the BCS and SLCS to 2.6 m for the PS (Figure B-8). These yield a mean displacement for the central WFZ of 2.1 m, which is similar to the unmodeled mean of 2.0 m, and a mean of 2.2 m reported by DuRoss (2008), but based on a subset of the data used in this analysis. Limitations of these data include assumptions regarding the position of the displacement observation along the rupture and several individual rupture displacements that are based on only one to two displacement observations (e.g., B1; Table B-8). However, despite the sparse data (not all sites yielded displacement observations for each rupture), per-rupture displacements are similar for each rupture source (Table B-9).

Vertical Slip Rate per Segment

We used the mean displacements per earthquake rupture and per single-segment rupture source, the individual earthquake times, and the open and closed mean recurrence intervals to calculate vertical slip rates for the central WFZ segments (Table B-11) and for the central WFZ as a whole (composite slip rates). For each segment, we determined (1) a closed-interval slip rate using the modeled mean displacement for the segment (Table B-10) divided by the segment's closed mean recurrence interval (Table B-7), (2) an open-interval slip rate for which we used the total displacement in the time period defined by the maximum limiting age for the oldest earthquake to the present (Tables B-7 and B-11), and (3) long-term rates based on the vertical offset of geomorphic surfaces related to the latest Pleistocene-age Provo phase (14.0–17.6 ka; Godsey *et al.*, 2005, 2011) and highstand (about 17.6 ± 0.3 ka; based on Oviatt, 1997) of Lake Bonneville (Table B-11). We calculated composite slip rates comprising (1) a composite, long-term slip rate based on eight long-term (latest Pleistocene) slip rates (Table B-11), and (2) a composite, closed-interval, mean slip rate for which we used the mean of the average displacements per segment divided by the closed-interval mean composite recurrence interval for the central WFZ. We report a weighted mean slip rate per segment that uses these slip rates and a weighting scheme described below and in Table B-12.

We calculated weighted-mean slip rates for the central WFZ segments using two weighting schemes (Table B-12) that stem from expert opinion. For the WS, SLCS, and PS, the weighted mean slip rate is based on the closed mean slip rate per segment (0.35 weight), the composite closed mean slip rate for the central WFZ (0.35 weight), and the composite long-term (latest Pleistocene) slip rate for the central WFZ (0.3 weight). The closed mean slip rates received the greatest weight (0.35 each) as the earthquake records and mean recurrence intervals for these segments are well constrained. We did not use the open-interval slip rates for these segments because of the robust closed recurrence data. The long-term rate received slightly less weight (0.3) on account of the spatial distribution of geologic units and surfaces used to make the displacement measurements, which are generally limited in horizontal extent and clustered nonuniformly along the fault (generally at the segment boundaries). For the BCS and NS, we used the composite long-term slip rate (0.3 weight), but gave slightly less weight to the closed mean slip rate per segment (0.2 weight) and the composite closed mean slip rate (0.3 weight). Reduced weight for the closed mean slip rates allowed for the inclusion of open-mean slip rate per segment (0.2 weight). We included the open mean rate for the BCS because it accounts for the long elapsed time since the BCS MRE (which is excluded in the closed mean rate). For the NS, we chose to use the open mean rate because the closed mean rate is based on only two closed recurrence intervals.

WS, SLCS, and PS	Weight
Closed mean slip rate per segment	0.35
Composite closed mean slip rate	0.35
Composite long-term slip rate	0.3

BCS and NS	Weight
Closed mean slip rate per segment	0.2
Open mean slip rate per segment	0.2
Composite closed mean slip rate	0.3
Composite long-term slip rate	0.3

The weighted mean slip rates are very similar for each segment ranging from 1.3 mm/yr for the BCS and SLCS (the shortest segments), to 1.5 and 1.6 mm/yr for the WS and PS, respectively (the longest segments) (Table B-12). The similarity in these rates reflects the fairly consistent closed-interval slip rates (1.3–2.0 mm/yr) and open-interval slip rates (1.2–2.1 mm/yr), as well as the composite rates, which are included in the weighted-mean calculation for each segment. The composite long-term slip rate is 1.0 mm/yr (0.6–1.4 mm/yr range) based on both measured displacements across Provo-phase and Bonneville highstand surfaces of the Bonneville lake cycle. The composite closed-interval slip rate is 1.7 mm/yr (0.9–2.7 mm/yr range) using the mean of the mean displacements per segment (~2.1 m) divided by the composite mean recurrence interval (1.2 ± 0.1 kyr).

RUPTURE MODELS

Evaluation of Possible Multi-Segment Ruptures on the Central WFZ

Prominent structural segment boundaries along the central WFZ represent persistent (long-term) features that may act as barriers to lateral propagation of surface faulting (Machette *et al.*, 1992). Support for the seismogenic independence of the segments stems from their unique late Holocene earthquake histories as well as significant differences in most recent earthquake timing across these complex structural boundaries (Schwartz and Coppersmith, 1985; Machette *et al*., 1992; Lund, 2005; DuRoss, 2008). However, similar to Machette *et al*., (1992), we cannot rule out the simultaneous rupture of adjacent segments (e.g., Chang and Smith, 2002) considering moderate to large uncertainties in earthquake timing and limited mid-Holocene earthquake records for the segments. Thus, we used the refined earthquake chronologies and displacement estimates per segment to identify possible and probable multi-segment ruptures on the central WFZ. These ruptures are included in rupture models that capture the range of possible earthquake rupture behavior on the central WFZ.

We evaluated possible multi-segment ruptures using: (1) the degree of overlap in the segment PDFs (PDF overlap; Figure B-9); (2) the number and location of sites where a specific rupture was identified, which defines the percentage of the rupture's length that has been studied and identifies along-strike gaps in paleoseismic data; and (3) the mean and along-strike displacements per rupture (from individual paleoseismic sites) (Table B-8). The PDF overlap is the sum of the minimum probabilities for time bins common to two PDFs (e.g., earthquake-timing PDFs for earthquakes on adjacent segments) and ranges from 0 (no overlap) to 1 (complete overlap of two identical PDFs) (after Biasi and Weldon, 2009; see also DuRoss *et al.*, 2011). Our evaluation relied mostly on the amount of PDF overlap (giving preference to PDFs with overlap values greater than an arbitrary amount of 0.5, which visually represents a moderate amount of overlap) and the displacement data rather than solely focusing on the locations of the paleoseismic sites along the ruptures because these are also a function of many other factors unrelated to the paleoseismology such as access, urbanization, or landowner restrictions. We considered ruptures at least as long as the largest known historic normal slip earthquake in the Basin and Range Province, the **M** 7.5 ± 0.3 1887 Sonora, Mexico earthquake that ruptured 102 km along three sections (Pitaycachi, Teras, and Otates sections) of a 300-km-long range-bounding normal fault in northern Mexico (Bakun, 2006; Suter, 2006) as plausible. On the central WFZ, two-segment ruptures yield rupture lengths of about 90 to 100 km (table B-13), consistent with the 1887 Sonora earthquake. However, we also considered ruptures as long as three adjacent segments if the paleoseismic data warranted it. Finally, we also made a qualitative assessment of the strength or persistence of a segment boundary based on its fault complexity and geometry (e.g., the horizontal distance between fault traces in a step-over zone), timing of most recent surface faulting, and the amount and quality of the paleoseismic data available at or adjacent to the boundary.

Based on our evaluation of earthquake timing data for the central WFZ, we found multi-segment ruptures between the BCS and WS, SLCS and PS, and PS and NS to be most probable. In particular, possible multi-segment ruptures B4+W5, S2+P3, and P3+N3 have significant overlap (~0.6) in their segment-PDF pairs, a large percentage (56–80%) of their total rupture lengths studied (having paleoseismic data), and minimal gaps between paleoseismic sites along the rupture (gaps less than 50% of the total rupture length) (Table B-13). Multi-segment rupture B3+W4 also has significant PDF overlap (0.7), but only 35% of the rupture length studied because no evidence is reported for W4 on the southern part of the WS (Kaysville site). However, because the Kaysville site may not have exposed evidence of all mid-Holocene earthquakes on the WS (DuRoss *et al.*, 2011), we consider B3+W4 a probable multi-segment rupture. Using these criteria, we consider multi-segment ruptures W2+S1, P2+N2, B2+W3, S3+P4, and S2+P3+N3 (the only three-segment rupture considered, which is based on similar PDF overlap values of 0.59 for S2–P3 and P3–N3) to be less likely. These ruptures have less overlap in their respective segment-PDF pairs (less than 0.4), more significant paleoseismic data gaps, and/or remaining questions regarding earthquake timing and rupture extent from the site data. In addition, we dismissed multi-segment ruptures involving poorly constrained earthquakes on a segment, such as N4 or P5.

We also evaluated possible multi-segment ruptures using estimates of mean displacement. To determine mean displacements for the multi-segment ruptures, we used analytical displacement curves fit to the per-site displacement data (discussed above in the Vertical Displacement per Rupture and Earthquake Source section), but using rupture lengths shown in Table B-13 and Figure B-10. On the BCS and WS, displacements are moderately large (~1.5–2.5 m) along the segments, and have large-displacement (4.2 m) peaks near the segment boundary, supporting multi-segment ruptures between the two segments (e.g., B2+W3 and B3+W4). Ruptures having moderately large displacements along two segments, but lacking a clear displacement peak near the possible rupture center (segment boundary) (e.g., 1.4–2.5 m along B4+W5, 1.5–3.2 m along W2+S1, and 1.4–2.5 m along S3+P4) provide less compelling evidence of multi-segment ruptures. Several segment pairs have more limited displacement data (~3 observations), but still show a half-ellipse-shaped displacement profile along the possible rupture length (*e.g.*, S2+P3 and S3+P4), providing a small degree of confidence in our possible multi-segment ruptures.

Mean displacement per multi-segment rupture (e.g., B2+W3), using our analytical displacement curves, is mostly about 2 m, but ranges from about 1.7 m (S2+P3+N3) to 3.8 m (P3+N3) (Figure B-10). These displacements are similar to those for single-segment ruptures (Table B-9) because we chose to honor the per-earthquake site displacements rather than model the displacement using a surface rupture length (SRL)–displacement scaling relation (e.g., Wells and Coppersmith, 1994; c.f., Biasi and Weldon, 2009). Doing so would result in larger displacements (e.g., 4–8 m for a 100-km-long rupture using the all- and normal-fault type maximum displacement–SRL regressions of Wells and Coppersmith, 1994) than generally observed (most per-earthquake displacements are < 3 m). Although our moderate multi-segment rupture displacements (similar to those for single-segment ruptures) may stem from sparse data along the rupture, it is also plausible that displacement values reach a maximum value once a certain rupture length (or possibly down-dip rupture width) is achieved (e.g., see Wesnousky, 2008).

Rupture Models for the Central WFZ

We developed rupture models for the central WFZ (Table B-14; Figures B-11 to B-13) using methods somewhat similar to those of the Working Group on California Earthquake Probabilities (WGCEP, 2003; Earthquake Probabilities in the San Francisco Bay Area) and WGCEP (2008; The Uniform California Earthquake Rupture Forecast [UCERF2]). WGCEP (2003) constructed rupture scenarios, which they defined as combinations of rupture sources that describe possible differing modes of failure of an entire fault (e.g., single- or multi-segment ruptures) in one earthquake cycle. These scenarios were combined into various fault-rupture models—ideally representing the long-term behavior of the fault—and the various scenarios were assigned weights based on the opinion of experts. A significant difference with our rupture models is that they are based on paleoseismic data that span the middle to late Holocene, and thus encompass the behavior of the central WFZ over multiple earthquake cycles. We only apply a single set of weights for these rupture models rather than various weights for the multiple fault-rupture models described in WGCEP (2003). Our rupture models yield different rupture-source combinations, similar to WGCEP (2003). For the UCERF2, WGCEP (2008) constructed B-priori models of fault rupture using paleoseismic data to determine single- and multi-segment earthquake rates and magnitudes (e.g., appendix F in WGCEP, 2008). Our rupture models are similar to WGCEP (2008) a-priori maximum, geologic-insight (preferred models that correspond with observations such as slip rate and paleoseismic event records), and minimum rupture models.

Rupture models address epistemic uncertainties in the segmentation of the central WFZ. Five models include: (1) a model in which each rupture is confined to a single-segment (single-segment rupture model; Figure B-11), (2) three intermediate models consisting primarily of single-segment ruptures, but including three combinations of multi-segment ruptures (intermediate models A, B, and C; Figure B-12), and (3) a model in which we include as many multi-segment ruptures as possible, which results in the fewest number of ruptures (multi-segment rupture model; Figure B-

13). These models were developed using the per-segment earthquake chronologies, rather than the individual trench-site data. We also included an unsegmented model, which accounts for potential multi-segment and/or partial-segment ruptures that we did not identify in these models (i.e., ruptures are allowed to "float" along the fault and are not constrained by segment boundaries).

Single-Segment Rupture Model

The single-segment rupture model includes 22 individual earthquakes on the central WFZ segments (Table B-6 and B-14; Figure B-11). Preference (model weight of 0.7) for the single-segment rupture model over those including multi-segment ruptures is based on (1) prominent along-strike variations in fault geometry (e.g., fault step-overs, gaps, and changes in strike), complexity (e.g., areas of diffuse faulting), and structure (e.g., range-front morphology and relief) that define prominent fault salients, hanging-wall basins, and fault segments; (2) differences in the timing of the youngest surface-faulting earthquakes at sites along the WFZ (e.g., compare the timing of the youngest events along the BCS, WS, SLCS, and PS; Figure B-3); (3) unique late Holocene surface-faulting earthquake histories per segment (Figure 4.1-2); (4) differences in per-event vertical displacement across the segment boundaries (e.g., compare DuRoss *et al*., 2011 to Personius *et al*., 2012, see also DuRoss, 2008); (5) long-term (latest Pleistocene) slip deficits at the segment boundaries (Machette *et al*., 1992); and (6) paleoseismic evidence for at least one spillover rupture from the WS to the BCS (DuRoss *et al*., 2012; Personius *et al*., 2012), rather than the simultaneous rupture of both segments. Per-earthquake displacements do not unequivocally support single-segment ruptures; however, we note that our single-segment analytical displacement curves better fit the displacement observations than the multi-segment curves (average error of 0.6 vs. 2.0 m, respectively). Single-segment earthquakes have median SRLs of 35 to 59 km and moment magnitudes of 6.9 to 7.3 based on SRL and 7.1 to 7.4 based on seismic moment (M_O) (see discussion in Calculating Magnitudes section).

We incorporated uncertainty into the location of each segment boundary (following WGCEP 2003; see discussion in Segment Boundary Uncertainties section) to allow for variability in single-segment rupture lengths. Although we cannot discount the occurrence of multi-segment ruptures, spillover rupture across segment boundaries (i.e., coseismic rupture across a "leaky" segment boundary; Crone and Haller, 1991) is more consistent with the WFZ paleoseismic data. For example, spillover rupture across the WS-BCS boundary in earthquake W2 shows that the segment boundary has failed in the late Holocene. However, the rupture only continued onto the southern ~8 km of the BCS (DuRoss *et al.*, 2012), despite the relatively large amount of accumulated seismic moment on the northern part of the BCS at the time of the event (Personius *et al.*, 2012). The 1983 Borah Peak earthquake demonstrated similar behavior, where surface faulting at the north end of the Thousand Springs segment crossed the segment boundary and ruptured about 8 km of the adjacent Warm Spring segment (Crone *et al.*, 1987). This treatment of the WFZ is consistent with the hybrid characteristic slip model of DuRoss (2008) in which "large-displacement single-segment ruptures dominate the fault history but are interrupted by anomalously small- and large-displacement events (i.e., possible partial- and multi-segment ruptures, respectively)."

Intermediate and Multi-Segment Rupture Models

The intermediate and multi-segment rupture models include combinations of both single-segment and multi-segment ruptures consistent with the central WFZ paleoseismic data (Tables B-14 and

B-15; Figures B-12 and B-13). In cases where several single-segment earthquakes could potentially combine to yield more than one multi-segment rupture, we relied on the PDF overlap value (as well as displacement data, if available) to guide our choice of a preferred rupture, or we included those combinations of ruptures in multiple models. For example, we preferred a rupture of S1+P2 (PDF overlap of 0.46) over S1+W2 (PDF overlap of 0.39). Likewise, we preferred B3+W4 over W4+S3 on the basis of the PDF overlap, but also because of the lack of evidence that W4 produced rupture on the southern part of the WS. Because of the similar PDF overlap values for the earthquake pairs of S2+P3 and P3+N3, we included both of these ruptures in separate models.

The intermediate rupture models each contain 19 to 20 earthquakes, most of which are single-segment ruptures, but two to three of which are the most probable multi-segment ruptures (Figure B-12). We have greater confidence in the intermediate models over the multi-segment rupture model because they include three multi-segment ruptures supported by similar earthquake times on adjacent segments (PDF overlap greater than 0.5), and for the BCS+WS, large (4.2-m) vertical displacements on the northern part of the WS (close to the BCS–WS segment boundary). We recognize that our three intermediate models represent only a few of all the possible models given the most probable ruptures shown in Table B-13.

We limited our intermediate models to three variations of the multi-segment ruptures we consider most probable: B4+W5, B3+W4, S2+P3, and P3+N3. Each of the intermediate models includes B4+W5 and B3+W4, which have very similar earthquake times (PDF overlap of about 0.6–0.7), large (4.2 m) displacements close to the BCS–WS segment boundary (at the northern end of the WS; Figure B-10), and a segment boundary that has failed in at least one spillover earthquake (continuation of WS earthquake W2 rupture about 8 km onto the southernmost BCS; DuRoss *et al.*, 2012; Personius *et al.*, 2012). Intermediate model C includes multi-segment ruptures B4+W5 and B3+W4; all of the remaining earthquakes are single-segment ruptures. Intermediate models A and B are identical to intermediate model C, but also include S2+P3 (model A) and P3+N3 (model B), which are supported by significant overlap (PDF overlap of 0.59) in their respective segment earthquake times (Table B-13). We prefer modeling S2, P3, and N3 as separate earthquakes and therefore prefer intermediate model C over models A and B, which include 85- to 99-km-long ruptures in S2+P3 and P3+N3. Given the broad timing uncertainties (± 0.5–0.7 kyr) for the individual earthquakes forming multi-segment ruptures in these models, we assign a total weight of 0.175 to the intermediate rupture models, with individual weights of 0.05, 0.05, and 0.075 to models A, B, and C, respectively.

The multi-segment rupture model includes 14 earthquakes—seven multi-segment and seven single-segment ruptures (Figure B-13), which is the fewest number of ruptures based on earthquake timing (PDF overlap). The model includes six two-segment ruptures and one three-segment rupture (S2+P3+N3) that we cannot fully dismiss given the earthquake-timing and displacement data. These multi-segment earthquakes have median SRLs of 88 to 128 km and moment magnitudes of 7.3 to 7.6 based on SRL and 7.4 to 7.5 based on M_O (see discussion in Calculating Magnitudes section).

Consistent with Machette *et al*. (1992), Lund (2005), and DuRoss (2008), we found no observational basis to conclude that earthquakes on the central WFZ regularly rupture multiple segments. That is, the most recent and best-constrained earthquakes per segment support individual-segment ruptures (figure B-3), at least one spillover rupture on the central WFZ has been documented with paleoseismic data (Personius *et al.*, 2012), and large numbers of multi-segment ruptures are inconsistent with the presence of prominent segment boundaries along the fault. Thus, we assigned relatively low weight to the multi-segment and intermediate rupture models (total weight of 0.2) compared to the single-segment rupture model (weight of 0.7). We gave more weight to the intermediate models (combined weight of 0.175) compared to the multi-segment rupture model (weight of 0.025) because they include the most probable multi-segment ruptures. Although some of the two (and three-) segment ruptures included in the multi-segment model may have occurred, we find it highly unlikely that all them occurred given the earthquake timing, segment-boundary, and spillover rupture arguments discussed above.

Together, the single-segment, intermediate, and multi-segment rupture models highlight possible modes of rupture along the central WFZ. However, our analyses are limited by modeling assumptions and poorly constrained mid-Holocene earthquake data. For example, although our analysis of the site PDF data by segment is consistent with the body of work indicating a segmented fault (e.g., Schwartz and Coppersmith, 1984; Machette *et al.*, 1992; Lund, 2005; DuRoss, 2008; Personius *et al.*, 2012) and serves to help limit the per-segment earthquake chronologies (e.g., DuRoss *et al.*, 2011), our ability to define and evaluate all possible rupture permutations is limited. We have addressed this limitation by constructing multi-segment and unsegmented rupture scenarios and by defining segment-boundary uncertainties, which allow for both partial-segment and spillover ruptures not specifically accounted for in the rupture models. However, we suggest that an evaluation of possible ruptures across the WFZ segment boundaries using the site earthquake data be conducted to yield a more comprehensive suite of rupture models (e.g., Biasi and Weldon, 2009). Finally, although the youngest earthquakes along the WFZ are consistent with a segmented fault, poorly constrained mid-Holocene earthquakes allow for longer rupture lengths. Additional mid- to early Holocene paleoseismic data for the central WFZ would aid in evaluating which of these multi-segment ruptures are most plausible.

Unsegmented Rupture Model

An unsegmented rupture model is implemented in the WGUEP forecast to account for ruptures on the central WFZ and the WFZ as a whole, irrespective of fault segmentation model and defined rupture boundaries. This model uses a distribution of magnitudes (as opposed to rupture lengths) ranging from **M** 6.75 to 7.6 (Section 3.4). To some degree, this model accounts for a level of partial-segment rupture and rupture across a segment boundary (spillover rupture) greater than that allowed by the segment boundary uncertainties. We assigned a relatively low weight (0.1) to the unsegmented model because the central WFZ is characterized by prominent segment boundaries and because the paleoseismic data suggests that ruptures on the central WFZ are not spatially random (e.g., the youngest earthquakes on the BCS are significantly older than those on the adjacent WS). Furthermore, we account for many multi-segment ruptures in our multi-segment and intermediate models, where those ruptures honor available paleoseismic earthquake timing and displacement data. Rates for the unsegmented model are based on the central WFZ closed-mean slip rate (~1.7 mm/yr; 0.2 weight), long-term slip rate (~1.0 mm/yr; 0.3 weight), as well as the broad range in slip rates for the northernmost end segments (Section 4.2.2).

Segment Boundary Uncertainties

To define segment-boundary uncertainties for the central WFZ (table B-16), we considered the geometry and extent of Holocene faulting near the ends of the segments, and, if available, paleoseismic data from sites close to the segment boundaries (Figures B-14 and B-15; Table B-17). Most segment boundaries are moderately well constrained (3–8 km); however, we include large uncertainties (13–17 km) for the complex overlapping fault step-over between the PS and NS. The best-constrained boundary is the BCS–Collinston segment (CS) boundary (± 3 km) based on the extent of Holocene surface faulting on the BCS, the apparent lack of Holocene rupture on the CS, and 3 km of spillover rupture from the BCS onto the southern CS (Personius, 1990; Personius *et al.*, 2012). We applied asymmetric uncertainties for several segment boundaries. The uncertainty for the BCS and WS is 3 to 8 km (depending on the segment; Figure B-14), which accounts for the spillover rupture that occurred during earthquake W2 (DuRoss *et al.*, 2012; Personius *et al.*, 2012). An asymmetric uncertainty for the PS and NS (+4, –13 km for the southern PS and +5, –17 km for the northern NS) is based on overlap between the two segment traces, the total length of the northern strand of the Nephi segment. Additional descriptions of geologic data used to constrain the segment-boundary uncertainties are included in Table B-17.

We used these uncertainties to define a range of rupture-lengths for both single- and multi-segment ruptures (Table B-16). For single-segment earthquake sources, rupture lengths range from a minimum of about 20 to 46 km to a maximum of 41 to 71 km. Ruptures equal to the minimum lengths would represent the partial rupture of each segment, or rupture of 47 to 82% of the median rupture lengths (e.g., 35 km for the BCS; Table B-16), defined using the traditional segmentation model (Machette *et al.*, 1992). Ruptures equal to the maximum lengths would entail rupture of about 117 to 133% of the median rupture lengths, and thus, spillover rupture of about 3 to 8 km at each end of the rupture. For the multi-segment ruptures, we used the same segment-boundary uncertainties, and defined minimum and maximum rupture lengths of 76–115 km and 100–141 km, respectively. These values result in the rupture percentages varying from 80–91% (using minimum lengths) to 110–114% (using maximum lengths) of the median multi-segment rupture lengths.

CONCLUSIONS

At least 22 surface-faulting earthquakes have ruptured the central segments of the WFZ since about 6.0 ka. These data stem from our systematic analysis of previous paleoseismic data, OxCal model development, and integration of site earthquake data along each segment. Using our revised surface-faulting earthquake histories for each segment, we calculated inter-event, open mean, and closed mean recurrence intervals. These data indicate moderately periodic earthquake recurrence on the central WFZ as a whole: inter-event recurrence intervals range from 0.7 to 2.7 kyr and yield a composite COV of ~0.5, and open and closed mean recurrence intervals for the segments (0.9–1.3 kyr and 1.1–1.5 kyr, respectively) are similar to a composite closed mean recurrence calculated for the central WFZ (~1.2 kyr). Using these recurrence data and modeled mean vertical displacements per rupture and segment, we calculated weighted mean vertical slip rates for the segments of ~1.3 to 1.6 mm/yr, based on closed-seismic-interval slip rates of ~1.3 to 2.0 mm/yr, open-interval rates of ~1.2 to 2.1 mm/yr, and composite rates for the central WFZ. A composite closed-interval slip rate, based on the mean central WFZ displacement of ~2.1 m divided by the 1.2-kyr composite recurrence, is ~1.7 mm/yr; a mean long-term slip rate for the central WFZ based on offset latest Pleistocene geomorphic surfaces is ~1.0 mm/yr.

Although single-segment ruptures may be the dominant earthquake process on the central WFZ, earthquake-timing uncertainties allow for alternative (e.g., multi-segment) scenarios. To address epistemic uncertainties in the WFZ segmentation, we constructed rupture models from the per-segment earthquake histories and also defined segment-boundary uncertainties. Five rupture models include both single- and multi-segment ruptures; an unsegmented model accounts for potential multi-segment and/or partial-segment (i.e., floating) ruptures not identified in our rupture models. Ultimately, prominent segment boundaries and significant differences in the timing of the most recent and best-constrained earthquakes per segment support the seismogenic independence of the segments. As we have no observational basis to conclude that earthquakes on the central WFZ regularly rupture multiple segments, we gave the greatest weight to rupture models dominated by single-segment earthquakes. Further, our segment-boundary uncertainties allow for more complex (e.g., partial and spillover) ruptures, and are consistent with paleoseismic observations. Our treatment of the central WFZ addresses uncertainties in fault segmentation and rupture extent, but is limited by our initial per-segment analysis. Thus, we suggest future work focused on the development of a comprehensive suite of possible ruptures from the individual per-site earthquake data.

REFERENCES

Aitken, M.J., 1994, Optical dating—a non-specialist review: Quaternary Geochronology (Quaternary Science Reviews), v. 13, p. 503–508.

Bakun, W.H., 2006, MMI attenuation and historical earthquakes in the Basin and Range Province of western North America: Bulletin of the Seismological Society of America, v. 96, no. 6, p. 2206–2220, doi: 10.1785/0120060045.

Biasi, G.P., and Weldon, R.J., 2006, Estimating surface rupture length and magnitude of paleoearthquakes from point measurements of rupture displacement: Bulletin of the Seismological Society of America, v. 96, no. 5, p. 1612–1623.

Biasi, G.P., and Weldon, R.J., 2009, San Andreas fault rupture scenarios from multiple paleoseismic records–stringing pearls: Bulletin of the Seismological Society of America, v. 99, no. 2A, p. 471–498, doi: 10.1785/0120080287.

Black, B.D., Hecker, S., Hylland, M.D., Christenson, G.E., and McDonald, G.N., 2003, Quaternary fault and fold database and map of Utah: Utah Geological Survey Map 193DM, scale 1:50,000, CD.

Black, B.D., Lund, W.R., Schwartz, D.P., Gill, H.E., and Mayes, B.H., 1996, Paleoseismic investigation on the Salt Lake City segment of the Wasatch fault zone at the South Fork Dry Creek and Dry Gulch sites, Salt Lake County, Utah – Paleoseismology of Utah, Volume 7: Utah Geological Survey Special Study 92, 22 p., 1 plate.

Bronk Ramsey, C., 1995, Radiocarbon calibration and analysis of stratigraphy—the OxCal program: Radiocarbon, v. 37, no. 2, p. 425–430.

Bronk Ramsey, C., 2001, Development of the radiocarbon program OxCal: Radiocarbon, v. 43, no. 2a, p. 355–363.

Bronk Ramsey, C., 2008, Depositional models for chronological records: Quaternary Science Reviews, v. 27, no. 1-2, p. 42–60.

Bruhn, R., Gibler, P., Houghton, W., and Parry, W., 1992, Structure of the Salt Lake segment, Wasatch normal fault zone—Implications for rupture propagation during normal faulting, *in* Gori, P.L., and Hays, W.W., editors, Assessment of regional earthquake hazards and risk along the Wasatch Front, Utah: U. S. Geological Survey Professional Paper 1500-B-J, p. H1–H25.

Chang, W.L., and Smith, R.B., 2002, Integrated seismic-hazard analysis of the Wasatch Front, Utah: Bulletin of the Seismological Society of America, v. 92, no. 5, p. 1904–1922.

Crone, A.J., and Haller, K.M., 1991, Segmentation and the coseismic behavior of Basin and Range normal faults—Examples from east-central Idaho and southwestern Montana, U.S.A.: Journal of Structural Geology, v. 13, no. 2, p. 151−164.

Crone, A.J., and Haller, K.M., 2004, Twenty years after the Borah Peak earthquake–Field guide to surface-faulting earthquakes along the Lost River fault, Idaho, *in* Haller, K.M., and Wood, S.H., editors, Geological field trips in southern Idaho, eastern Oregon, and northern Nevada: Department of Geosciences, Boise State University, Boise, Idaho, p. 116–133.

Crone, A.J., Machette, M.N, Bonilla, M.G., Lienkaemper, J.J., Pierce, K.L., Scott, W.E., and Bucknam, R.C., 1987, Surface faulting accompanying the Borah Peak earthquake and segmentation of the Lost River fault, central Idaho: Bulletin of the Seismological Society of America, v. 77, no. 3, p. 739−770.

Crone, A.J., Personius, S.F., DuRoss, C.B., Machette, M.N., and Mahan, S.A., 2014, History of late Holocene earthquakes at the Willow Creek site and on the Nephi segment, Wasatch fault zone, Utah—Paleoseismology of Utah, Volume 25: Utah Geological Survey Special Study 151, 43 p., CD.

Duller, G.A.T., 2008, Luminescence dating—Guidelines on using luminescence dating in archaeology: Swindon, United Kingdom, English Heritage Publishing, 45 p., online at http://www.aber.ac.uk/en/media/english_heritage_luminescence_dating.pdf, accessed March 2012.

DuRoss, C.B., 2008, Holocene vertical displacement on the central segments of the Wasatch fault zone, Utah: Bulletin of the Seismological Society of America, v. 98, no. 6, p. 2918–2933, doi: 10.1785/0120080119.

DuRoss, C.B., 2014, Paleoseismic investigation to determine the mid-Holocene chronology of surface-faulting earthquakes on the Nephi segment of the Wasatch fault zone, Utah and Juab Counties, Utah: Final Technical Report to the U.S. Geological Survey, National Earthquake Hazards Reduction Program, award no. G12AP20076, 48 p., 2 plates.

DuRoss, C.B., and Hylland, M.D., 2015, Synchronous ruptures along a major graben-forming fault system—Wasatch and West Valley fault zones, Utah, USA: Bulletin of the Seismological Society of America, v. 105, p. 14–37.

DuRoss, C.B., Hylland, M.D., McDonald, G.N., Crone, A.J., Personius, S.F., Gold, R.D., and Mahan, S.A., 2014, Holocene and latest Pleistocene paleoseismology of the Salt Lake City segment of the Wasatch fault zone at the Penrose Drive trench site, *in* DuRoss, C.B., and

Hylland, M.D., Evaluating surface faulting chronologies of graben-bounding faults in Salt Lake Valley, Utah—New paleoseismic data from the Salt Lake City segment of the Wasatch fault zone and the West Valley fault zone—Paleoseismology of Utah, Volume 24: Utah Geological Survey Special Study 149, 76 p., 12 appendices, CD.

DuRoss, C.B., McDonald, G.N., and Lund, W.R., 2008, Paleoseismic investigation of the northern strand of the Nephi segment of the Wasatch fault zone at Santaquin, Utah—Paleoseismology of Utah, Volume 17: Utah Geological Survey Special Study 124, 33 p., 1 plate, CD.

DuRoss, C.B., Personius, S.F., Crone, A.J., McDonald, G.N., and Briggs, R., 2012, Late Holocene earthquake history of the Brigham City segment of the Wasatch fault zone at the Hansen Canyon, Kotter Canyon, and Pearsons Canyon trench sites, Box Elder County, Utah—Paleoseismology of Utah, Volume 22: Utah Geological Survey Special Study 142, 28 p., 3 plates, 5 appendices.

DuRoss, C.B., Personius, S.F., Crone, A.J., McDonald, G.N., and Lidke, D.J., 2009, Paleoseismic investigation of the northern Weber segment of the Wasatch fault zone at the Rice Creek trench site, North Ogden, Utah—Paleoseismology of Utah, Volume 18: Utah Geological Survey Special Study 130, 37 p., 2 plates, CD.

DuRoss, C.B., Personius, S.F., Crone, A.J., Olig, S.S., Hylland, M.D., Lund, W.R., and Schwartz, D.P., 2016, Fault segmentation—New concepts from the Wasatch fault zone, Utah, USA: Journal of Geophysical Research – Solid Earth, v. 121, 27 p., doi: 10.1002/2015JB012519.

DuRoss, C.B., Personius, S.F., Crone, A.J., Olig, S.S., and Lund, W.R., 2011, Integration of paleoseismic data from multiple sites to develop an objective earthquake chronology—Application to the Weber segment of the Wasatch fault zone: Bulletin of the Seismological Society of America, v. 101, no. 6, p. 2765–2781, doi: 10.1785/0120110102.

Ellsworth, W.L., Matthews, M.V., Nadeau, R.M., Nishenko, S.P., Reasenberg, P.A., and Simpson, R.W., 1999, A physically-based earthquake recurrence model for estimation of long-term earthquake probabilities: U.S. Geological Survey Open-File Report 99-522, 22 p.

Friedrich, A.M., Wernicke, B.P., Niemi, N.A., Bennett, R.A., and Davis, J.L., 2003, Comparison of geodetic and geologic data from the Wasatch region, Utah, and implications for the spectral character of Earth deformation at periods of 10 to 10 million years: Journal of Geophysical Research, v. 108, no. B4, p. 2199, doi:10.1029/2001JB000682.

Forman, S.L., Machette, M.N., Jackson, M.E., and Maat, P., 1989, An evaluation of thermoluminescence dating of paleoearthquakes on the American Fork segment, Wasatch fault zone, Utah: Journal of Geophysical Research, v. 94, no. B2, p. 1622–1630.

Forman, S.L., Nelson, A.R., and McCalpin, J.P., 1991, Thermoluminescence dating of fault-scarp-derived colluvium—Deciphering the timing of earthquakes on the Weber segment of the Wasatch fault zone, north-central Utah: Journal of Geophysical Research, v. 96, no. B1, p. 595–605.

Godsey, H.S., Currey, D.R., and Chan, M.A., 2005, New evidence for an extended occupation of the Provo shoreline and implications for regional climate change, Pleistocene Lake

Bonneville, Utah, USA: Quaternary Research, v. 63, no. 2, p. 212–223, doi:10.1016/j.yqres.2005.01.002.

Godsey, H.S., Oviatt, C.G., Miller, D.M., and Chan, M.A., 2011, Stratigraphy and chronology of offshore to nearshore deposits associated with the Provo shoreline, Pleistocene Lake Bonneville, Utah: Palaeogeography, Palaeoclimatology, Palaeoecology, v. 310, no. 3–4, p. 442–450, doi: 10.1016/j.palaeo.2011.08.005.

Hanson, K.L., Swan, F.H., and Schwartz, D.P., 1981, Study of earthquake recurrence intervals on the Wasatch fault, Utah: San Francisco, California, Woodward-Clyde Consultants, sixth annual technical report prepared for U.S. Geological Survey under contract no. 14-08-0001-19115, 22 p., also available in Utah Geological Survey Miscellaneous Publication 13-3.

Hanson, K.L., Swan, F.H., and Schwartz, D.P., 1982a, Study of earthquake recurrence intervals on the Wasatch fault, Utah: San Francisco, California, Woodward-Clyde Consultants, seventh annual technical report prepared for U.S. Geological Survey under contract no. 14-08-0001-19842, 10 p., also available in Utah Geological Survey Miscellaneous Publication 13-3.

Hanson, K.L., Swan, F.H., and Schwartz, D.P., 1982b, Guidebook to late Pleistocene and Holocene faulting along the Wasatch Front and vicinity—Little Cottonwood Canyon to Scipio, Utah, *in* Hanson, K.L., and Schwartz, D.P., editors, Proceedings of the American Geophysical Union Chapman Conference on Fault Behavior and the Earthquake Generation Process, Snowbird, Utah, 40 p.

Harty, K.M., Mulvey, W.E., and Machette, M.N., 1997, Surficial geologic map of the Nephi segment of the WFZ, eastern Juab County, Utah: Utah Geological Survey Map 170, 14 p., 1 plate, scale 1:50,000.

Hemphill-Haley, M.A., and Weldon, R.J., 1999, Estimating prehistoric earthquake magnitude from point measurements of surface rupture: Bulletin of the Seismological Society of America, v. 89, no. 5, p. 1264–1279.

Horns, D.M., Rey, K.A., Barnes, C.S., Mcshinsky, R.D., and Palmer, M., 2009, New constraints on the timing of prehistoric earthquakes on the northernmost part of the Nephi segment of the Wasatch fault zone, Utah [abs.]: Geological Society of America Abstracts with Programs, v. 41, no. 6, p. 42.

Huntley, D.J., Godfrey-Smith, D.I., and Thewalt, M.L.W., 1985, Optical dating of sediments: Nature, v. 313, p. 105–107.

Hylland, M.D., 2007, Surficial-geologic reconnaissance and scarp profiling on the Collinston and Clarkston Mountain segments of the Wasatch fault zone, Box Elder County, Utah – Paleoseismic inferences, implications for adjacent segments, and issues for diffusion-equation scarp-age modeling—Paleoseismology of Utah, Volume 15: Utah Geological Survey Special Study 121, 18 p., CD.

Jackson, M., 1991, Number and timing of Holocene paleoseismic events on the Nephi and Levan segments, Wasatch fault zone, Utah—Paleoseismology of Utah, Volume 3: Utah Geological Survey Special Study 78, 23 p.

Lienkaemper, J.J., and Bronk Ramsey, C., 2009, OxCal – versatile tool for developing paleoearthquake chronologies—A primer: Seismological Research Letters, v. 80, no. 3, p. 431–434.

Lund, W.R., 2005, Consensus preferred recurrence-interval and vertical slip-rate estimates—Review of Utah paleoseismic-trenching data by the Utah Quaternary Fault Parameters Working Group: Utah Geological Survey Bulletin 134, 109 p., CD.

Lund, W.R., 2007, Summary—Utah Quaternary Fault Parameters Working Group Annual Meeting—Wednesday, February 28, 2007, Unpublished minutes of the Utah Quaternary Fault Parameters Working Group, 13 p., available online at http://geology.utah.gov/ghp/workgroups/pdf/uqfpwg/UQFPWG-2007_Summary.pdf.

Lund, W.R., and Black, B.D., 1998, Paleoseismic investigation at Rock Canyon, Provo segment, Wasatch fault zone, Utah County, Utah – Paleoseismology of Utah, Volume 8: Utah Geological Survey Special Study 93, 21 p.

Lund, W.R., Schwartz, D.P., Mulvey, W.E., Budding, K.E., and Black, B.D., 1991, Fault behavior and earthquake recurrence on the Provo segment of the Wasatch fault zone at Mapleton, Utah County, Utah – Paleoseismology of Utah, Volume 1: Utah Geological and Mineral Survey Special Study 75, 41 p.

Machette, M.N., 1992, Surficial geologic map of the Wasatch fault zone, eastern part of Utah Valley, Utah County and parts of Salt Lake and Juab Counties, Utah: U.S. Geological Survey Miscellaneous Investigations Series Map I-2095, scale 1:50,000, 30 p. pamphlet.

Machette, M.N., Crone, A.J., Personius, S.F., Mahan, S.A., Dart, R.L., Lidke, D.J., and Olig, S.S., 2007, Paleoseismology of the Nephi segment of the Wasatch fault zone, Juab County, Utah – Preliminary results from two large exploratory trenches at Willow Creek: U.S. Geological Survey Scientific Investigations Map SI-2966, 2 plates.

Machette, M.N., Personius, S.F., and Nelson, A.R., 1992, Paleoseismology of the Wasatch fault zone—A summary of recent investigations, interpretations, and conclusions, *in* Gori, P.L., and Hays, W.W., editors, Assessment of regional earthquake hazards and risk along the Wasatch Front, Utah: U.S. Geological Survey Professional Paper 1500-A, p. A1–A71.

McCalpin, J.P., 2002, Post-Bonneville paleoearthquake chronology of the Salt Lake City segment, Wasatch fault zone, from the 1999 "megatrench" site – Paleoseismology of Utah, Volume 10: Utah Geological Survey Miscellaneous Publication 02-7, 37 p.

McCalpin, J.P., and Forman, S.L., 2002, Post-Provo earthquake chronology of the Brigham City segment, Wasatch fault zone, Utah – Paleoseismology of Utah, Volume 11: Utah Geological Survey Miscellaneous Publication 02-9, 46 p.

McCalpin, J.P., Forman, S.L., and Lowe, M., 1994, Reevaluation of Holocene faulting at the Kaysville site, Weber segment of the Wasatch fault zone, Utah: Tectonics, v. 13, no. 1, p. 1-16.

Nelson, A.R., 1988, The northern part of the Weber segment of the Wasatch fault zone near Ogden, Utah, *in* Machette, M.N., editor, In the footsteps of G.K. Gilbert—Lake Bonneville and neotectonics of the eastern Basin and Range Province, Geological Society of America Guidebook for Field Trip Twelve, the Geological Society of America 100th Annual Meeting: Utah Geological and Mineral Survey Miscellaneous Publication 88-1, p. 33–37.

Nelson, A.R., Lowe, M., Personius, S., Bradley, L.A., Forman, S.L., Klauk, R., and Garr, J., 2006, Holocene earthquake history of the northern Weber segment of the Wasatch fault zone, Utah—Paleoseismology of Utah, Volume 13: Utah Geological Survey Miscellaneous Publication 05-8, 39 p., 2 plates.

Nelson, A.R., and Personius, S.F., 1993, Surficial geologic map of the Weber segment, Wasatch fault zone, Weber and Davis Counties, Utah: U.S. Geological Survey Miscellaneous Investigations Series Map I-2199, 22 p. pamphlet, scale 1:50,000.

Olig, S.S., McDonald, G.N., Black, B.D., DuRoss, C.B., Lund, W.R., Hylland, M.D., Simon, D.B., Giraud, R.E., and Christenson, G.E., 2011, Extending the paleoseismic record of the Provo segment of the Wasatch fault zone, Utah: URS Corporation, Final Technical Report to the U.S. Geological Survey, National Earthquake Hazards Reduction Program, Award No. 02HQGR0109, variously paginated.

Ostenaa, D., 1990, Late Holocene displacement history, Water Canyon site, Wasatch fault zone [abs.]: Geological Society of America Abstracts with Programs, v. 22, no. 6, p. 42.

Oviatt, C.G., 1997, Lake Bonneville fluctuations and global climate change: Geology, v. 25, p. 155–158.

Oviatt, C.G., Currey, D.R., and Sack, D., 1992, Radiocarbon chronology of Lake Bonneville, eastern Great Basin, USA: Paleogeography, Paleoclimatology, Paleoecology, v. 99, p. 225–241.

Personius, S.F., 1990, Surficial geologic map of the Brigham City segment and adjacent parts of the Weber and Collinston segments, Wasatch fault zone, Box Elder and Weber Counties, Utah: U.S. Geological Survey Miscellaneous Investigations Series Map I-1979, scale 1:50,000.

Personius, S.F., 1991a, Paleoseismic analysis of the Wasatch fault zone at the Brigham City trench site, Brigham City, Utah, *in* Personius, S.F., Paleoseismic analysis of the Wasatch fault zone at the Brigham City trench site, Brigham City and Pole Patch trench site, Pleasant View, Utah—Paleoseismology of Utah, Volume 2: Utah Geological and Mineral Survey Special Study 76, 39 p. 1–17.

Personius, S.F., 1991b, Paleoseismic analysis of the Wasatch fault zone at the Pole Patch trench site, Pleasant View, Utah, *in* Personius, S.F., Paleoseismic analysis of the Wasatch fault zone at the Brigham City trench site, Brigham City and Pole Patch trench site, Pleasant View, Utah—Paleoseismology of Utah, Volume 2: Utah Geological and Mineral Survey Special Study 76, p. 19–39.

Personius, S.F., DuRoss, C.B., and Crone, A.J., 2012, Holocene behavior of the Brigham City segment—Implications for forecasting the next large-magnitude earthquake on the Wasatch fault zone, Utah, USA: Bulletin of the Seismological Society of America, v. 102, no. 6, p. 2265–2281, doi: 10.1785/0120110214.

Personius, S.F., and Scott, W.E., 1992, Surficial geologic map of the Salt Lake City segment and parts of adjacent segments of the Wasatch fault zone, Davis, Salt Lake, and Utah Counties, Utah: U.S. Geological Survey Miscellaneous Investigations Series Map I-2106, scale 1:50,000.

Personius, S.F., and Scott, W.E., 2009 (digital release), Surficial geologic map of the Salt Lake City segment and parts of adjacent segments of the Wasatch fault zone, Davis, Salt Lake, and Utah Counties, Utah (digitized from U.S. Geological Survey Miscellaneous Investigations Series Map I-2106 [1992]): Utah Geological Survey Map 243DM, GIS data, scale 1:50,000.

Puseman, K., and Cummings, L.S., 2005, Separation and identification of charcoal and organics from bulk sediment samples for improved radiocarbon dating and stratigraphic correlations, *in* Lund, W.R., editor, Western States Seismic Policy Council Proceedings Volume of the Basin and Range Province Seismic Hazards Summit II: Utah Geological Survey Miscellaneous Publication 05-2, 10 p., CD.

Robison, R.M., and Burr, T.N., 1991, Fault-rupture hazard analysis using trenching and borings—Warm Springs fault, Salt Lake City, Utah, *in* McCalpin, J.P., editor, Proceedings of the 27th Symposium on Engineering Geology and Geotechnical Engineering: Boise, Idaho Department of Transportation, p. 26-1–26-13.

Schwartz, D.P., and Coppersmith, K.J., 1984, Fault behavior and characteristic earthquakes—Examples from the Wasatch and San Andreas fault zones: Journal of Geophysical Research, v. 89, p. 5681–5698.

Schwartz, D.P., Hanson, K.L., and Swan, F.H., III, 1983, Paleoseismic investigations along the Wasatch fault zone – An update, *in* Gurgel, D.K., editor, Geologic Excursions in Neotectonics and Engineering Geology in Utah, Geological Society of America Rocky Mountain and Cordilleran Sections Meeting, Salt Lake City, Utah, Field Trip Guidebook – Part IV: Utah Geological and Mineral Survey Special Studies 62, p. 45–48.

Schwartz, D.P., and Lund, W.R., 1988, Paleoseismicity and earthquake recurrence at Little Cottonwood Canyon, WFZ, Utah, *in* Machette, M.N., editor, In the footsteps of G.K. Gilbert—Lake Bonneville and neotectonics of the eastern Basin and Range Province: Utah Geological and Mineral Survey Miscellaneous Publication 88-1, p. 82–85.

Simon-Bymaster, Inc., 1999, Report of geologic investigation; Salt Palace Convention Center Expansion Project; 100 South West Temple Street, Salt Lake City: Unpublished consultant report prepared for Salt Lake County, 27 p.

Scott, W.E., and Shroba, R.R., 1985, Surficial geologic map of an area along the Wasatch fault zone in the Salt Lake Valley, Utah: U.S. Geological Survey Open-File Report 85-448, 18 p, 2 plates, scale 1:24,000.

Suter, M., 2006, Contemporary studies of the 3 May 1887 M_W 7.5 Sonora, Mexico (Basin and Range Province) earthquake: Seismological Research Letters, v. 77, no. 2, p. 134–147.

Swan, F.H., III, Schwartz, D.P., and Cluff, L.S., 1980, Recurrence of moderate to large magnitude earthquakes produced by surface faulting on the Wasatch fault zone, Utah: Bulletin of the Seismological Society of America, v. 70, p. 1431–1462.

Swan, F.H., III, Schwartz, D.P., Hanson, K.L., Knuepfer, P.L., and Cluff, L.S., 1981, Study of earthquake recurrence intervals on the Wasatch fault at the Kaysville site, Utah: U.S. Geological Survey Open-File Report 81-228, 30 p.

Tucker, A.B., Woefti, W., Bonani, G., Suter, M., 1983, Earthquake dating—An application of carbon-14 atom counting: Science, v. 219, p. 1320–1321.

Wells, D.L., and Coppersmith, K.J., 1994, New empirical relationships among magnitude, rupture length, rupture width, rupture area, and surface displacement: Bulletin of the Seismological Society of America, v. 84, no. 4, p. 974–1002.

Wesnousky, S.G., 2008, Displacement and geometrical characteristics of earthquake surface ruptures—Issues and implications for seismic-hazard analysis and the process of earthquake rupture: Bulletin of the Seismological Society of America, v. 98, no. 4, p. 1609–1632, doi: 10.1785/0120070111.

Wheeler, R.L., and Krystinik, K.B., 1992, Persistent and nonpersistent segmentation of the Wasatch fault zone, Utah—Statistical analysis for evaluation of seismic hazard, *in* Gori, P.L., and Hays, W.W., editors, Assessment of regional earthquake hazards and risk along the Wasatch front, Utah: U.S. Geological Survey Professional Paper 1500, p. B1–B47.

Working Group on California Earthquake Probabilities, 2003, Earthquake probabilities in the San Francisco Bay region 2002–2031: U.S. Geological Survey Open-File Report 03-214, variously paginated.

Working Group on California Earthquake Probabilities, 2008, The Uniform California Earthquake Rupture Forecast: U.S. Geological Survey Open File Report 2007-1437, 96 p., 16 appendices.

Table B-1. Correlation of surface-faulting earthquakes on the Brigham City segment.

Brigham City Segment	Kotter Canyon	Bowden Canyon	Box Elder Canyon	Pearsons Canyon
no evidence	*no evidence*	*no evidence*	*no evidence*	PC1 1.2 ± 0.05
B1 2.4 ± 0.3	KC1 2.5 ± 0.3	BC1 2.6 ± 1.0	BEC1 2.2 ± 0.6	*not exposed*
B2 3.5 ± 0.2	KC2 3.5 ± 0.3	BC2 3.7 ± 0.5	BEC2 3.2 ± 0.5	-
B3 4.5 ± 0.5	*not exposed*	BC3 4.6 ± 0.6	BEC3 4.4 ± 1.1	-
B4 5.6 ± 0.7	-	BC4 5.8 ± 1.6	BEC4 5.6 ± 0.8	-

Earthquake times are mean ± two sigma (2σ) in thousands of calendar years B.P. (1950) (ka) based on OxCal modeling. BCS earthquakes B1–B4 are based on the correlation of site data; for example, KC1, BC1, and BEC1 correlate and are used to define earthquake B1 (see DuRoss *et al.*, 2011 for methodology). PC1, which is likely the northern continuation of WS earthquake W2, did not rupture the northern BCS.

Table B-2. Correlation of surface-faulting earthquakes on the Weber segment.

Weber Segment	Rice Creek	Garner Canyon	East Ogden	Kaysville
W1 0.6 ± 0.07	RC1 0.6 ± 0.08	GC1 0.6 ± 0.07	EO1 0.5 ± 0.2	K1 0.6 ± 0.2
W2 1.1 ± 0.6	RC2 1.2 ± 0.3	GC2 1.5 ± 0.5	EO2 0.9 ± 0.4	K2 0.9 ± 0.5
W3 3.1 ± 0.3	RC3 3.4 ± 0.7	GC3 3.2 ± 0.6	EO3 3.0 ± 0.4	K3 2.8 ± 1.7
W4 4.5 ± 0.3	RC4 4.6 ± 0.5	GC4 4.4 ± 0.6	EO4 4.0 ± 0.9	*no evidence*
W5 5.9 ± 0.5	RC5 6.0 ± 1.0	*not exposed*	*not exposed*	K4 5.7 ± 1.3

Earthquake times are mean ± two sigma (2σ) in thousands of calendar years B.P. (1950) (ka) based on OxCal modeling. WS earthquakes W1–W5 are based on the correlation of site data; for example, RC1, GC1, EO1, and K1 correlate and are used to define earthquake W1 (see DuRoss *et al.*, 2011 for methodology).

Table B-3. Correlation of surface-faulting earthquakes on the Salt Lake City segment**.**

Salt Lake City Segment	***Penrose Drive***	**Little Cottonwood Canyon**	**South Fork Dry Creek**
S1 1.3 ± 0.2	*no evidence*	LCC1 1.3 ± 0.04	SFDC1 1.3 ± 0.2
S2 2.2 ± 0.2	*no evidence*	LCC2 2.1 ± 0.3	SFDC2 2.2 ± 0.4
S3 4.2 ± 0.3	*PD1 4.0 ± 0.5*	LCC3 4.4 ± 0.5	SFDC3 3.8 ± 0.6
S4 5.3 ± 0.2	*PD2 5.9 ± 0.7*	LCC4 5.5 ± 0.8	SFDC4 5.0 ± 0.5

Earthquake times are mean ± two sigma (2σ) in thousands of calendar years B.P. (1950) (ka) based on OxCal modeling. SLCS earthquakes S1–S4 are based on the correlation of site data; for example, LCC1 and SFDC1 correlate and are used to define earthquake S1 (see DuRoss *et al.*, 2011 for methodology). Penrose Drive data, shown in *italics* (DuRoss *et al.*, 2014; DuRoss and Hylland, 2015), were not used to define the times of earthquakes S3 and S4, but are shown for comparative purposes. Including PD1 would result in an S3 time of 4.2 ± 0.2 ka; including PD2 would have an insignificant (<50-yr) effect on the S4 time.

Table B-4. Correlation of surface-faulting earthquakes on the Provo segment.

Provo Segment	**American Fork**	**Rock Canyon**	**Mapleton North**	**Mapleton South**
P1 0.6 ± 0.05	AF1 0.4 ± 0.2	ROC1 0.6 ± 0.07	MN1 0.6 ± 0.07	MS1 0.7 ± 0.7
P2 1.5 ± 0.4	*not dated or exposed?*	*not exposed?*	MN2 1.5 ± 0.4	*not exposed?*
P3 2.2 ± 0.4	AF2 2.0 ± 0.8	*not exposed*	MN3 3.2 ± 1.6	MS2 2.2 ± 0.8
P4 4.7 ± 0.3	AF3 4.3 ± 1.5	-	MN4 4.7 ± 0.3	*not exposed*
P5 5.9 ± 1.0	AF4 6.2 ± 1.0	-	MN5 5.6 ± 0.5	-

Earthquake times are mean ± two sigma (2σ) in thousands of calendar years B.P. (1950) (ka) based on OxCal modeling. PS earthquakes P1–P5 are based on the correlation of site data; for example, AF1, ROC1, MN1, and MS1 correlate and are used to define earthquake P1 (see DuRoss *et al.*, 2011 for methodology). Possible reasons as to why MN2 was not identified at other sites are discussed in the text, as well as uncertainties in correlating AF2 with MN3 and MS2 (versus the alternative of correlating AF2 with MN2 and MS2).

Table B-5. Correlation of surface-faulting earthquakes on the Nephi segment.

Nephi Segment		Santaquin Canyon		North Creek		Willow Creek		Red Canyon	
N1	0.2 ± 0.09	SQ1	0.3 ± 0.2*	NC1	0.4 ± 0.5	WC1	0.2 ± 0.09	REC1	0.5 ± 0.5
N2	1.2 ± 0.1	*no evidence*		NC2	1.4 ± 0.3	WC2	1.2 ± 0.1	REC2	1.2 ± 0.3
N3	2.0 ± 0.4	*no evidence/not exposed?*		NC3	1.9 ± 0.5	WC3	2.0 ± 0.5	*no evidence*	
N4	4.7 ± 1.8	*no evidence/not exposed?*		*not exposed?*		WC4	4.7 ± 1.8	REC3	4.7 ± 2.5*

Earthquake times are mean ± two sigma (2σ) in thousands of calendar years B.P. (1950) (ka) based on OxCal modeling. NS earthquakes N1–N4 are based on the correlation of site-data; for example, NC1, WC1, and REC1 correlate and are used to define earthquake N1 (see DuRoss *et al.*, 2011 for methodology). * Indicates earthquakes that are not used to define a segment earthquake on account of uncertainty in the site correlation (SQ1) or a very broadly defined earthquake time (REC3).

Table B-6. Summary of earthquake timing data for the central WFZ.

Rupture[1]	**PDFs combined**[2]		**Earthquake Timing**[3] (ka)		**Inter-event recurrence**[4] (kyr)
	Site PDFs	Integration method	Mean ± 2σ	5th–50th–95th [mode]	
B1	BEC1, BC1, KC1	product	2.4 ± 0.3	2.2–2.4–2.6 [2.4]	-
B2	BEC2, BC2, KC2	product	3.5 ± 0.2	3.4–3.5–3.7 [3.4]	1.1 ± 0.3 (B2–B1)
B3	BEC3, BC3	product	4.5 ± 0.5	4.1–4.5–5.0 [4.5]	1.0 ± 0.6 (B3–B2)
B4	BEC4, BC4	product	5.6 ± 0.6	5.0–5.6–6.1 [5.6]	1.1 ± 0.8 (B4–B3)
W1	RC1, K1, EO1, GC1	product	0.6 ± 0.1	0.5–0.6–0.6 [0.5]	-
W2	RC2, K2, EO2, GC2	mean	1.1 ± 0.6	0.7–1.2–1.7 [1.3]	0.7 ± 0.6 (W2–W1)
W3	RC3, K3, EO3, GC3	product	3.1 ± 0.3	2.9–3.1–3.3 [3.1]	1.9 ± 0.7 (W3–W2)
W4	RC4, EO4, GC4	product	4.5 ± 0.3	4.2–4.5–4.7 [4.5]	1.4 ± 0.4 (W4–W3)
W5	RC5, K4	product	5.9 ± 0.5	5.6–5.9–6.4 [5.6]	1.4 ± 0.6 (W5–W4)
S1	LCC1, SFDC1	mean	1.3 ± 0.2	1.2–1.3–1.5 [1.3]	-
S2	LCC2, SFDC2	product	2.2 ± 0.2	2.0–2.2–2.3 [2.2]	0.8 ± 0.3 (S2–S1)
S3	LCC3, SFDC3	product	4.1 ± 0.3	3.9–4.1–4.4 [4.1]	2.0 ± 0.4 (S3–S2)
S4	LCC4, SFDC4	product	5.3 ± 0.2	5.1–5.2–5.5 [5.2]	1.1 ± 0.4 (S4–S3)
P1	MN1, AF1, ROC1, MS1	product	0.6 ± 0.05	0.5–0.6–0.6 [0.6]	-
P2	MN2	-	1.5 ± 0.4	1.2–1.5–1.8 [1.7]	0.9 ± 0.4 (P2–P1)
P3	MN3, AF2, MS2	product	2.2 ± 0.4	1.9–2.3–2.6 [2.3]	0.8 ± 0.5 (P3–P2)
P4	MN4, AF3	product	4.7 ± 0.3	4.5–4.7–4.9 [4.7]	2.5 ± 0.5 (P4–P3)
P5	MN5, AF4	mean	5.9 ± 1.0	5.2–5.8–6.9 [5.6]	1.2 ± 1.0 (P5–P4)
N1	NC1, WC1, REC1	product	0.2 ± 0.1	0.1–0.2–0.3 [0.2]	-
N2	NC2, WC2, REC2	product	1.2 ± 0.1	1.2–1.2–1.3 [1.2]	1.0 ± 0.1 (N2–N1)
N3	NC3, WC3	product	2.0 ± 0.4	1.7–2.0–2.3 [2.0]	0.8 ± 0.4 (N3–N2)
N4	WC4	-	4.7 ± 1.8	3.3–4.7–6.1 [5.8]	2.7 ± 1.8 (N4–N3)

[1] Rupture abbreviations: B – Brigham City segment, W – Weber segment, S – Salt Lake City segment, P – Provo segment, N – Nephi segment. Numerical values indicate youngest (e.g., B1) and progressively older earthquakes (e.g., B2–B4) (Tables B-1 to B-5).

[2] Site PDFs contributing to the segment-wide rupture times; e.g., BEC1, BC1, and KC1 were combined to determine the time of rupture B1. Integration method is the product or mean of the site PDF probabilities (over common time bins); see text and DuRoss *et al.* (2011) for discussion.

[3] Summary statistics based on integration of per-site earthquake-timing PDFs (derived from OxCal models) following the method of DuRoss *et al.* (2011). Earthquake times are in thousands of years before 1950.

[4] Individual recurrence interval (RI) is mean recurrence time between earthquakes (e.g., B4–B3 time).

Table B-7. Mean recurrence intervals for the central WFZ.

Segment	**Closed mean RI**[1] (kyr)	**Open mean RI (*N*-in-*T*)**[2] (kyr)	**Time since MRE**[3] (kyr)
BCS	1.1 ± 0.2 (B4–B1)	1.5 ± 0.1; 4 events <5.9 ± 0.4 ka [BEC4]	2.5 ± 0.3
WS	1.3 ± 0.1 (W5–W1)	1.4 ± 0.3; 5 events <7.1 ± 1.4 ka [RC5]	0.6 ± 0.07
SLCS	1.3 ± 0.1 (S4–S1)	1.3 ± 0.09; 4 events <5.2 ± 0.4 ka [SFDC4]	1.4 ± 0.2
PS	1.3 ± 0.2 (P5–P1)	1.2 ± 0.03; 5 events <6.1 ± 0.2 ka [MN5]	0.6 ± 0.05
NS	0.9 ± 0.2 (N3–N1)	1.1 ± 0.04; 3 events <3.2 ± 0.1 ka [WC3]	0.3 ± 0.09

[1] Closed mean recurrence per segment is elapsed time between oldest and youngest earthquakes per segment (e.g., B4–B1; Tables B-1 to B-5) divided by the number of closed intervals.

[2] Open mean recurrence per segment is the time from the maximum constraining age on the oldest event (e.g., 5.9 ± 0.4 ka for B4) to the present (2011) divided by number of events.

[3] Time (to the present; 2011) since the most recent earthquake (MRE).

Table B-8. Vertical displacement per site and rupture for the central WFZ.

Rupture[1]	**Site earthquake**[1] [**distance along rupture** (km)][2]	**Site Displacement**[3] (m)			**Rupture Displacement**[5] (m)			
		Mean	Range	Type[4]	Mean	Min	Max	n
Single-segment ruptures								
B1	BE1[a] [17.1]	>0.9	0.4	TD				
B1	KC1 [13.4]	2.1	0.2	TD				
B1					**2.1**	**1.9**	**2.3**	1
B2	BEC2[a] [17.1]	>1.0	0.0	TD				
B2	BC2 [14.9]	1.0	0.0	TD				
B2	KC2 [13.4]	2.1	0.2	TD				
B2					**1.6**	**1.5**	**1.7**	2
B3	BC3 [14.9]	2.5	0.0	TD				
B3	PP1 [34.6]	1.0	0.3	TD				
B3					**1.8**	**1.6**	**1.9**	2
B4	BEC4[a] [17.1]	>1.1	0.2	TD				
B4	BC4 [14.9]	2.5	0.0	TD				
B4					**2.5**	**-**	**-**	1
W1	RC1 [2.7]	2.0	0.7	SD				
W1	K1 [36.1]	1.8	0.1	TD				
W1	EO1 [11.8]	0.7	0.2	TD				
W1	GC1 [6.5]	1.2	0.2	TD				
W1					**1.4**	**1.1**	**1.7**	4
W2	PC1[b] [3.7]	0.5	0.4	TD				
W2	RC2 [11.8]	3.2	0.5	TD				
W2	EO2 [20.8]	2.6	0.0	TD				
W2	GC2 [15.5]	1.5	0.7	TD				
W2					**2.0**	**1.6**	**2.4**	4
W3	RC3 [2.7]	1.1	0.3	TD				
W3	K3 [36.1]	2.9	0.6	TD				
W3	EO3 [11.8]	4.2	0.0	TD				
W3	GC3 [6.5]	1.0	0.1	TD				
W3					**2.3**	**2.1**	**2.6**	4
W4	RC4 [2.7]	2.0	0.4	TD				
W4	EO4 [11.8]	4.2	0.0	TD				
W4					**3.1**	**2.9**	**3.3**	2
W5	RC5 [2.7]	2.0	0.4	CWT				
W5	K4 [36.1]	1.4	0.0	TD				
W5					**1.7**	**1.5**	**1.9**	2
S1	LLC1 [30.8]	1.8	0.0	TR				
S1	SFDC1 [34.1]	2.0	0.5	TD				
S1					**1.9**	**1.7**	**2.2**	2
S2	LCC2 [30.8]	1.8	0.0	TR				
S2	SFDC2 [34.1]	2.0	0.5	TD				

S2					**1.9**	**1.7**	**2.2**	2
S3	LCC3 [30.8]	1.8	0.0	TR				
S3	PD1 [9.4]	1.4	0.4	CWT, TD				
S3					**1.6**	**1.4**	**1.8**	2
S4	LCC4 [30.8]	1.8	0.0	TR				
S4	PD2 [9.4]	1.0	0.3	CWT, TD				
S4					**1.4**	**1.3**	**1.6**	2
P1	MN1 [46.0]	4.7	0.5	TD				
P1	AF1 [8.7]	2.5	0.3	TD				
P1	ROC1 [28.1]	3.3	0.0	SD				
P1					**3.5**	**3.2**	**3.8**	3
P2	MN2 [46.0]	1.4	0.9	TD[a]	**1.4**	**0.5**	**2.3**	1
P3	AF2 [8.7]	2.5	0.3	TD	**2.5**	**2.2**	**2.8**	1
P4	AF3 [8.7]	2.5	0.3	TD	**2.5**	**2.2**	**2.8**	1
P5	no data							
N1	NC1 [26.1]	2.1	0.1	CWT				
N1	REC1 [39.0]	1.4	0.3	CWT				
N1					**1.8**	**1.6**	**2.4**	2-3
N2	NC2 [26.1]	2.3	0.3	TD				
N2	REC2 [39.0]	1.5	0.2	CWT				
N2					**1.9**	**1.7**	**2.2**	2
N3	no data							
N4	REC3 [39.0]	1.7	0.4	CWT	**1.7**	**1.4**	**2.0**	1
-	SQ1[c]	3.0	0.2	SD				

Multi-segment ruptures

Rupture[1]	**Site earthquakes**[1] [**distance along rupture** (km)][2]	**Rupture displacement**[5] (m)			
		Mean	Min	Max	n
B2+W3	KC2 [13.3], BC2 [14.9], RC3 [37.7], GC3 [41.4], EO3 [46.7], K3 [71.0]	**2.1**	**1.9**	**2.3**	6
B3+W4	BC3 [14.9], PP1 [34.8], RC4 [37.7], EO4 [46.7]	**2.4**	**2.3**	**2.6**	4
B4+W5	BC4 [14.9], RC5 [37.7], K4 [71.0]	**2.0**	**1.8**	**2.1**	3
W2+S1	PC1 [3.7], RC2 [11.5], GC2 [15.3], EO2 [20.6], LLC1 [94.6], SFDC1 [97.9]	**1.9**	**1.6**	**2.3**	6
S2+P3+N3	LLC2 [30.2], SFDC2 [33.6], AF2 [47.7]	**2.1**	**1.9**	**2.3**	3
S3+P4	PD1 [9.4], LLC3 [30.1], AF3 [48.6]	**1.9**	**1.7**	**2.1**	3
P2+N2	MN2 [42.8], NC2 [71.0], REC2 [83.8]	**1.7**	**1.3**	**2.2**	3
P3+N3	AF2 [7.7]	**2.5**	**2.2**	**2.8**	1
S2+P3	LLC2 [30.1], SFDC2 [34.2], AF2 [48.6]	**2.1**	**1.8**	**2.4**	3

[1] Individual site earthquakes (e.g., KC1) that correspond to single or multi-segment ruptures.

[2] Distance along rupture is site location along linear rupture length (end-to-end), measured from the northern end. For example, the displacement in site earthquake KC1 occurred 13.4 km south of the northern end of the BCS B1 rupture. Distance measurements are used to construct along-strike displacement profiles for analytical displacement modeling (Figure B-8; Table B-9); see text for discussion.

[3] Displacement per site earthquake (e.g., KC1) based on individual trench data (see text for discussion of site paleoseismic data; also DuRoss [2008]). [a] Displacement not used (minimum estimate); [b] PC1 displacement is likely for W2 (DuRoss *et al.*, 2012; Personius *et al.*, 2012)–displacement not used; [c] displacement for SQ1 is not used to constrain N1 due to uncertainty in whether SQ1 corresponds with southern-NS N1 or PS P1.

[4] Displacement-measurement types include TD - total displacement (or surface offset) at site apportioned to individual events, either equally or based on colluvial wedge thickness (CWT) or a trench reconstruction. CWT indicates per-event displacement based on maximum thickness of scarp colluvium, min-max range is generally maximum thickness to two-times that thickness. SD is stratigraphic displacement. [a] Displacement for P2 (MN2) is based on an eroded buried free-face height minus back tilting and antithetic faulting.

[5] Rupture displacement based on simple mean of site displacements corresponding to the rupture (e.g., mean of BC2 and KC2 displacements for rupture B2). n is number of site displacement observations.

Table B-9. Modeled vertical displacement per rupture for the central WFZ.

Rupture	Modeled Displacement Profiles (ellipses)[1]									
	Mean[2]	Error	n, h	Min[2]	Error	n, h	Max[2]	Error	n, h	Notes
B1	**1.7**	1.0E-03	0.5, 2.2	**1.5**	7.0E-04	0.5, 2.0	**1.8**	1.0E-03	0.5, 2.4	fixed-shape
B2	**1.2**	6.0E-01	0.5, 1.6	**1.2**	4.0E-01	0.5, 1.5	**1.3**	9.0E-01	0.5, 1.7	fixed-shape
B3	**2.0**	7.0E-03	0.4, 2.5	**1.8**	3.0E-03	0.6, 2.5	**2.1**	2.0E-03	0.3, 2.5	best-fit
B4	**2.0**	1.0E-03	0.5, 2.5	**1.5**	*(average of B1-B3)*[a]		**2.1**	*(max of B1-B3)*[a]		fixed-shape (mean)
W1	**1.4**	1.2E+00	0.1, 1.5	**1.1**	8.0E-01	0.1, 1.2	**1.7**	2.2E+00	0.1, 1.8	best-fit
W2	**2.1**	2.4E+00	0.7, 3.0	**1.8**	2.9E+00	0.9, 2.7	**2.5**	2.3E+00	0.5, 3.3	best-fit
W3	**2.7**	3.4E+00	0.7, 3.9	**2.4**	4.5E+00	0.6, 3.3	**3.0**	2.6E+00	0.7, 4.3	best-fit
W4[b]	**4.0**	4.0E-01	0.5, 5.3	**3.8**	6.0E-01	0.5, 5.1	**4.1**	5.0E-01	0.5, 5.5	best-fit/fixed-shape
W5	**1.7**	4.0E-01	0.1, 1.8	**1.5**	1.0E-01	0.1, 1.6	**1.9**	9.0E-01	0.1, 2.0	best-fit
S1[c]	**1.9**	2.0E-01	0.5, 2.5	**1.7**	1.0E-02	0.5, 2.2	**2.2**	6.0E-01	0.5, 2.8	fixed-shape
S2	**1.9**	2.0E-01	0.5, 2.5	**1.7**	1.0E-02	0.5, 2.2	**2.2**	6.0E-01	0.5, 2.8	fixed-shape
S3[c]	**1.5**	8.0E-02	0.3, 1.8	**1.3**	3.0E-01	0.2, 1.5	**1.7**	1.0E-04	0.5, 2.2	best-fit
S4	**1.3**	3.0E-01	0.2, 1.5	**1.2**	6.0E-01	0.1, 1.3	**1.5**	1.0E-01	0.1, 1.6	best-fit
P1	**3.3**	2.2E+00	0.2, 3.8	**3.1**	1.6E+00	0.3, 3.7	**3.6**	3.2E+00	0.1, 3.9	best-fit
P2[d]	**1.3**	7.0E-04	0.5, 1.7	**1.3**	7.0E-04	0.5, 1.7	**1.3**	7.0E-04	0.5, 1.7	fixed-shape
P3	**2.9**	7.0E-04	0.5, 3.8	**2.6**	5.0E-05	0.5, 3.4	**3.3**	2.0E-04	0.5, 4.3	fixed-shape
P4	**2.9**	7.0E-04	0.5, 3.8	**2.6**	5.0E-05	0.5, 3.4	**3.3**	2.0E-04	0.5, 4.3	fixed-shape
P5	**2.6**	*(average of P1-P4)*[a]		**2.4**	*(average of P1-P4)*[a]		**2.9**	*(average of P1-P4)*[a]		average
N1[e]	**1.8**	4.0E-03	0.4, 2.2	**1.5**	3.0E-03	0.5, 2.0	**2.3**	8.0E-01	0.3, 2.7	best-fit
N2	**1.9**	3.0E-03	0.4, 2.4	**1.7**	3.0E-03	0.4, 2.1	**2.1**	2.0E-03	0.4, 2.7	best-fit
N3	**2.0**	*(average of N1,N2,N4)*[a]		**1.7**	*(average of N1,N2,N4)*[a]		**2.4**	*(average of N1,N2,N4)*[a]		average
N4	**2.4**	6.0E-04	0.5, 3.2	**2.0**	2.0E-04	0.5, 3.6	**2.7**	2.0E-02	0.5, 3.4	fixed-shape
B2+W3	**1.9**	8.3E+00	0.2, 2.2	**1.7**	8.2E+00	0.3, 2.0	**2.1**	8.2E+00	0.2, 2.4	best-fit
B3+W4	**2.3**	5.4E+00	0.1, 2.5	**2.2**	6.7E+00	0.1, 2.3	**2.4**	4.2E+00	0.2, 2.7	best-fit
B4+W5	**1.9**	7.0E-01	0.1, 2.0	**1.8**	8.0E-01	0.1, 1.9	**2.1**	7.0E-01	0.1, 2.2	best-fit
W2+S1[b]	**2.7**	2.8E+00	0.5, 3.5	**2.4**	3.3E+00	0.6, 3.3	**2.9**	3.0E+00	0.4, 3.7	best fit

S2+P3+N3	**1.7**	9.0E-03	0.9, 2.6	**1.6**	2.0E-01	0.9, 2.4	**1.9**	2.0E-01	0.7, 2.7	best fit
S3+P4	**1.7**	1.0E-01	.5, 2.3	**1.5**	1.0E-02	0.6, 2.1	**2.0**	4.0E-01	0.3, 2.4	best fit
P2+N2	**1.8**	5.0E-01	0.1, 1.9	**1.2**	1.3E+00	0.1, 1.3	**2.2**	2.0E-01	0.2, 2.5	best fit
P3+N3	**3.8**	5.0E-04	0.5, 5.0	**3.3**	5.0E-04	0.5, 4.5	**4.2**	3.0E-04	0.5, 5.7	fixed-shape
S2+P3	**1.5**	6.0E-02	0.9, 2.3	**1.3**	1.0E-01	0.9, 2.0	**1.7**	2.0E-01	0.9, 2.6	best fit

[1] Modeled displacement profiles, using least-squares best fit of ellipses modeled using the function $([\sin(x/L)]^n)h$ (after Biasi and Weldon, 2009), where x/L is the normalized distance along the rupture (in 0.1-km increments), h controls the maximum height of the displacement curve, and n controls its shape (mostly uniform [0.1] to peaked [0.9]); see text for discussion. Error is the sum of the squared deviations of the modeled and observed displacements.

[2] Mean, minimum (min), and maximum (max) displacements per rupture are modeled mean displacements for analytical curves fit to the mean, min, and max site displacements, respectively. For ruptures having only one or two closely spaced displacement observations (Table B-8), the mean is the mean displacement from three ellipses with fixed shapes, using n = 0.2, 0.5, and 0.8. [a] The modeled mean, min, or max displacement reported for these ruptures is the average of modeled mean values for other ruptures on the source. However, for B4, the max displacement is the max of B1–B3 to yield a value greater than the B4 mean (2.0 m). [b] For W4 and W2+S1, the least-squares best-fit ellipse is used for the mean, whereas fixed-shape ellipses (n = 0.2 and 0.8) are used for the range, which yields more reasonable results. [c] For S1 and S3, the best-fit ellipses are used; however, fixed-shape ellipses yield similar results. [d] Because of significant uncertainties in the P2 displacement measurement (0.5–2.3 m; Table B-8), only a mean value is used; the small 0.5 m minimum displacement is not considered suitable for defining the PS minimum displacement. [e] For N1, observed and modeled mean and min displacement values exclude displacement from Santaquin site; the max displacement for N1 includes the Santaquin site displacement.

Table B-10. Summary of displacement per rupture source on the central WFZ.

Rupture Source[1]	**Obs. D**[2] (m)	**Modeled D (displacement curves)**[3] (m)			**EQs obs.**[4]	**Disp. obs.**[4]
	μ	μ	min	max		
BCS	2.0	1.7	1.2	2.1	4	6
WS	2.1	2.4	1.1	4.1	5	16
SLCS	1.7	1.7	1.2	2.2	4	8
PS	2.5	2.6	1.3	3.6	4	6
NS	1.8	2.0	1.5	2.7	3	5-6
BCS+WS	2.2	2.0	1.7	2.4	3	13
WS+SLCS	1.9	2.7	2.4	2.9	1	6
SLCS+PS+NS	2.1	1.7	1.6	1.9	1	3
SLCS+PS	2.0	1.6	1.3	2.0	2	6
PS+NS	2.1	2.8	1.2	4.2	2	4

[1] Vertical displacement (D) for single-segment rupture sources. See "Evaluation of Possible Multi-Segment Ruptures on the Central WFZ" section for discussion of multi-segment ruptures.

[2] Mean (μ) of observed displacement per earthquake on the source (Figure B-8; Table B-8). For example, mean observed displacement for BCS is mean of displacement estimates for B1, B2, B3, and B4 (Table B-8).

[3] Mean (μ) and min-max range of modeled displacement per earthquake on the source, using analytical displacement curves (Figure B-8; Table B-9).

[4] EQs. obs. is total number of earthquakes on the source. Disp. obs. is the total number of site observations of displacement for the source.

Table B-11. Open and closed mean vertical slip rates for the central segments of the WFZ.

Closed-interval vertical slip rate (average displacement and recurrence)[1]											
Source	**Average displacement** (m)			**Average recurrence interval** (yr)				**Vertical slip rate** (mm/yr)			
	Mean	Min	Max	Mean	2σ	Min	Max	Mean	Min	Max	
BCS	1.7	1.2	2.1	1062	235	827	1297	1.6	0.9	2.5	
WS	2.4	1.1	4.1	1332	124	1208	1456	1.8	0.8	3.4	
SLCS	1.7	1.2	2.2	1303	90	1213	1393	1.3	0.9	1.8	
PS	2.6	1.3	3.6	1327	249	1078	1576	2.0	0.8	3.3	
NS(N3)[a]	2.0	1.5	2.7	901	199	702	1100	2.3	1.4	3.8	
NS(N4)[a]	2.0	1.5	2.7	1499	586	913	2085	1.4	0.7	3.0	
Closed-interval vertical slip rate (total displacement and elapsed time)[2]											
Source	**Elapsed time** (yr)			**Total displacement** (m)				**Vertical slip rate** (mm/yr)			
	Mean	Min	Max	Mean	Min	Max	Events	Mean	Min	Max	
BCS (B4-B1)	3183	2280	4086	4.9	4.5	5.2	B3-B1	1.5	1.1	2.3	
WS (W5-W1)	5330	4759	5901	10.2	9.1	11.2	W4-W1	1.9	1.5	2.4	
SLCS (S4-S1)	3907	3523	4291	5.3	4.7	6.1	S3-S1	1.4	1.1	1.7	
PS (P5-P1)	5312	4262	6362	10.4	9.6	11.5	P4-P1	2.0	1.5	2.7	
NS (N3-N1)[a]	1798	1324	2272	3.7	3.2	4.4	N2-N1	2.1	1.4	3.3	
NS (N4-N1)[a,b]	4493	2639	6347	5.7	4.9	6.8	N3-N1	1.3	0.8	2.6	

Open-interval vertical slip rate[3]										
Source	**Limiting age constraint** (ka)			**Total displacement** (m)				**Vertical slip rate** (mm/yr)		
	Event	Time	2σ	Mean	Min	Max	Events	Mean	Min	Max
BCS	B4 (BEC4) max	5.9	0.4	6.9	6.0	7.3	B4-B1	1.2	0.9	1.3
WS	W5 (RC5) max	7.1	1.4	11.9	10.6	13.1	W5-W1	1.7	1.2	2.3
SLCS	S4 (SFDC4) max	5.2	0.4	6.6	5.9	7.6	S4-S1	1.3	1.0	1.6
PS	P5 (MN5) max	6.1	0.2	13.0	12.0	14.4	P5-P1	2.1	1.9	2.4
NS(N3)	N3 (WC3) max	3.2	0.1	5.7	4.9	6.8	N3-N1	1.7	1.5	2.2
NS(N4)[a]	N4 (WC4) max	6.2	0.1	8.1	6.9	9.5	N4-N1	1.3	1.1	1.5
Long-term vertical slip rates[4]										
Source	**Surface Age** (ka)			**Displacement/offset** (m)				**Vertical slip rate** (mm/yr)		
	Surface	Midpt.	Range	Midpt.	Min	Max	Source	Midpt.	Min	Max
BCS	P	15.8	1.8	15.5	10.0	21.0	a	1.0 [j]	0.6	1.5
BCS	B	17.6	0.3	21.5	16.0	27.0	a, b	1.2 [k]	0.9	1.6
WS	B/P	15.8	1.8	17.6	7.0	28.3	c	1.1 [l]	0.4	2.0
WS	P	15.8	1.8	14.2	4.6	23.7	b, c	0.9 [m]	0.3	1.7
SLCS	~B	15.9	0.7	14.5	11.5	24.5	e, f	0.9 [n]	0.7	1.6
PS	P	15.8	1.8	12.5	11.5	13.5	b, g, h	0.8 [o]	0.7	1.0
PS	B	17.6	0.3	21.5	15.0	28.0	b, h	1.2 [p]	0.8	1.6
NS	B	17.6	0.3	9.0	8.1	9.9	i	0.5 [q]	0.5	0.6
				Mean long-term SR for central WFZ:				**1.0**	**0.6**	**1.4**

[1] Closed interval slip rate per segment based on the modeled mean displacement (Table B-10) divided by the closed mean recurrence interval (Table B-7). [a] NS closed interval slip rates based on NS mean recurrence intervals determined using N3 or N4.

[2] Closed interval slip rate based on the total displacement (sum individual rupture displacements on the segment; for example, for B1 to B3; table B-9) following the elapsed time between earthquakes (e.g., B4 and B1), using the mean and two-sigma ranges for events (in parentheses) included in table B-6. [a] NS closed interval slip rates are based on the elapsed time between N4 and N1 and N3 and N1. [b] For the NS slip rate since N4, a displacement range of 2.0 (1.7-2.4) m is used for N3 based on N1, N2, and N4 (Table B-9).

[3] Open-interval slip rate per segment is based on the total displacement (sum of individual rupture displacements; Table B-9) divided by the elapsed time since the maximum limiting age on the oldest earthquake (e.g., B4 max for site earthquake BEC4) to the present (2011). [a] A displacement range of 2.0 (1.7-2.4) m is used for N3 based on N1, N2, and N4 (Table B-9).

[4] Long term slip rates based on displacements postdating the Bonneville (B) and Provo (P) shorelines. Sources: [a] Personius (1990), [b] Lund (2005), [c] Nelson and Personius (1993), [d] Nelson *et al.* (2006), [e] Personius and Scott (1992), [f] Lund (2007), [g] Machette *et al.* (1992), [h] Machette (1992), [i] DuRoss *et al.* (2008). Slip rate per source notes: [j] 10 m—P gravel south of Box Elder Cyn. 21 m—P delta at Box Elder Cyn, P gravel south of Pearsons Canyon. Personius *et al.* (2012) calculated a maximum rate of 1.3 ± 0.2 mm/yr using 21.2 ± 2.1 m (at Box Elder Canyon) and a P occupation time of 16.0 ± 1.0 ka (after Benson *et al.*, 2011), which is consistent with our min (0.6 mm/yr) and max (1.5 mm/yr) results for the BCS. [k] 16 m—undifferentiated gravel and B gravel north of Cook Cyn. 27 m—B delta north of Willard Canyon. [l] 17.6 m—mean of least-squares best-fit ellipse (shape: sin(L)^0.6, height: 24 m) using 22 displacements digitized from Nelson *et al.* (2006; their Figure 6). [m] 4.6 m—P shoreline north of Davis Cr. 19 m—P gravel S of Coldwater Canyon. 23.7 m—estimate from East Ogden trench site (Lund, 2005). [n] 14.5 m—mean displacement from Bells Canyon moraine (Swan et al., 1981). Age from Lips (Lund, 2007); Undifferentiated B displacement of 11.7–15.8 m from Warm Springs fault fits within min-max range. [o] 11.5-13.5 m—post P displacement at Hobble Creek. [p] 15 m—post B displacement at American Fork Canyon. 28 m—B Sand displaced north of Spanish Fork. We excluded a displacement of 40-45 m at Hobble Creek because of question of lower surface measured across large graben. [q] 9 m—offset of B shoreline at Santaquin Canyon (with 10% uncertainty added).

Table B-12. Weighted mean vertical slip rates for the central WFZ.

Slip Rate (SR):	**BCS** mm/yr [wt.]	**WS** mm/yr [wt.]	**SLCS** mm/yr [wt.]	**PS** mm/yr [wt.]	**NS** mm/yr [wt.]
Closed mean SR per segment[1]	1.6 (1.0–2.4) [0.2]	1.9 (1.1–2.9) [0.35]	1.3 (1.0–1.8) [0.35]	2.0 (1.2–3.0) [0.35]	1.7 (1.1–3.2) [0.2]
Open mean SR per segment[2]	1.2 (0.9–1.3) [0.2]	1.7 (1.2–2.3) [0]	1.3 (1.0–1.6) [0]	2.1 (1.9–2.4) [0]	1.5 (1.3–1.8) [0.2]
Composite closed mean SR[3]	1.7 (0.9–2.7) [0.3]	1.7 (0.9–2.7) [0.35]	1.7 (0.9–2.7) [0.35]	1.7 (0.9–2.7) [0.35]	1.7 (0.9–2.7) [0.3]
Composite long-term SR[4]	1.0 (0.6–1.4) [0.3]	1.0 (0.6–1.4) [0.3]	1.0 (0.6–1.4) [0.3]	1.0 (0.6–1.4) [0.3]	1.0 (0.6–1.4) [0.3]
Weighted mean SR[5]	**1.3 (0.8–2.0)**	**1.5 (0.9–2.4)**	**1.3 (0.8–2.0)**	**1.6 (0.9–2.4)**	**1.4 (0.9–2.2)**

[1] Closed-interval slip rate (SRs) are the average of mean, minimum, and maximum SRs based on (1) average displacement and recurrence and (2) elapsed time and total displacement (Table B-11). For the NS, the closed mean slip rate is the mean of SRs calculated using the N4–N1 and N3–N1 mean recurrence.

[2] Open-interval SRs are based on the total displacement since the maximum limiting age for the oldest earthquake on the segment (Tables B-7 and B-11). For the NS, the open mean slip rate is the mean of SRs calculated using the total displacement postdating N3 and N4.

[3] The composite closed mean SR is based on the mean of the per-source modeled mean displacements (Table B-10) and the composite closed recurrence interval for the central WFZ; see text for discussion.

[4] The composite long-term SR is the mean of the long-term SRs per segment based on the total net vertical displacement of latest Pleistocene-age geomorphic surfaces related to the Provo phase and highstand of Lake Bonneville (Table B-11).

[5] Weighted mean SRs per segment are based on weighting scheme for per-segment and composite SRs (weights shown in brackets).

Table B-13. Multi-segment ruptures included in central WFZ rupture models.

Multi-segment rupture[1]	**L**[2] (km)	**PDF over-lap**[3]	**Length of rupture studied**[4]			**Gap in paleoseismic data**[5]		**Displacement per rupture**[6] (m)			
								Observed		Modeled	
			(km)	(%)	n	(km)	(%)	range	n	mean	min-max
B3+W4	91	0.73	32	35%	5	45	49%	1.0–4.2	3	2.3	2.2–2.4
B4+W5	91	0.64	56	62%	4	33	36%	1.4–2.5	4	1.9	1.8–2.1
S2+P3	99	0.59	55	56%	5	37	37%	1.8–2.5	3	1.5	1.3–1.7
P3+N3	88	0.59	70	80%	5	35	40%	2.5	1	3.8	3.3–4.2
W2+S1	104	0.39	94	90%	6	50	48%	0.5–3.2	6	2.7	2.4–2.9
P2+N2	88	0.25	41	47%	4	43	49%	1.4–2.3	3	1.8	1.2–2.2
B2+W3	91	0.07	58	64%	7	24	26%	1.0–4.2	6	1.9	1.7–2.1
S3+P4	99	0.07	55	56%	4	38	38%	1.4–2.5	3	1.7	1.5–2.0
S2+P3+N3	128	NA	88	69%	7	36	28%	1.8–2.5	3	1.7	1.6–1.9

[1] Multi-segment ruptures included in the intermediate and multi-segment rupture models; see text for discussion.

[2] L – end to end rupture length.

[3] Overlap in segment PDFs (after Biasi and Weldon, 2009; see also DuRoss *et al.* (2011) (e.g., between PDFs for B4 and W5), which we consider good if greater than 0.5; see text for discussion.

[4] Straight-line distance between northernmost and southernmost paleoseismic sites where the earthquake has been identified (km) divided by L (%). We consider ruptures having paleoseismic data for greater than 50% of L to be well constrained. n is number of paleoseismic sites where data defines the earthquake-timing PDFs (site PDFs) that contribute to the rupture.

[5] Largest straight-line distance between paleoseismic sites or between a site and the end of the rupture (km) divided by L (%). We consider ruptures have paleoseismic data gaps of less than about 50% of L to be moderately well constrained.

[6] Observed displacement is range in site displacements along the rupture (Figure B-10); modeled displacement is mean and min-max range based on analytical displacement curves fit to the displacement observations (see text for discussion; Figure B-10; Table B-9).

Table B-14. Rupture models and weights for the central WFZ.

Rupture Model[1]	Rupture Sources[2]	WGUEP Weight[3]	Earthquakes[4]	Notes
SSR	B, W, S, P, N	0.7	22 SSR	Only SSRs occur
Int. C	B, W, S, P, N, B+W	0.075	18 SSR, 2 MSR	SSRs, including B+W MSR
-	B, W, S, P, N, W+S	-	-	W+S accounted for in MSR model
-	B, W, S, P, N, S+P	-	-	S+P ruptures separately
-	B, W, S, P, N, P+N	-	-	P+N ruptures separately
Int. A	B, W, S, P, N, B+W, S+P	0.05	16 SSR, 3 MSR	SSRs, including most-probable MSRs
Int. B	B, W, S, P, N, B+W, P+N	0.05	16 SSR, 3 MSR	SSRs, including most-probable MSRs
-	B, W, S, P, N, B+W, W+S…†	-	-	Accounted for in MSR model
MSR	B, W, S, P, N, B+W, W+S, S+P, P+N, S+P+N	0.025	7 SSR, 7 MSR	All possible MSRs occur
-	Unsegmented‡	0.1	-	-

[1] Rupture models include (1) all single-segment ruptures (SSRs) (SSR model; Figure B-11), (2) combinations of SSRs and multi-segment ruptures (MSRs) we consider most probable (Intermediate [Int.] A, B, and C; Figure B-12), and (3) all possible MSRs (MSR model; Figure B-13). See text for discussion of model development.

[2] Rupture sources: B – BCS, W – WS, S – SLCS, P – PS, N – NS; combinations of these indicate multi-segment-rupture sources (e.g., B+W). † Model representing SSRs plus one of many possible combinations of MSRs (e.g., B+W, W+S; or B+W, S+P). ‡The unsegmented model accounts for possible multi-segment and/or partial-segment ruptures not included in these models.

[3] Consensus weight of the WGUEP. No assigned weight indicates that rupture model not included.

[4] Number of earthquakes included in each rupture model; see Table B-15 for timing information for individual earthquakes.

Table B-15. Timing of multi-segment earthquakes on the central WFZ.

Rupture[1]	**Rupture model**[2]	**Earthquake Timing**[3] (ka)					
		Mean	Two sigma	5th	50th	95th	Mode
B2+W3	MSR	3.3	0.5	2.9	3.4	3.6	3.4
B3+W4	Int. A, B, C	4.5	0.4	4.1	4.5	4.9	4.5
B4+W5	Int. A, B, C	5.8	0.6	5.2	5.8	6.3	5.6
W2+S1	MSR	1.2	0.5	0.7	1.3	1.6	1.3
S3+P4	MSR	4.4	0.6	4.0	4.4	4.9	4.7
S2+P3	Int. A	2.2	0.3	1.9	2.2	2.5	2.2
S2+P3+N3	MSR	2.1	0.4	1.8	2.2	2.5	2.2
P2+N2	MSR	1.4	0.4	1.2	1.3	1.7	1.2
P3+N3	Int. B	2.1	0.5	1.7	2.1	2.5	2.1
B2+W3	MSR	3.3	0.5	2.9	3.4	3.6	3.4

[1] Rupture abbreviations: B – Brigham City segment (BCS), W – Weber segment (WS), S – Salt Lake City segment, P – Provo segment, N – Nephi segment. B2+W3 indicates a multi-segment rupture of BCS earthquake B2 and WS earthquake W3.

[2] Rupture model: MSR – multi-segment rupture model, Int. – Intermediate (A, B, C) models.

[3] Summary statistics based on integration of per-segment earthquake-timing PDFs.

Table B-16. Segment boundary uncertainties and rupture lengths for the central WFZ.

Rupture	**Median SRL**[1] (km)	**SRL uncert.**[2] (km) North end	South end	**Min SRL**[3] (km)	**Max SRL**[3] (km)
Brigham City segment (BCS)	35	± 3	+ 3, -8	24	41
Weber segment (WS)	56	+8, -3	± 7	46	71
Salt Lake City (SLCS)	40	± 7	± 6	27	53
Provo segment (PS)	59	± 6	+4, -13	40	69
Nephi segment (NS)	43	+5, -17	± 6	20	54
BCS+WS	91	± 3	± 7	81	101
WS+SLCS	104	+8, -3	± 6	95	118
SLCS+PS	99	± 7	+4, -13	79	110
PS+NS	88	± 6	± 6	76	100
SLCS+PS+NS	128	± 7	± 6	115	141

[1] Median surface rupture length (SRL) per rupture source based on the linear distance between segment ends.

[2] SRL uncertainties at the northern and southern rupture ends based on segment-boundary uncertainties (Figures B-14 and B-15). Two values indicate asymmetric uncertainties about median value.

[3] Minimum and maximum possible SRL per rupture source based on segment-boundary uncertainties.

Table B-17. Summary of segment-boundary uncertainties for the central WFZ.

Rupture	SRL[1] (km)	Segment Boundary Uncertainty[2]			
		North end		South end	
		km	Description	km	Description
Brigham City segment (BCS)	35	± 3	Based on 3 km of Holocene spillover rupture from the BCS onto the southernmost Collinston segment (CS) mapped by Personius (1990) (see also Personius *et al.*, 2012). A larger uncertainty was not considered because the CS does not have evidence of Holocene surface faulting.	+ 3, -8	3-km uncertainty based on the geometry of the fault step-over between the BCS and WS, and the distance from the south end of the BCS to the Rice Creek trench site on the WS. Rupture beyond 3 km likely consisted of multi-segment ruptures (e.g., B4+W5) accounted for the paleoseismic rupture models. The 8-km uncertainty is based on the spillover rupture of WS earthquake W2 onto the southern BCS (DuRoss *et al.*, 2012; Personius *et al.*, 2012).
Weber segment (WS)	56	+8, -3	See description for south end of BCS.	± 7	Uncertainty based on the geometry of the Salt Lake salient (WS–SLCS segment boundary), the length of the Warm Springs fault (~7–10 km), and the distance from the south end of the WS to the Penrose Drive trench site on the SLCS.
Salt Lake City (SLCS)	40	± 7	See description for south end of WS.	± 6	Uncertainty based on the geometry of the SLCS–PS segment boundary and the distance from the boundary to the Little Cottonwood Canyon and South Fork Dry Creek trench sites on the SLCS.
Provo segment (PS)	59	± 6	See description for south end of SLCS.	+4, -13	4-km uncertainty based on the distance from the southern end of the PS to the southern end of the northern strand of the NS. Larger uncertainty not included because we do not consider it likely that spillover rupture would extend from the PS to the southern strand of the NS (this scenario included in paleoseismic rupture models). 13-km uncertainty based on the distance from the southern end of the PS to the north end of the northern strand of the NS. This distance also corresponds with the distance from the south end of the PS to the Mapleton trench site.

Nephi segment (NS)	43	+5, -17	5-km uncertainty based on the distance from the north end of the northern strand of the NS to the Mapleton trench site on the PS. 17-km uncertainty based on the length of the northern strand of the NS.	± 6	Uncertainty based on the distance from the south end of the NS to the north end of the Levan segment (the gap in the rupture trace).
BCS+WS	91	± 3	See description for north end of the BCS.	± 7	See description for south end of the WS.
WS+SLCS	104	+8, -3	See description for north end of the WS.	± 6	See description for south end of the SLCS.
SLCS+PS	99	± 7	See description for north end of the SLCS.	+4, -13	See description for south end of the PS.
PS+NS	88	± 6	See description for north end of the PS.	± 6	See description for south end of the NS.
SLCS+PS+NS	128	± 7	See description for north end of the SLCS.	± 6	See description for south end of the NS.

[1] Median surface rupture length (SRL) per rupture source based on the linear distance between segment ends.

[2] SRL uncertainties at the northern and southern rupture ends based on segment-boundary uncertainties (Figures B-14 and B-15). Two values indicate asymmetric uncertainties about median value.

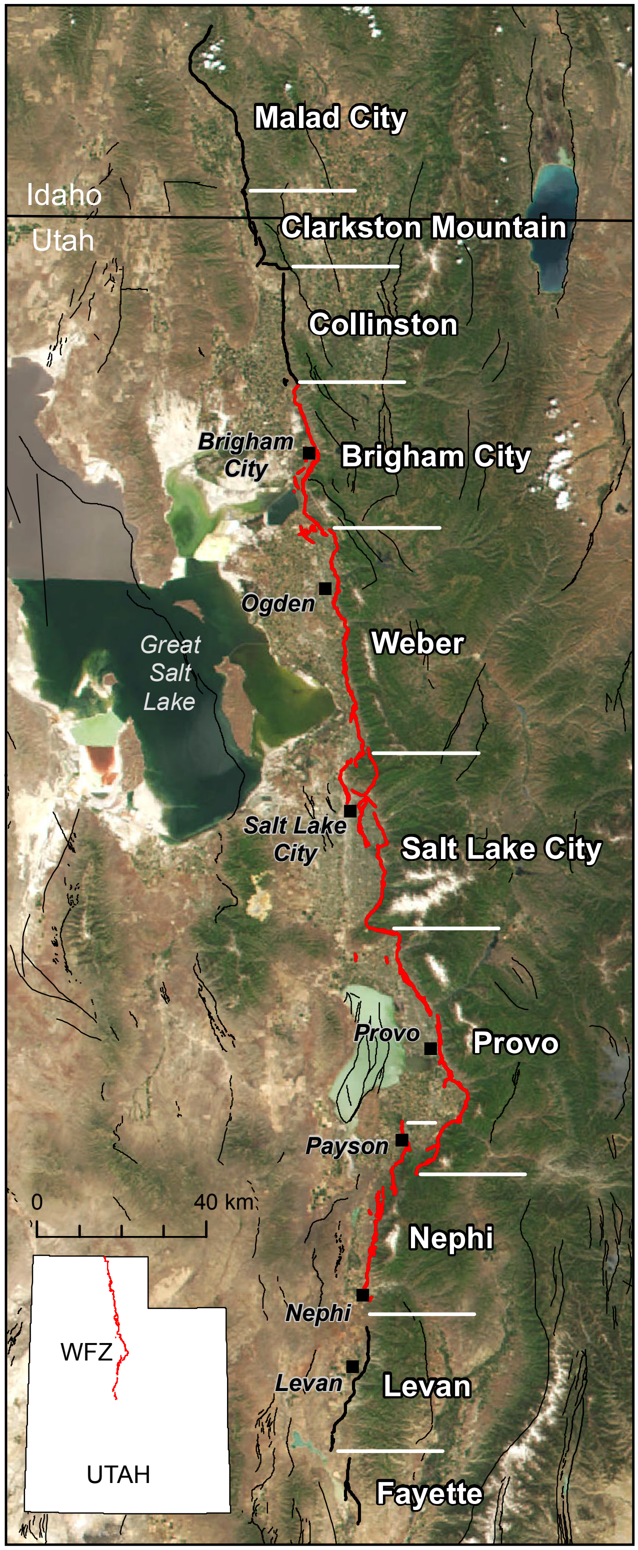

Figure B-1. Segments of the Wasatch fault zone (WFZ) in southern Idaho and northern Utah. The central WFZ, which has evidence of repeated Holocene surface-faulting earthquakes, is shown in red; end segments of the WFZ are shown in black. Other Quaternary faults in northern Utah are shown in dark gray. Fault traces are from Black *et al*. (2003); base map is true-color satellite image from the National Aeronautics & Space Administration (NASA; http://visibleearth.nasa.gov/view.php?id=55874).

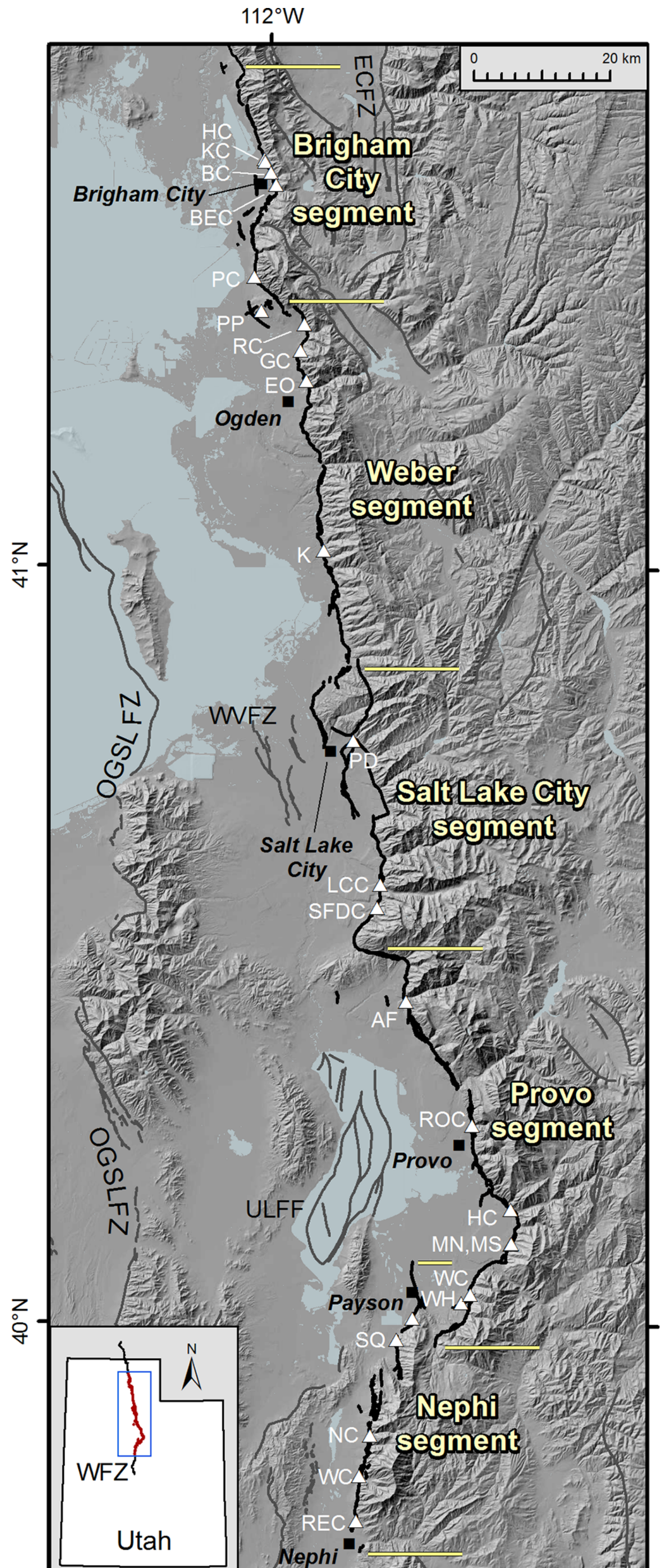

Figure B-2. Central segments of the WFZ (from Black *et al*., 2003) showing paleoseismic research sites (yellow triangles; see appendix A for site abbreviations). ECFZ – East Cache fault zone, ETMF – East Tintic Mountains fault, GSLFZ – Great Salt Lake fault zone, OFZ – Oquirrh fault zone, SOMFZ – Southern Oquirrh Mountains fault zone, THFZ – Topliff Hills fault zone, ULFF – Utah Lake faults and folds, WVFZ – West Valley fault zone. Shaded topography generated from 10-m digital elevation data (https://lta.cr.usgs.gov/NED).

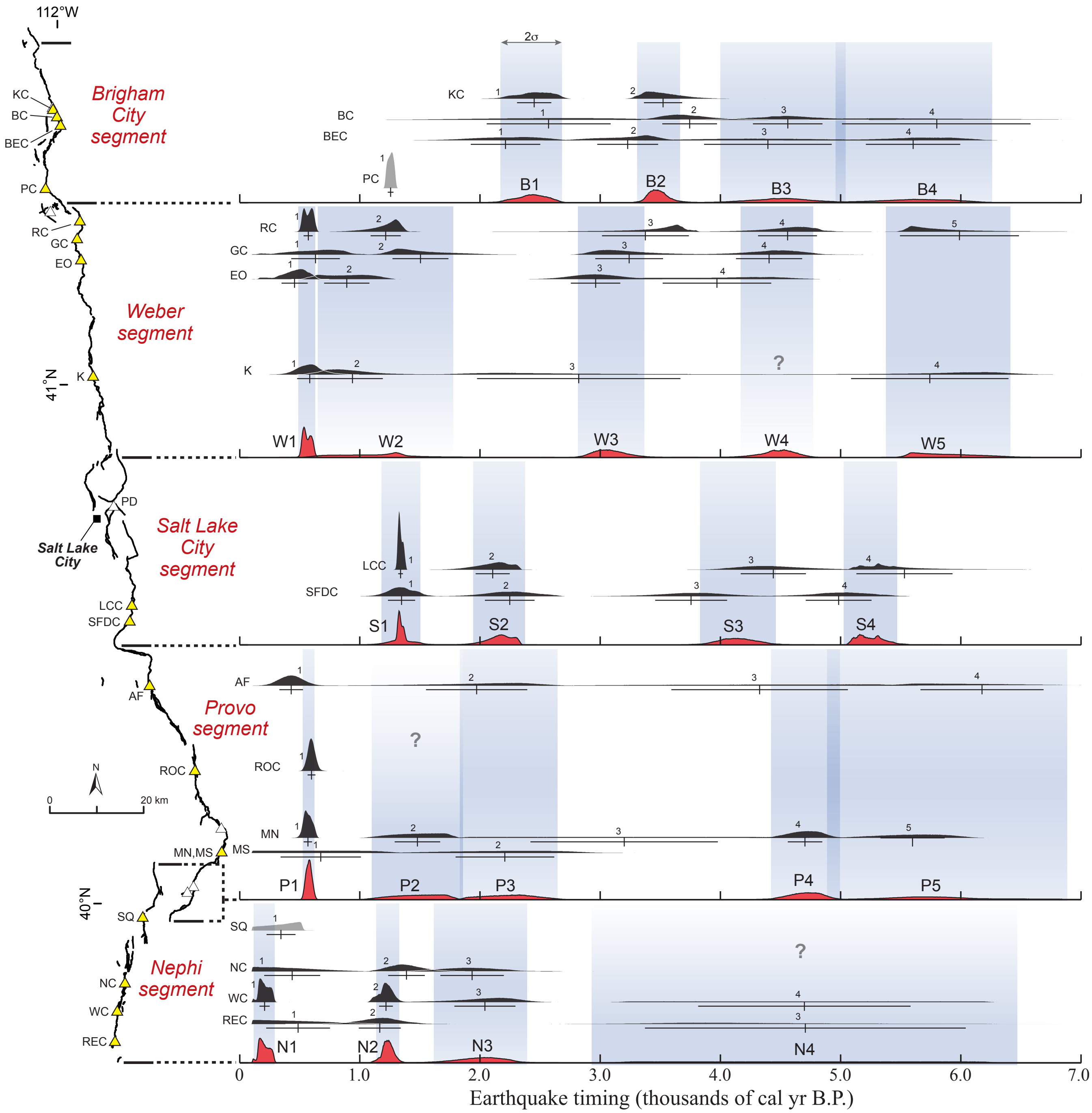

Figure B-3. Correlation of surface-faulting earthquakes identified at paleoseismic sites (yellow triangles) on the central WFZ. For each segment, black earthquake-timing distributions are site probability density functions (site PDFs) derived from OxCal (appendix A); abbreviations and event numbers correspond to Tables B-1 to B-5. Vertical blue bands show correlation of site PDFs along segment to form segment PDFs (red-filled time distributions; e.g., B1; Table B-6). Site earthquake PDFs not included in segment-PDF calculation (e.g., PC1 and SQ1) are shaded gray. See text for additional discussion.

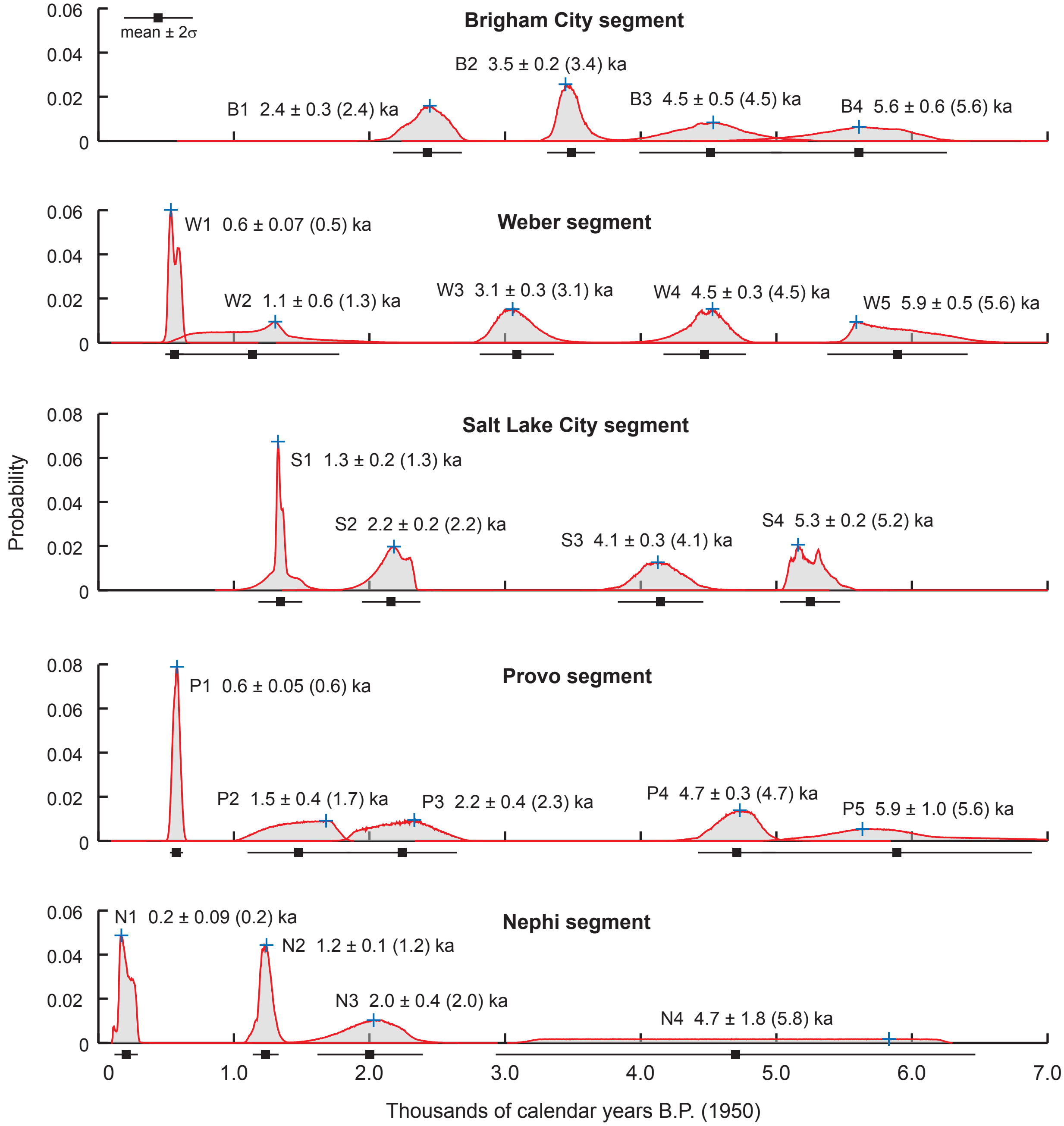

Figure B-4. Timing of surface-faulting earthquakes on the central segments of the WFZ. Red lines are earthquake-timing probability density functions (PDFs) derived from our integration of site paleoseismic data (Figure B-3; appendix C; see text for discussion). Earthquake times are reported as mean ± 2σ, and modal times (corresponding to the peak probabilities) are shown by blue crosses with modal value in parentheses.

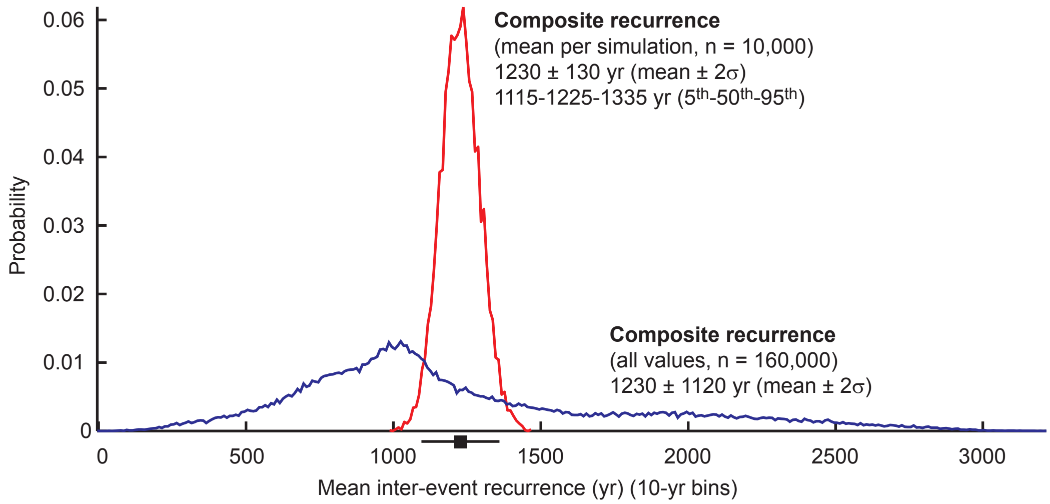

Figure B-5. Composite recurrence intervals for the central WFZ determined by (1) sampling and averaging 16 inter-event recurrence intervals (per segment; e.g., W5–W4, but not W5–B4) in numerous simulations (red shaded PDF—see text for discussion) and (2) taking all possible inter-event recurrence intervals in numerous simulations (blue line). The composite recurrence, or distribution of means, is narrower than the recurrence distribution for the complete (grouped) dataset, where each inter-event recurrence value is included and treated equally.

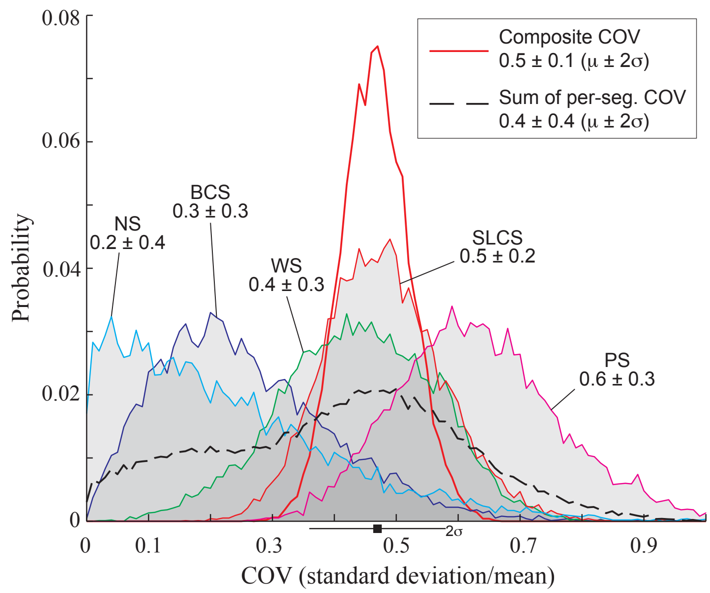

Figure B-6. Composite coefficient of variation (COV) of earthquake recurrence for the central WFZ (solid black line), calculated by compiling 16 inter-event-recurrence PDFs (per segment; e.g., W5–W4, but not W5–B4) and sampling them in a Monte Carlo model. Each simulation produced a group of 16 randomly sampled inter-event recurrence times from which we calculated the COV (standard deviation divided by the mean of the 16 recurrence intervals). The COV calculation thus uses the full inter-event recurrence distributions, but does not account for sample-size uncertainties. The composite COV distribution (and mean and 2σ values) is based on the COVs calculated in numerous simulations. The 5th–95th percentile range for the NS is shown in parentheses because of the asymmetric shape of the COV distribution. We also segregated the sampled recurrence PDFs by segment and computed segment-specific COVs (dashed and colored COV distributions; segment abbreviations correspond with Figure B-3), which we then summed to form a composite COV (dashed black line). Ultimately, the composite approach yields the most robust mean COV for the region; however, the COV estimates for the individual segments, although based on limited data, show more variability.

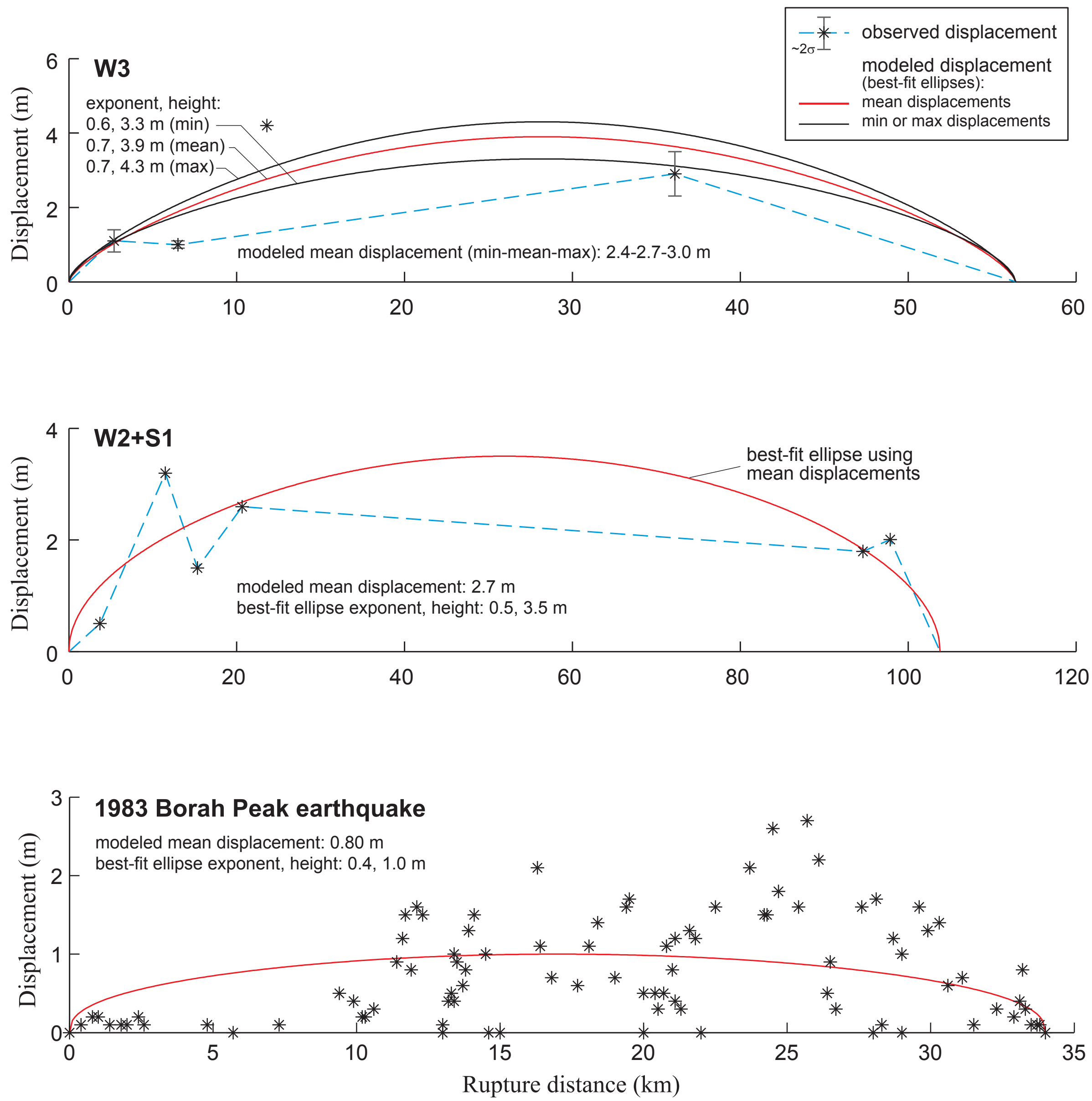

Figure B-7. Examples of analytical displacement curves fit to displacement observations for single and multiple segment ruptures on the central WFZ (upper two panels) and the 1983 Borah Peak earthquake (lower panel). In upper panel, the three curves are fit to the mean (red), and minimum and maximum (black) displacement observations using a least-squares, best fit method (see text for discussion). For the lower two panels, only displacement curves fit to the mean displacement values are shown. Per-site displacement observations are shown as black asterisks (Borah Peak observations are from Wesnousky [2008]); blue dashed lines are simple displacement profiles (between displacement observations); not shown for the Borah Peak displacements. Modeled mean displacements are determined by sampling the analytical displacement curves in 0.1 km increments.

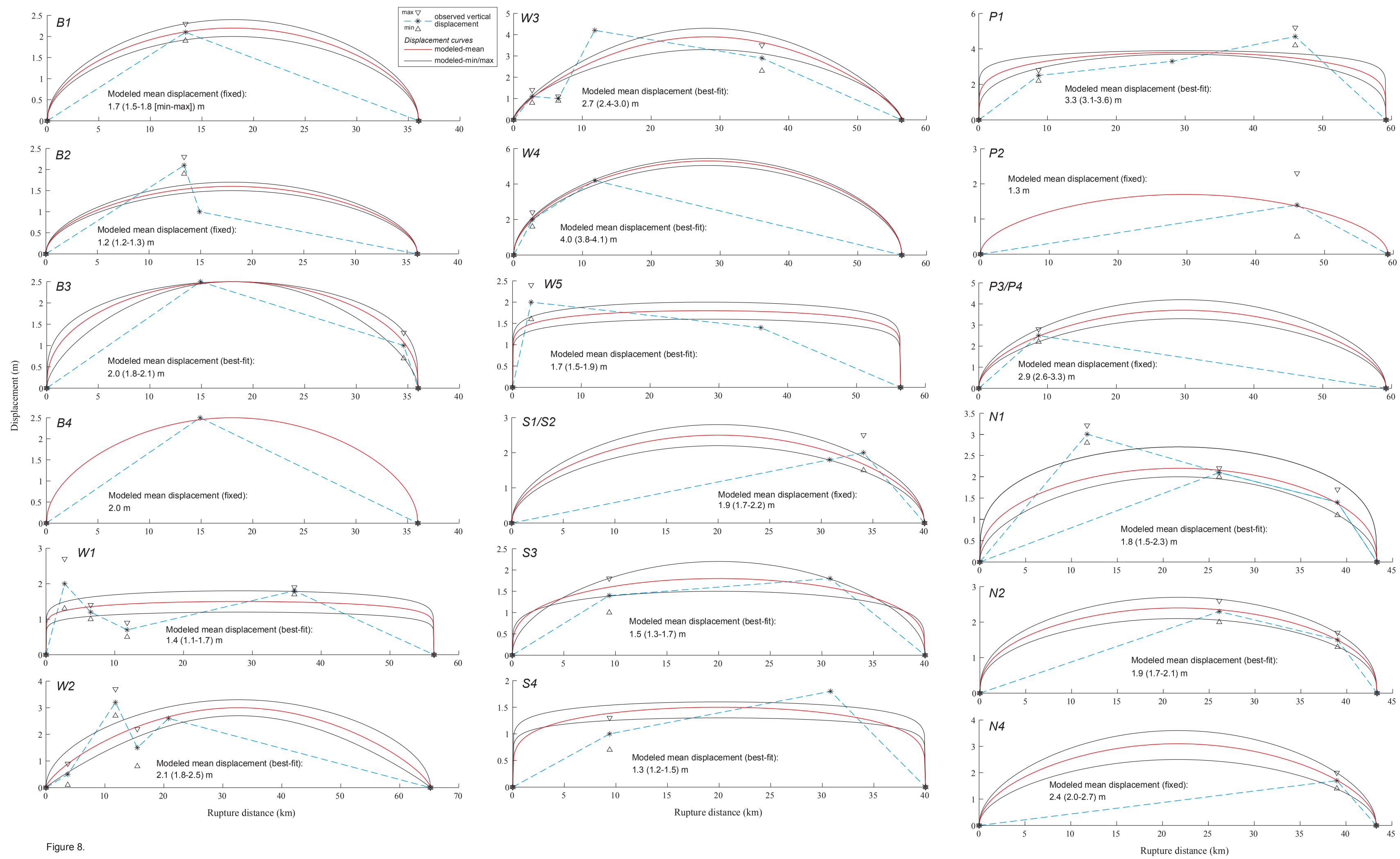

Figure B-8. Analytical displacement curves for single-segment ruptures on the central WFZ. Single displacement curves indicate those fit to the mean displacement observations (using a least-squares method with the curve shape and maximum height allowed to vary); multiple curves (e.g., for B1) are analytical displacement curves with fixed shapes (flat, half-ellipse, and peaked) are fit to the displacement observations (see text for discussion of both methods). Site displacements (black asterisks) correspond to table B-8; blue dashed lines are simple displacement profiles (between displacement observations). Modeled displacements, calculated by sampling the analytical displacement curves in 0.1 km increments, correspond to table B-9.

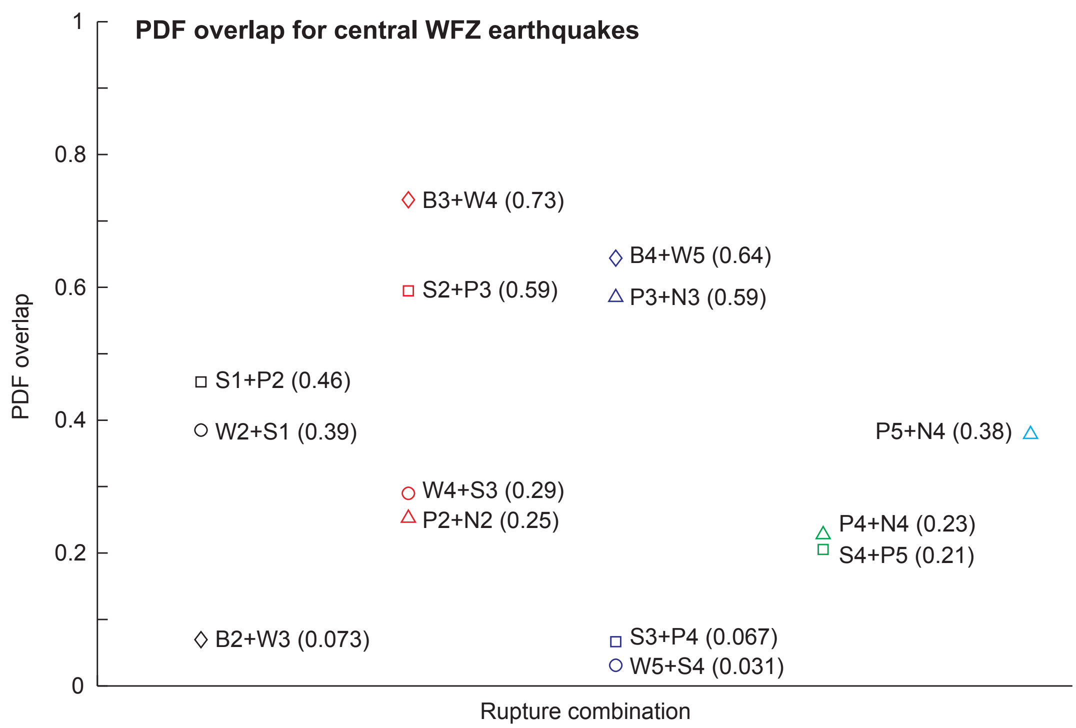

Figure B-9. PDF overlap for pairs of earthquakes on the central WFZ (adjacent segments only). PDF overlap ranges from 0 (no overlap) to 1 (two identical PDFs) and is found by summing the minimum probabilities for common time bins in two overlapping PDFs (Biasi and Weldon, 2009; see also DuRoss *et al*., 2011). The letter-number pairs refer to individual earthquakes on specific segments; B–Brigham City, W–Weber, S–Salt Lake City, P–Provo, and N–Nephi (tables B-1 to B-5).

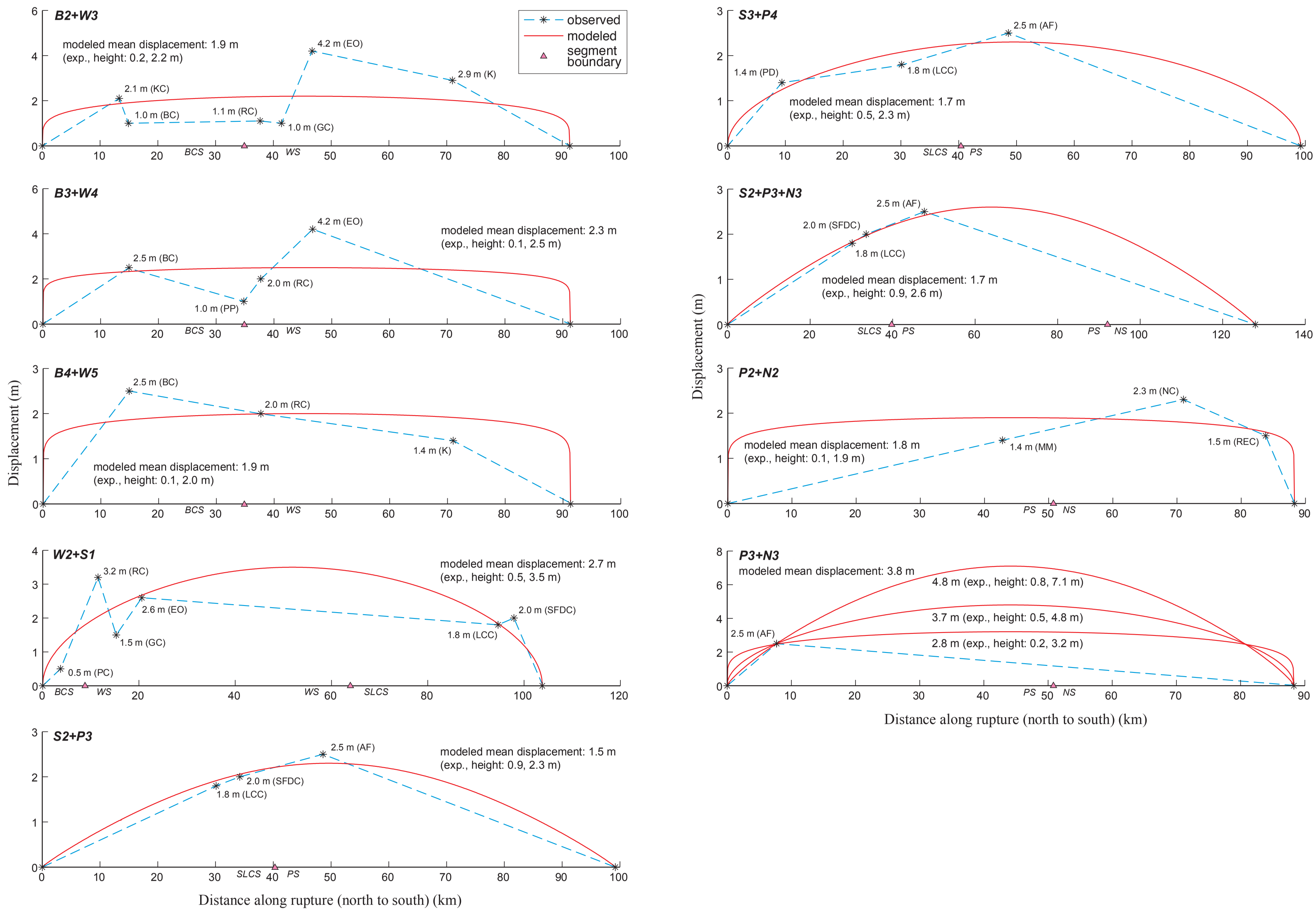

Figure B-10. Analytical displacement curves for multi-segment ruptures on the central WFZ. All curves are fit to the mean displacement observations (using a least-squares method with the curve shape and maximum height allowed to vary), with the exception of P3+N3, where three analytical displacement curves with fixed shapes (flat, half-ellipse, and peaked) are fit to the displacement observation (see text for discussion of both methods). Site displacements (black asterisks) correspond to table B-8; blue dashed lines are simple displacement profiles (between displacement observations). Modeled displacements, calculated by sampling the analytical displacement curves in 0.1 km increments, correspond to table B-9.

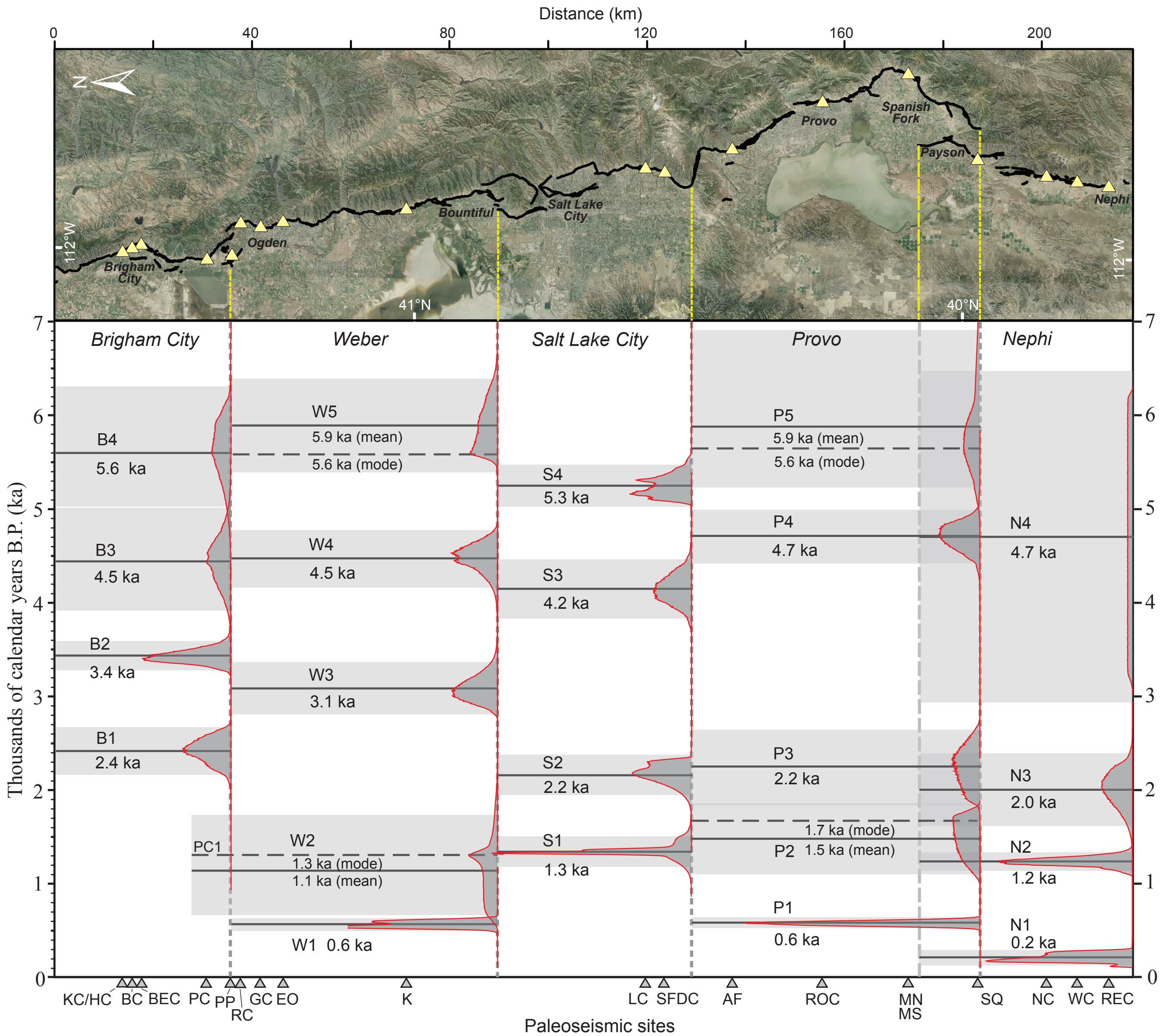

Figure B-11. Single-segment rupture model for the central WFZ. Upper panel shows map of the central segments; yellow triangles show locations of paleoseismic study sites. Lower panel shows times of earthquakes on each segment. Solid horizontal lines indicate mean earthquake times (dashed lines indicate modal times for select earthquakes); gray boxes show 2σ time ranges. Red lines with gray-shaded fill are segment PDFs from Figure B-3; see text for discussion and table B-6 for correlation of site-PDFs and site abbreviations. Base map is aerial imagery (https://gdg.sc.egov.usda.gov/) overlain on shaded topography generated from 10-m digital elevation data (https://lta.cr.usgs.gov/NED).

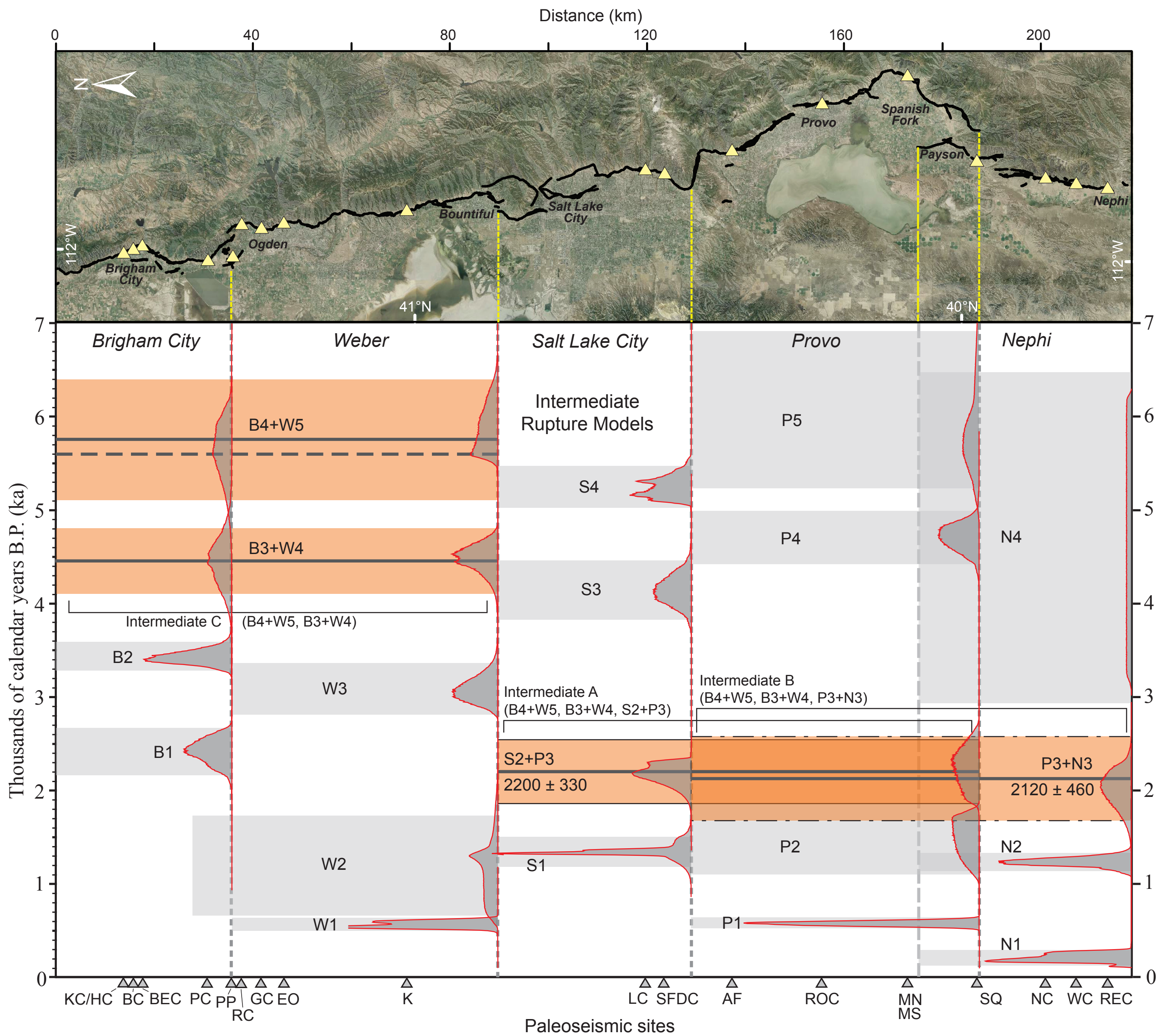

Figure B-12. Intermediate rupture models for the central WFZ. Upper panel is the same as in Figure B-8. Intermediate model A consists of single-segment ruptures (gray boxes showing 2σ ranges) and multi-segment ruptures B4+W5, B3+W4, and S2+P3 (orange boxes showing 2σ ranges). Intermediate model B includes P3+N3 in place of S2+P3. Intermediate model C has single-segment ruptures as well as multi-segment ruptures B4+W5 and B3+W4. Solid horizontal lines indicate mean earthquake times (dashed lines indicate modal times for select earthquakes). Red lines with gray-shaded fill are segment PDFs from Figure B-3; see text for discussion and tables B-6 and B-8 for correlation of site-PDFs and site abbreviations. Base map is aerial imagery (https://gdg.sc.egov.usda.gov/) overlain on shaded topography generated from 10-m digital elevation data (https://lta.cr.usgs.gov/NED).

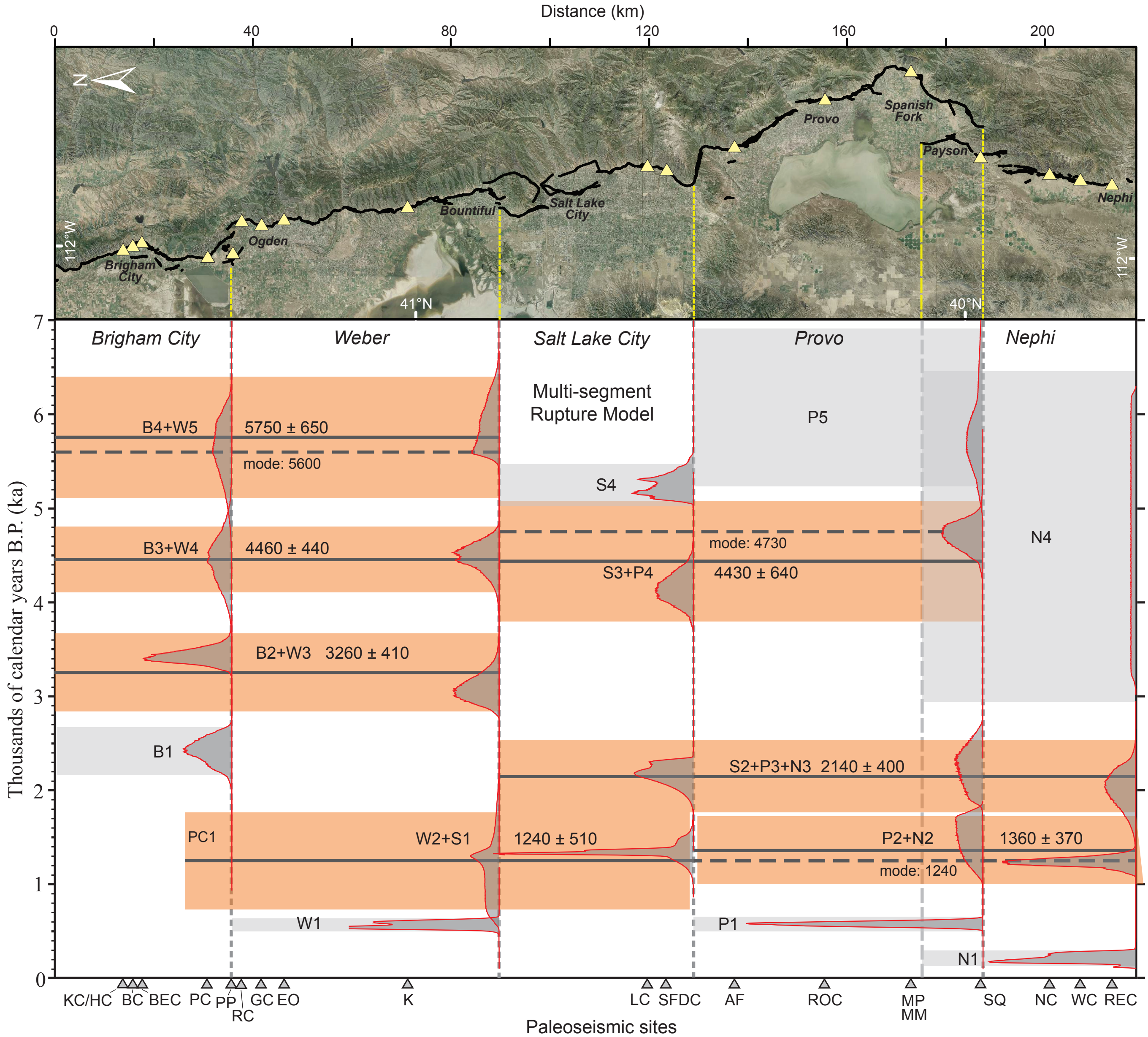

Figure B-13. Multi-segment rupture model for the central WFZ consisting of single-segment ruptures (gray boxes showing 2σ ranges) and multi-segment ruptures (orange boxes showing 2σ ranges). Solid horizontal lines indicate mean earthquake times (dashed lines indicate modal times for select earthquakes). Red lines with gray-shaded fill are segment PDFs from Figure B-3; see text for discussion and tables B-6 and B-8 for correlation of site-PDFs and site abbreviations. Base map is aerial imagery (https://gdg.sc.egov.usda.gov/) overlain on shaded topography generated from 10-m digital elevation data (https://lta.cr.usgs.gov/NED).

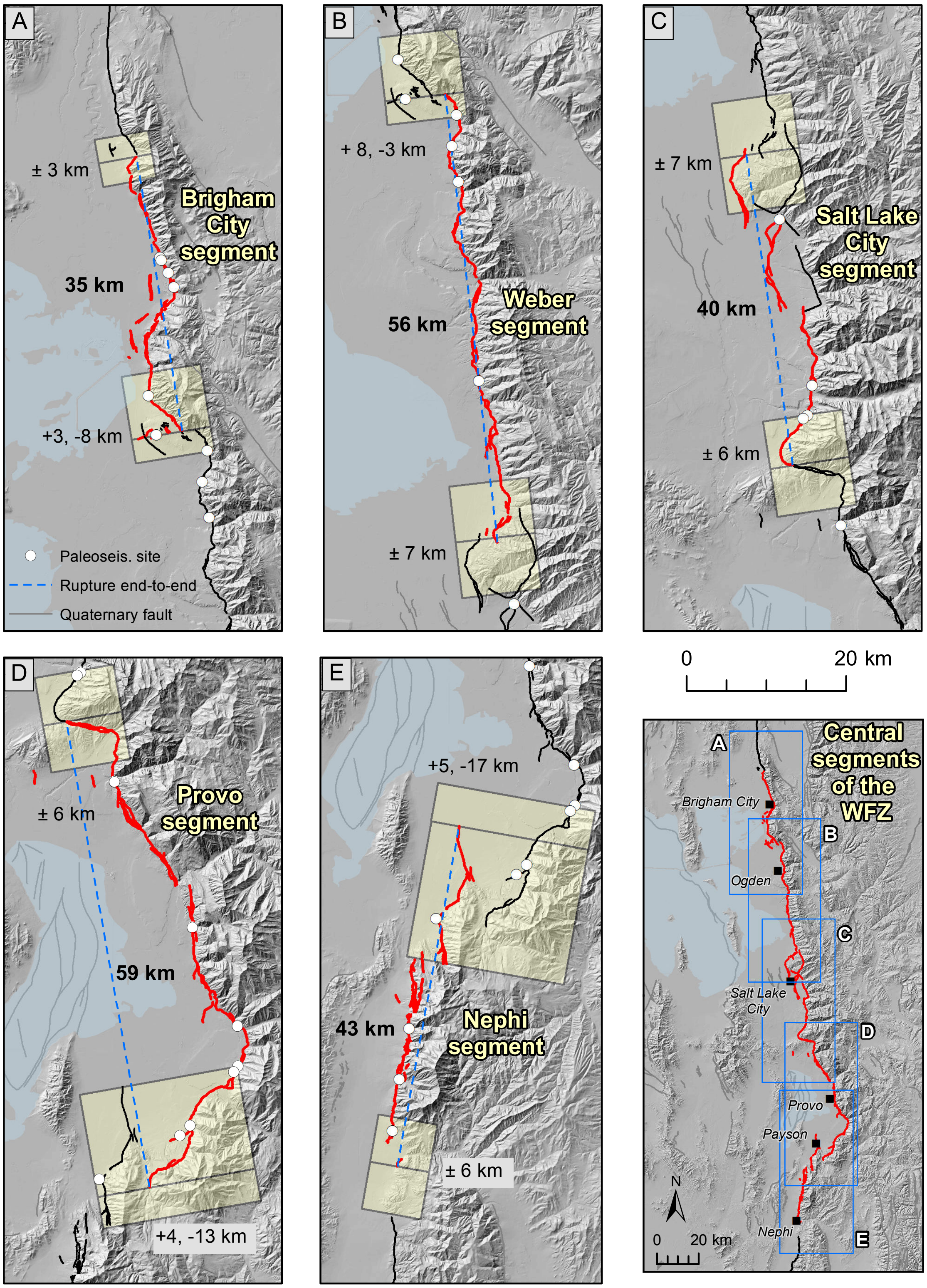

Figure B-14. Segment-boundary uncertainties for single-segment ruptures on the central WFZ. Yellow boxes correspond to segment-boundary uncertainties defined using the geometry and timing of faulting close to the segment boundaries, and paleoseismic data, if available. White dots show paleoseismic sites, and blue dashed lines are straight-line length measurements (between rupture ends), with median rupture lengths (e.g., 35 km for the BCS) shown. See text and table B-17 for discussion of individual segment-boundary uncertainties. Shaded topography generated from 10-m digital elevation data (https://lta.cr.usgs.gov/NED).

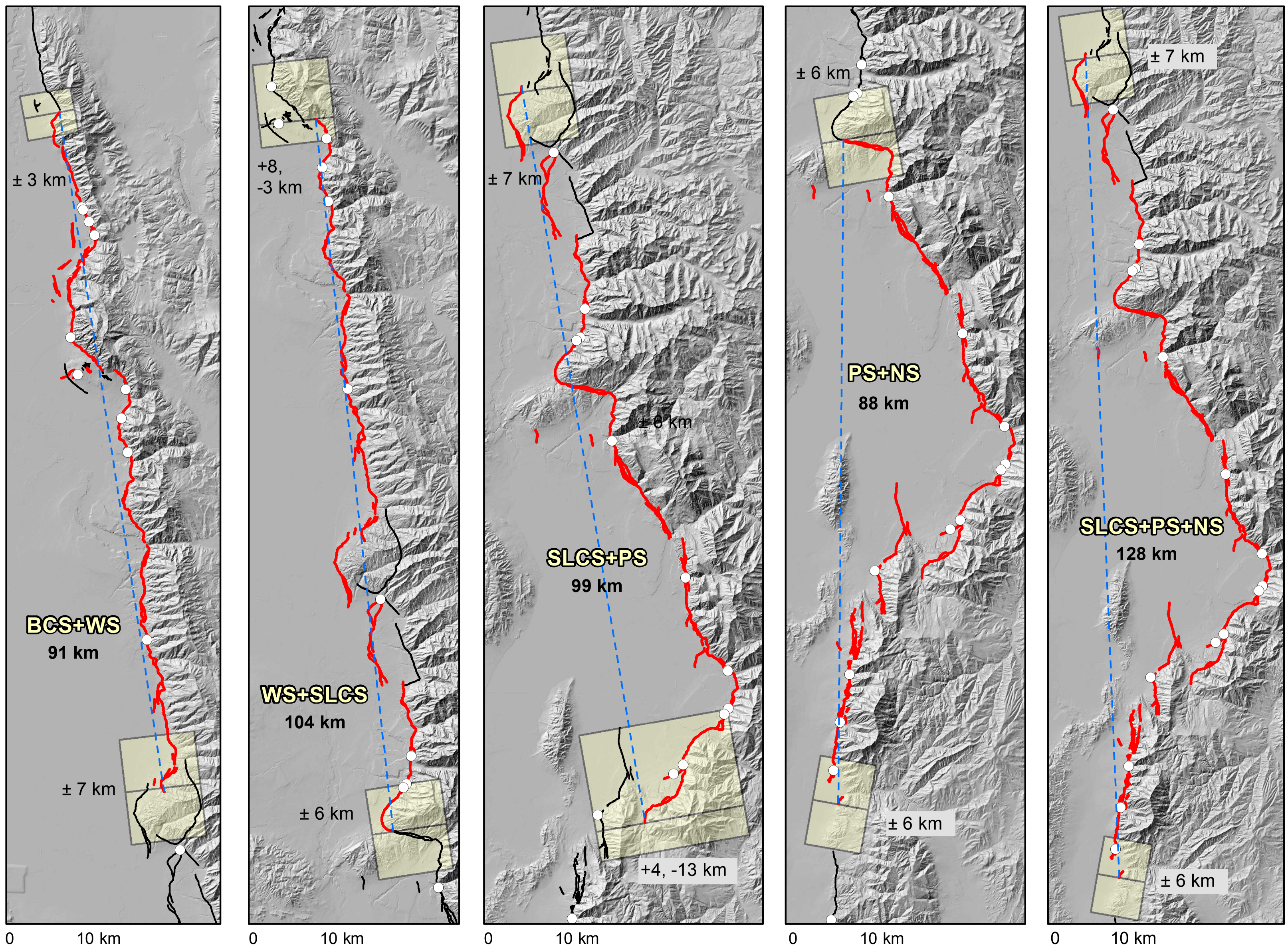

Figure B-15. Segment-boundary uncertainties for multi-segment ruptures on the central WFZ. Yellow boxes correspond to segment-boundary uncertainties defined using the geometry and timing of faulting and paleoseismic data, and are the same as those defined for single-segment ruptures (Figure B-14). White dots show paleoseismic sites, and blue dashed lines are straight-line length measurements (between rupture ends), with median rupture lengths (e.g., 91 km for the BCS+WS multi-segment rupture source) shown. See text and table B-17 for discussion of individual segment-boundary uncertainties. Shaded topography generated from 10-m digital elevation data (https://lta.cr.usgs.gov/NED).